



Università degli Studi di Cagliari

DIPARTIMENTO DI FISICA
Corso di Dottorato di Ricerca in Fisica

SETTORE SCIENTIFICO DISCIPLINARE DI AFFERENZA FIS/04

Improvement of muon identification algorithms and perspectives on the $D^0 \rightarrow \mu^+ \mu^-$ search

Presentata da:
Violetta Cogoni

Tutor:
Dott. Alessandro Cardini
Coordinatore di dottorato:
Prof. Alessandro De Falco

Contents

Contents	iii
1 Theory overview	1
1.1 The Standard Model of Particle Physics	1
1.2 The GIM mechanism	5
1.3 The CKM matrix	6
1.4 CP violation in the quark sector	8
1.5 Rare decays and the $D^0 \rightarrow \mu^+ \mu^-$ case	14
2 The LHCb experiment	19
2.1 The Large Hadron Collider	19
2.2 The LHCb experiment	20
2.3 Tracking System	22
2.4 RICH system	32
2.5 Calorimeters	36
2.6 Muon System	40
2.7 Trigger	51
2.8 Simulation in LHCb	55
2.9 Reconstruction and analysis	55
3 The LHCb Upgrade	57
3.1 Physics Motivation	58
3.2 The upgrade of the LHCb detector	60
3.3 The upgraded Muon System	65
4 Muon Identification at LHCb	71
4.1 The Muon Identification procedure	71
4.2 Performance of the Muon Identification	74

5	A novel muon identification algorithm	81
5.1	The new algorithm	81
5.2	Test on Monte Carlo for the upgrade	85
5.3	Validation on data	87
6	The $D^0 \rightarrow \mu^+ \mu^-$ decay case	97
6.1	Data and Monte Carlo samples	99
6.2	Selection	99
6.3	Normalisation	111
6.4	Fit model	118
6.5	Results	121
7	Conclusions	123
A	Multivariate selection	125
A.1	Boosted Decision Tree	125
A.2	Training, test and application	127
A.3	Likelihood	127
A.4	Neural Networks	128
	Bibliography	131

Introduction

The Standard Model of Particle Physics (SM) is the theory that best describes the fundamental particles and their interaction, with the exception of gravity. Despite representing the acme of human knowledge about the constituents of nature, the SM is an incomplete theory, since there are physics phenomena which are not described in the SM or which even deviate from its predictions. Among them, we can observe how the universe is mostly made of matter, and CP-symmetry violation is a fundamental ingredient to explain the observed matter-antimatter asymmetry. Nevertheless, this discrepancy is too large to be only generated by the mechanism described in the SM, thus suggesting the presence of additional sources of CP violation beyond those predicted in the theory. The effects of New Physics (NP) not included in the SM can be searched either directly, by increasing the available energy at colliders to produce new particles and reveal them, or by increasing the experimental precision on the detection of processes involving particles already described in the SM. The second case, *i.e.* the indirect search for NP, can profit from decays that are precisely calculable, very rare or completely forbidden in the Standard Model.

Flavour-changing neutral current (FCNC) and CP-violating processes are among the most powerful probes when searching for NP. In the SM, FCNC are forbidden at tree level and they are also strongly suppressed at loop level. Once CKM elements are precisely determined, the study of FCNC allows to search for NP contributions.

The CP violation has been measured with high accuracy in several $b \rightarrow s$ decay channels. The study of particles containing b quarks can thus help in the identification of the flavour structure of the physics beyond the Standard Model.

Among the four main experiments that use the LHC accelerator, the LHCb experiment is the one devoted to the study of b -hadron physics, and it has been optimised to allow precise measurements of CP violation and

the study of rare decays. The presence of muons in the final state of many of the decays studied for this purpose makes the efficient muon triggering and the correct muon identification crucial requirements for the success of the LHCb physics programme. In order to fully exploit its flavour physics potential, LHCb will start from 2020 a data taking period with an increased instantaneous luminosity to perform very high precision measurements. As a consequence it becomes mandatory to develop new algorithms that allow to maintain or even improve the current muon identification capabilities when operating at higher detector occupancies.

The main topic of this thesis connects with this fundamental subject presenting the development and the first applications of a novel algorithm for the muon identification at LHCb.

Chapter 1 introduces the Standard Model of Particle Physics with a description of the processes that are useful to understand the study of rare decays of D mesons, with particular care for the $D^0 \rightarrow \mu^+\mu^-$ case. Chapter 2 provides an overview of the LHCb experiment, with a description of its subdetector together with a brief explanation of the simulation, reconstruction, and analysis strategies at LHCb. Chapter 3 describes the physics motivations and the improvements foreseen for the upgrade of the LHCb detector. All the general aspects are covered, and particular emphasis is given to the upgrade of the Muon System. Chapter 4 presents the current status of the muon identification at LHCb together with its performance. Chapter 5 and 6 are the core of the current work. In Chapter 5 the new algorithm for the muon identification developed by the author is presented, together with its application on a Monte Carlo sample produced in upgrade conditions. This test allowed the author to study the performances of the method in a situation of high occupancy of the muon system. The first application on data of this algorithm has been in the search for the $K_S^0 \rightarrow \mu^+\mu^-$ decay, which is here reported for completeness, even if the author did not take part to the analysis. Following this work, the author also reports her preliminary studies on the application of the method on the $J/\psi \rightarrow \mu^+\mu^-$ case, where the performances of the new algorithm are compared to those which are currently used. Finally Chapter 6 concentrates on the use of the new method on the $D^0 \rightarrow \mu^+\mu^-$ analysis to obtain an expected upper limit for the branching fraction of this decay channel. It is worth noting that most of the tools for this study are shared with the official analysis for the search of the $D^0 \rightarrow \mu^+\mu^-$ decay, which is currently under way. The analysis presented here is a preliminary study focused on the understanding of the performances of the new algorithm on a benchmark channel such as the

$D^0 \rightarrow \mu^+ \mu^-$. Conclusions are drawn in Chapter 7.

Theory overview

1.1 The Standard Model of Particle Physics

Elementary particle physics describes what is the matter made of on the smallest scale of size. Surprisingly, the huge quantity of matter we are surrounded with only consists of a limited number of different types of objects at the subatomic level. Different replicas of the same object type have a feature that is missing in the macroscopic world: they are completely indistinguishable.

From the 1970s, a theory has been formulated that describes all of the known elementary particle interactions except gravity. This is actually a collection of theories, incorporating quantum electrodynamics (QED), the Glashow-Weinberg-Salam theory of electroweak processes, and quantum chromodynamics (QCD), and is called Standard Model (SM).

The Standard Model describes all the known matter as made out of three kind of elementary particles: leptons, quarks, and mediators [1, 2].

Leptons are 1/2 spin particles (called *fermions*) that carry integral electric charge and that interact via electroweak interactions. They are classified according to their electric charge (Q), electron number (L_e), muon number (L_μ), and tau number (L_τ) and are organised into three *families* (or *generations*). The main properties of these particles are summarised in Table 1.1 [3].

There are also six antileptons, with all the sign for the quantum numbers reversed. Neutrinos are massless in the Standard Model, however neutrino oscillations demonstrate they have a small but non-zero mass [4, 5].

Generation	Name	Q	L_e	L_μ	L_τ	Mass
1	e	-1	1	0	0	0.511 MeV/c ²
	ν_e	0	1	0	0	< 2 eV/c ²
2	μ	-1	0	1	0	105.758 MeV/c ²
	ν_μ	0	0	1	0	< 2 eV/c ²
3	τ	-1	0	0	1	1776.82 MeV/c ²
	ν_τ	0	0	0	1	< 2 eV/c ²

Table 1.1: Main properties of leptons [3].

Generation	Name (flavour)	Q	S	C	B	T	Mass
1	u	$+\frac{2}{3}$	0	0	0	0	$2.3_{-0.5}^{+0.7}$ MeV/c ²
	d	$-\frac{1}{3}$	0	0	0	0	$4.8_{-0.3}^{+0.5}$ MeV/c ²
2	c	$+\frac{2}{3}$	0	1	0	0	1.275 ± 0.025 GeV/c ²
	s	$-\frac{1}{3}$	-1	0	0	0	95 ± 5 MeV/c ²
3	t	$+\frac{2}{3}$	0	0	0	1	$173.21 \pm 0.51 \pm 0.71$ GeV/c ²
	b	$-\frac{1}{3}$	0	0	-1	0	4.18 ± 0.03 GeV/c ²

Table 1.2: Main properties of quarks. The mass quoted for t quark derives from direct measurement, while the b -mass is an estimate of the so-called “current-quark mass” [3].

Quarks are organised in a similar way, and are classified according to their charge, strangeness (S), charm (C), beauty (B), and top (T), as can be seen in Table 1.2. Quarks are fermions but, unlike leptons, they carry fractionary electric charge. Also quarks have antiquark counterparts. Quarks have an additional quantum number that is called *colour* and that is the source of the strong interaction: each quark and antiquark comes in three colours, namely red (r), green (g), and blue (b). The quarks combine to form “white” composite particles, mesons (quark and antiquark of colour and complementary colour, respectively) and baryons (three quark of different colours). It is important to notice that the quark eigenstates of mass are not eigenstates for the weak interaction, the latter being a linear combination of the former. This *mixing* between quark generations is summarised in the Cabibbo-Kobayashi-Maskawa (CKM) matrix [6] and will be explained in more detail in the following section.

Interaction	Name	Mass	Spin
Strong	g	0	1
Electromagnetic	γ	0	1
Weak	W^\pm	$80.385 \pm 0.015 \text{ GeV}/c^2$	1
	Z^0	$91.1876 \pm 0.0021 \text{ GeV}/c^2$	1
-	H^0	$125.7 \pm 0.4 \text{ GeV}/c^2$	0

Table 1.3: Main properties of gauge and Higgs bosons.

Finally, every mediator is responsible for an interaction: the photon (γ) for the electromagnetic force, a positive and a negative W and also a Z^0 for the weak force, and for the strong force the gluon (g , which comes in eight combinations of the colours already named for quarks). The graviton is presumably responsible for gravity but, as already said, gravitational force is not included in the Standard Model. These particles of integer spin are called *bosons*. Related to how mass is assigned to elementary particles in the SM, the Glashow-Weinberg-Salam theory calls for at least one Higgs boson. A candidate for the Higgs particle (H^0) was discovered by the ATLAS and CMS collaboration in 2012 [7, 8, 9]. A summary of the properties of these particles is presented in Table 1.3.

In the Standard Model all the fundamental interactions derive from a single general principle, the *local gauge invariance*, in this case with respect to the symmetry group $SU(3)_C \otimes SU(2)_L \otimes U(1)_Y$. For each interaction, the invariance of the Lagrangian under the respective transformation leads to the conservation of a quantum number, represented in the above formula by the subscripts.

The $SU(3)_C$ is the non-abelian gauge symmetry group for the QCD and describes the strong interaction among quarks. The conserved quantum number is the colour (C) and the mediator is the gluon. The gauge transformation for gluonic fields is complicated by the non-abelian structure of $SU(3)$, which is responsible for gluon self-interaction. Two features descend from the structure of this group: *asymptotic freedom*, which is an “antiscreening” of the colour charge resulting in the fact that two quarks of the same colour interact through colour fields of reduced strength and asymptotically behave as free, noninteracting particles; and *confinement*, related to the fact that all the particles or quark bound states that can be observed are colour singlets (colourless), and this explains the exclusive detection of qqq , $\bar{q}\bar{q}\bar{q}$,

and $q\bar{q}$ quark combinations¹.

The description of electroweak interaction must include fermions of different flavours and properties with their right-handed and left-handed fields, where left-handed fermions must appear paired; it must include the photon, which is massless, together with massive gauge bosons, W^\pm and Z^0 . The simplest way to represent electroweak interactions is $SU(2)_L \otimes U(1)_Y$. Associated to the weak $SU(2)$ group are the gauge bosons W_i , $i = 1, 2, 3$, and the conserved quantum number is the weak isospin T . This theory is called *chiral*, which means that left-handed fermions (and right-handed anti-fermions) couple to the gauge boson and have a nonzero weak isospin, while right-handed fermions (and left-handed anti-fermions) are isospin singlets. The subscript L in the group notation is to remind us the exclusive coupling with *left-handed* fermions. The $U(1)$ group has the associated gauge boson A and the subscript Y refers to the associated quantum number, also called *weak hypercharge*, defined as:

$$Y = 2(Q - T_3) \quad (1.1)$$

where T_3 is the third component of the *weak isospin*. The four mentioned gauge bosons (W_1 , W_2 , W_3 , and B) acquire mass through the Higgs mechanism. In particular, the mixing of W_3 and B forms the Z^0 boson and the photon, while the W_1 and W_2 fields mix to form the charged W^+ and W^- bosons. In the mixing, only the photon remains massless. The weak interactions can be distinguished in a *charged current* (CC) interaction, which is mediated by the charged bosons W^\pm , and in a *neutral current* (NC) interaction mediated by the exchange of a Z^0 boson where only fermions of the same family can participate. In fact, *flavour changing neutral currents* (FCNC) interactions can only happen with the exchange of a gluon and for this reason they are suppressed in the SM due to the Glashow-Iliopoulos-Maiani (GIM) mechanism.

The derivation of the Lagrangian of the Standard Model starting from the ingredients here presented can be found on [1]. The final result can be expressed as:

$$\mathcal{L} = -\frac{1}{4}F_{\mu\nu}F^{\mu\nu} + \bar{\psi}\not{D}\psi + \mathcal{L}_{Yukawa} + (D_\mu\Phi)^\dagger(D^\mu\Phi) - V(\Phi). \quad (1.2)$$

¹Although already demonstrated, the existence of exotic states is not included here as it can be explained as an aggregate of the already described quark combinations.

Here $F^{\mu\nu}$ represents the bosonic gauge fields, ψ the fermionic fields and Φ the Higgs fields pair. The terms in Eq. 1.2 can be explained as follows [10]:

- $-\frac{1}{4}F_{\mu\nu}F^{\mu\nu}$ represents the kinetic term for the gauge bosons;
- $\bar{\psi}\not{D}\psi$: thanks to the covariant derivative, the kinetic term for fermions include both the couplings between fermions and the couplings of fermions with gauge bosons;
- \mathcal{L}_{Yukawa} : the Lagrangian cannot include an explicit mass term for the fermions, for it would mix left-handed and right-handed particles. The problem is solved including the Higgs doublet, so that the Yukawa terms include the mass terms and the coupling of fermions with Higgs terms, which are proportional to the squared mass of the considered fermion;
- $(D_\mu\Phi)^\dagger(D^\mu\Phi) - V(\Phi)$: these represent the kinetic and potential terms for the Higgs fields, respectively; the Higgs doublet Lagrangian part contains a kinetic term, which will generate the gauge boson masses and interactions between the Higgs and the gauge bosons, and a “spontaneous symmetry breaking” potential, which will give the Higgs a vacuum expectation value and self-interactions.

1.2 The GIM mechanism

When describing the three quark families in Sec. 1.1 we started from the end of the story: in the first picture of the quark sector, only three quarks were involved, namely the doublet $\begin{pmatrix} u \\ d \end{pmatrix}$ and the singlet s . As long as the fundamental quark vertex was allowed to operate only *within* each generation, the observed strangeness-changing weak decays like $K^+ \rightarrow \mu^+\nu_\mu$ were impossible to explain. The solution to this dilemma was suggested by Cabibbo in 1963, applied to neutral processes by Glashow, Iliopoulos and Maiani in 1970 and extended to three quark generations by Kobayashi and Maskawa in 1973 (see Sec. 1.3). Cabibbo introduced a mixing angle θ_C and suggested that the $d \rightarrow u + W^-$ carries a factor of $\cos\theta_C$, while $s \rightarrow u + W^-$ carries a factor of $\sin\theta_C$. Early measurements of the semi-leptonic decay rates of strange particles with a change in strangeness $\Delta S = 1$ shown that they were suppressed by a factor of ≈ 20 as compared with $\Delta S = 0$ decays, so evidently the Cabibbo angle is rather small. Its value has been experimentally found

to be $\theta_C = 13.1^\circ$. Transitions can be now classified as *Cabibbo-favoured* (where the factor $\cos \theta_C$ appears) and *Cabibbo-suppressed* (where the proportionality to $\sin \theta_C$ appears). However, the three-quark scheme predicts a flavour-changing neutral current decay, $K_L \rightarrow \mu^+ \mu^-$, whose amplitude should be proportional to $\sin \theta_C \cos \theta_C$, but that was totally excluded by the data. To solve this paradox, Glashow, Iliopoulos and Maiani [11] introduced a fourth quark charged $+2/3$, c , four years before the first direct experimental evidence for charm, whose weak couplings to d and s carry factors of $\cos \theta_C$ and $-\sin \theta_C$, respectively. For each u -line exchanged, the c quark introduces a second diagram with a coupling of the opposite sign. Were the masses of the two quark equal, the two diagrams would exactly cancel; instead, the amplitude for the process is proportional to the difference of the squared masses of quarks in the loop, $m_c^2 - m_u^2$.

1.3 The CKM matrix

Leptonic weak interaction only involves members of the same generation: e^- converts to ν_e with emission of W^- , or $\mu^- \rightarrow \mu^-$ with a Z^0 mediator, but e^- never goes to μ^- nor μ^- goes to ν_e , so the leptonic family number is conserved. The same rule does not apply to the quarks: while the colour is conserved in the interaction, the flavour changes. The “missing” flavour is not carried by the mediator, similarly to what happens with the colour with the emission of a gluon, rather, flavour is not conserved in weak interactions. Quarks generations are mixed by the weak interactions inasmuch mass eigenstates do not correspond to weak interaction eigenstates. As disclosed in the previous section, the unitary Cabibbo-Kobayashi-Maskawa (CKM) matrix couples quark fields of different flavours as

$$\begin{pmatrix} d' \\ s' \\ b' \end{pmatrix} = \begin{pmatrix} V_{ud} & V_{us} & V_{ub} \\ V_{cd} & V_{cs} & V_{cb} \\ V_{td} & V_{ts} & V_{tb} \end{pmatrix} \begin{pmatrix} d \\ s \\ b \end{pmatrix}, \quad (1.3)$$

where $(d' \ s' \ b')$ are the weak interaction eigenstates and $(d \ s \ b)$ are the mass eigenstates; the matrix elements, $V_{qq'}$ are thus the amplitudes for the couplings to the W^\pm mediators, and the quantity $|V_{qq'}|^2$ is proportional to the probability for the transition $q \rightarrow q'$. The value for the elements in the CKM matrix cannot be predicted from SM principles and must be experimentally determined.

The V_{CKM} matrix has 18 free parameters (9 complex elements), which are reduced to 9 due to the unitarity constraint. Five degrees of freedom can be absorbed into non-observable quark field phases. The remaining 4 parameters can be chosen as three angles, θ_{12} , θ_{23} , θ_{31} , and one complex phase, δ . The quark sector of the Standard Model is not invariant under charge conjugation (C) and parity operations (P) unless all the elements of V_{CKM} are real. With the chosen parameterisation, this implies the phase angle δ to be zero. Shortening $\cos \theta_{ij} = c_{ij}$ and $\sin \theta_{ij} = s_{ij}$, the CKM matrix can be written as:

$$V_{CKM} = \begin{pmatrix} c_{12}c_{13} & s_{12}c_{13} & s_{13}e^{-i\delta} \\ -s_{12}c_{23} - c_{12}s_{23}s_{13}e^{i\delta} & c_{12}c_{23} - s_{12}s_{23}s_{13}e^{i\delta} & s_{23}c_{13} \\ s_{12}s_{23} - c_{12}c_{23}s_{13}e^{i\delta} & -c_{12}s_{23} - s_{12}c_{23}s_{13}e^{i\delta} & c_{23}c_{13} \end{pmatrix}. \quad (1.4)$$

It is well known experimentally that $s_{13} \ll s_{23} \ll s_{12} \ll 1$. The Wolfenstein parameterisation [12] highlights this hierarchy with the following substitutions:

$$\lambda = s_{12}, \quad A = \frac{s_{23}}{s_{12}^2}, \quad (1.5)$$

$$\rho = \frac{s_{13}c_{\delta}}{s_{12}s_{23}}, \quad \eta = \frac{s_{13}s_{\delta}}{s_{12}s_{23}}, \quad (1.6)$$

and the CKM matrix can be re-written as a power expansion of the parameter $\lambda \approx 0.22$ as follows:

$$V_{CKM} = \begin{pmatrix} 1 - \lambda^2/2 & \lambda & A\lambda^3(\rho - i\eta) \\ -\lambda & 1 - \lambda^2/2 & A\lambda^2 \\ A\lambda^3(1 - \rho - i\eta) & -A\lambda^2 & 1 \end{pmatrix} + \mathcal{O}(\lambda^4). \quad (1.7)$$

The unitarity condition $VV^\dagger = \mathbf{1}$ translates in $\sum_i V_{ij}V_{ik}^* = \delta_{ik}$ and $\sum_j V_{ij}V_{kj}^* = \delta_{ik}$. The six vanishing combinations can be graphically represented in the complex plane ($\bar{\rho}$, $\bar{\eta}$) as triangles having very different shape but same area, directly proportional to the Jarlskog invariant, J , the CP violation parameter of the CKM matrix. A common choice is to use one of the two less scalene of the unitarity triangles, in which all the sides (and thus all the internal angles) are of the same order of magnitude, λ , which comes from the relation:

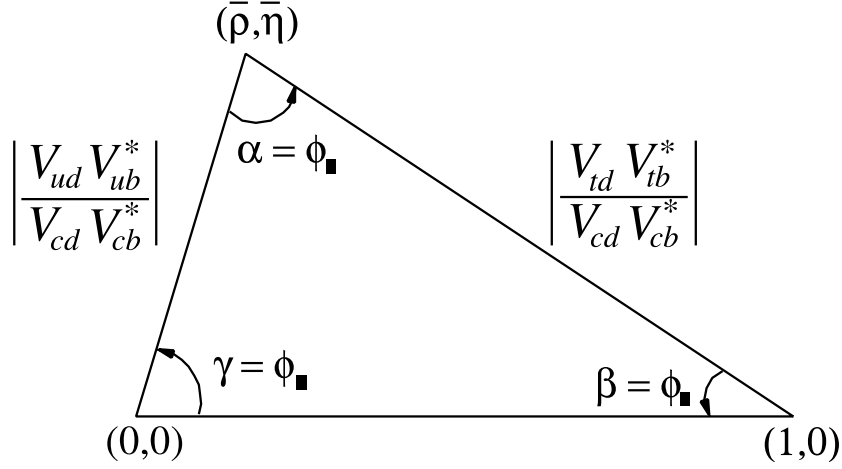


Figure 1.1: Sketch of a unitarity triangle.

$$V_{ud}V_{ub}^* + V_{cd}V_{cb}^* + V_{td}V_{tb}^* = 0, \quad (1.8)$$

and which is displayed in Fig. 1.1 dividing each side by $V_{cd}V_{cb}^*$. The angles are immediately obtained from Fig. 1.1 as [3]

$$\beta = \phi_1 = \arg \left(-\frac{V_{cd}V_{cb}^*}{V_{td}V_{tb}^*} \right), \quad (1.9)$$

$$\alpha = \phi_2 = \arg \left(-\frac{V_{td}V_{tb}^*}{V_{ud}V_{ub}^*} \right), \quad (1.10)$$

$$\gamma = \phi_3 = \arg \left(-\frac{V_{ud}V_{ub}^*}{V_{cd}V_{cb}^*} \right). \quad (1.11)$$

Both frequentist statistics and Bayesian approaches are used to combine the experimental data to determine the CKM matrix elements and they obtain similar results. The fit for the Wolfenstein parameters presented in Eq. 1.6 using a Bayesian approach provides the results:

$$\begin{aligned} \lambda &= 0.2255 \pm 0.0006, & A &= 0.818 \pm 0.015 \\ \bar{\rho} &= 0.124 \pm 0.024 & \bar{\eta} &= 0.354 \pm 0.015. \end{aligned} \quad (1.12)$$

1.4 CP violation in the quark sector

The operation of the spatial inversion of coordinates is a discrete transformation and is produced by the parity operator P :

$$P\psi(x, y, z) = \psi(-x, -y, -z). \quad (1.13)$$

When it exists, the eigenvalue of the operator will be ± 1 and it is called the *parity* of the system. On fermions, P has the effect of transforming left-handed particles in right-handed particles and vice versa.

The operation of charge conjugation C reverses the sign of all the internal quantum numbers of a particle while leaving mass, energy, momentum and spin unchanged. In relativistic quantum mechanics, charge conjugation also implies the interchange of particles and antiparticles like

$$C|p\rangle = |\bar{p}\rangle. \quad (1.14)$$

As with P , the eigenvalues of C are ± 1 but in this case most of the particles are not eigenstates of C , because $|p\rangle$ and $|\bar{p}\rangle$ differ at most by a sign².

Electromagnetic and strong interactions are experimentally invariant under the P and C operations. This has been demonstrated not to be the case of weak interactions [13]; as an example, the antimuon emitted in pion decay:

$$\pi^+ \rightarrow \mu^+ \nu_\mu^+ \quad (1.15)$$

is *always* left-handed, demonstrating that weak interactions are not invariant under parity transformation. The charge-conjugated decay would be:

$$\pi^- \rightarrow \mu^- \bar{\nu}_\mu \quad (1.16)$$

with a left-handed muon; instead the muon *always* comes out right-handed. In this sense P and C are said to be *maximally* violated in weak interactions. By contrast, *combining* the two operations the left-handed antimuon turns into a right-handed muon, which is exactly what can be observed in nature. However CP violation exists but is a small effect, which has been observed for the first time thanks to bizarre implications for neutral K mesons [14], as they are typically produced in strong interactions as eigenstates of strangeness (K^0 and \bar{K}^0) but they decay by weak interactions as eigenstates of CP (K_1 and K_2). The CP -violating effect have been also observed in recent years in B decays where they are larger. Although predicted, CP violation is not yet experimentally established in the D system.

²This means that only particles that coincide with their own antiparticles can be eigenstates of C .

In the following, a general formalism for CP violation in the decay of a weakly decaying meson M (which can be a $K^0, B_{(s)}^0$, or a D^0) is presented.

Given the Hamiltonian \mathcal{H} for the weak interactions, the decay amplitudes of M and of its CP conjugate \bar{M} to a generic multi-particle final state f and its CP conjugate \bar{f} can be written as

$$A_f = \langle f | \mathcal{H} | M \rangle, \quad \bar{A}_f = \langle f | \mathcal{H} | \bar{M} \rangle, \quad (1.17)$$

$$A_{\bar{f}} = \langle \bar{f} | \mathcal{H} | M \rangle, \quad \bar{A}_{\bar{f}} = \langle \bar{f} | \mathcal{H} | \bar{M} \rangle. \quad (1.18)$$

Applying CP to these states introduces the phases³ ξ_M and ξ_f according to:

$$CP|M\rangle = e^{+i\xi_M}|\bar{M}\rangle, \quad CP|f\rangle = e^{+i\xi_f}|\bar{f}\rangle \quad (1.19)$$

and also

$$CP|\bar{M}\rangle = e^{-i\xi_M}|M\rangle, \quad CP|\bar{f}\rangle = e^{-i\xi_f}|f\rangle \quad (1.20)$$

to guarantee $(CP)^2 = 1$. CP conservation implies $[CP, \mathcal{H}] = 0$, then A_f and $\bar{A}_{\bar{f}}$ have the same magnitude and an arbitrary unphysical relative phase given by $\xi_f - \xi_M$.

Starting from a state that is a superposition of M^0 and \bar{M}^0 states⁴ at $t = 0$,

$$|\psi(0)\rangle = a(0)|M^0\rangle + b(0)|\bar{M}^0\rangle, \quad (1.21)$$

its temporal evolution will include components describing all possible decay final states $\{f_1, f_2, \dots\}$,

$$|\psi(t)\rangle = a(t)|M^0\rangle + b(t)|\bar{M}^0\rangle + c_1(t)|f_1\rangle + c_2(t)|f_2\rangle + \dots \quad (1.22)$$

The formalism for only determining $a(t)$ and $b(t)$ is simplified for t much larger than the typical strong interaction scale. The time evolution is thus

³The phases ξ_M and ξ_f are arbitrary and unobservable because of the flavour symmetry of the strong interaction.

⁴The superscript 0 highlights that, contrary to the lines before, this part is only valid for neutral mesons.

determined by a 2×2 effective non-Hermitian Hamiltonian \mathbf{H} that can be written in terms of two Hermitian matrices, \mathbf{M} and $\mathbf{\Gamma}$, as

$$\mathbf{H} = \mathbf{M} - \frac{i}{2}\mathbf{\Gamma} = \begin{pmatrix} M_{11} - \frac{i}{2}\Gamma_{11} & M_{21} - \frac{i}{2}\Gamma_{21} \\ M_{21} - \frac{i}{2}\Gamma_{21} & M_{22} - \frac{i}{2}\Gamma_{22} \end{pmatrix}. \quad (1.23)$$

Diagonal elements are associated with flavour-conserving transitions, while off-diagonal elements are associated with flavour-changing transitions. The eigenvectors of \mathbf{H} are mass eigenstates (the lightest being M_L , and the heaviest M_H) and can be expressed in terms of the strong interaction eigenstates introducing the three complex parameters p , q and z ⁵

$$|M_L\rangle \propto p\sqrt{1-z}|M^0\rangle + q\sqrt{1+z}|\bar{M}^0\rangle, \quad (1.24)$$

$$|M_H\rangle \propto p\sqrt{1+z}|M^0\rangle - q\sqrt{1-z}|\bar{M}^0\rangle, \quad (1.25)$$

$$(1.26)$$

where $|q|^2 + |p|^2 = 1$ when $z = 0$. The real and the imaginary part of the eigenvalues $\omega_{L,H}$ corresponding to $M_{L,H}$ represent their masses and decay widths, respectively, hence the mass and width splittings can be written as

$$\Delta m = m_H - m_L = \text{Re}(\omega_H - \omega_L), \quad (1.27)$$

$$\Delta\Gamma = \Gamma_H - \Gamma_L = -2\text{Im}(\omega_H - \omega_L). \quad (1.28)$$

$$(1.29)$$

Solving the eigenvalue problem for \mathbf{H} yields

$$\left(\frac{q}{p}\right)^2 = \frac{M_{12}^* - (i/2)\Gamma_{12}^*}{M_{12} - (i/2)\Gamma_{12}} \quad (1.30)$$

and

$$z = \frac{\delta m - (i/2)\delta\Gamma}{\Delta m - (i/2)\Delta\Gamma} \quad (1.31)$$

where $\delta m \equiv M_{11} - M_{22}$ and $\delta\Gamma \equiv \Gamma_{11} - \Gamma_{22}$ being the mass and the decay width differences for the strong eigenstates M^0 and \bar{M}^0 . If either CP or

⁵For K mesons the standard choice is to label the eigenstates according to their lifetimes, thus identifying the short-lived state K_S with the lighter and the long-lived state K_L with the heavier state.

CPT is a symmetry of \mathbf{H} , δm and $\delta\Gamma$ are both zero, hence $z = 0$. If either CP or T is a symmetry of \mathbf{H} , the ratio Γ_{12}/M_{12} is real, hence

$$\left(\frac{q}{p}\right)^2 = e^{2i\xi_M} \Rightarrow \left|\frac{q}{p}\right| = 1. \quad (1.32)$$

In case of conserved CP , both the above conditions are true and the mass eigenstates are orthogonal

$$\langle M_H | M_L \rangle = |p|^2 - |q|^2 = 0. \quad (1.33)$$

The CP violation can occur in the quark sector in three ways:

- CP -violation in decay: this is the only possible source of CP asymmetries in charged meson decays, where there is no mixing. There is CP -violation in decay when the probability for $M \rightarrow f$ is different from the probability for $\bar{M} \rightarrow \bar{f}$, that is

$$\left|\frac{\bar{A}_{\bar{f}}}{A_f}\right| \neq 1 \quad (1.34)$$

and the CP -violation is said to have occurred *directly*. It can be observed measuring the quantity

$$\mathcal{A}_{f\bar{f}} = \frac{\Gamma(M \rightarrow f) - \Gamma(\bar{M} \rightarrow \bar{f})}{\Gamma(M \rightarrow f) + \Gamma(\bar{M} \rightarrow \bar{f})} = \frac{|\bar{A}_{\bar{f}}/A_f|^2 - 1}{|\bar{A}_{\bar{f}}/A_f|^2 + 1}; \quad (1.35)$$

- CP -violation in mixing: this type of CP -violation only occurs in neutral particles, and is the only source of CP violation in charged-current semileptonic neutral meson decays $M, \bar{M} \rightarrow l^\pm X$. It implies that the probability for $M^0 \rightarrow \bar{M}^0$ is different from the probability for $\bar{M}^0 \rightarrow M^0$. In this case

$$\left|\frac{q}{p}\right| \neq 1. \quad (1.36)$$

CP -violation in mixing can be accessed in the asymmetry from the rate of “wrong” final states due to oscillations:

$$\begin{aligned}
\mathcal{A}_{f\bar{f}}(t) &= \frac{d\Gamma/dt(\bar{M}^0(t) \rightarrow l^+ X) - d\Gamma/dt(M^0(t) \rightarrow l^- X)}{d\Gamma/dt(\bar{M}^0(t) \rightarrow l^+ X) + d\Gamma/dt(M^0(t) \rightarrow l^- X)} \\
&= \frac{1 - |q/p|^4}{1 + |q/p|^4}; \tag{1.37}
\end{aligned}$$

- *CP*-violation in interference between mixing and decay, which can occur when both M and \bar{M} have access to a common final state f . In this case f can be reached in two ways: with a direct decay $M^0 \rightarrow f$; with a decay after the mixing $M^0 \rightarrow \bar{M}^0 \rightarrow f$. Defining

$$\lambda_f = \frac{q \bar{A}_f}{p A_f} \tag{1.38}$$

the condition for this type of *CP*-violation is

$$\text{Im}(\lambda_f) \neq 0. \tag{1.39}$$

This form of *CP*-violation can be observed measuring the asymmetry of neutral meson decays into final *CP* eigenstates f_{CP}

$$\mathcal{A}_{f_{CP}}(t) = \frac{d\Gamma/dt(\bar{M}^0(t) \rightarrow f_{CP}) - d\Gamma/dt(M^0(t) \rightarrow f_{CP})}{d\Gamma/dt(\bar{M}^0(t) \rightarrow f_{CP}) + d\Gamma/dt(M^0(t) \rightarrow f_{CP})}. \tag{1.40}$$

If $|q/p| = 1$ and $\Delta\Gamma = 0$, as happens to a good approximation for B^0 , but not for K^0 and B_s^0 , then the expression for 1.40 reduces to a simple form

$$\mathcal{A}_{f_{CP}}(t) = S_{f_{CP}} \sin(\Delta mt) - C_{f_{CP}} \cos(\Delta mt) \tag{1.41}$$

with

$$S_{f_{CP}} \equiv \frac{2\text{Im}(\lambda_f)}{1 + |\lambda_f|^2}, \quad C_{f_{CP}} = \frac{1 - |\lambda_f|^2}{1 + |\lambda_f|^2}. \tag{1.42}$$

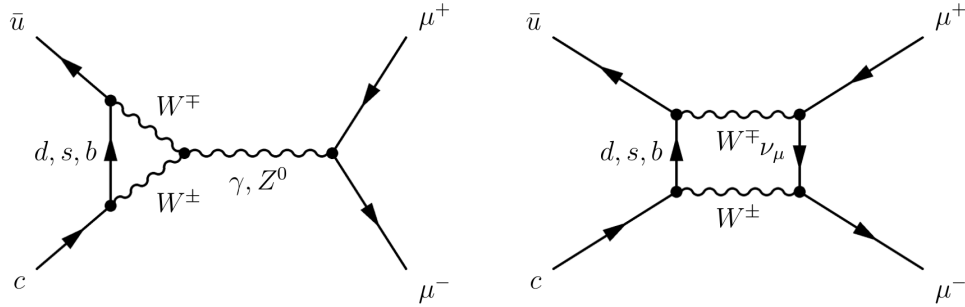


Figure 1.2: Feynman diagrams of two possible Standard Model contributions to the $D^0 \rightarrow \mu^+ \mu^-$ decay.

1.5 Rare decays and the $D^0 \rightarrow \mu^+ \mu^-$ case

The adjective “rare” is associated to decays whose branching fraction (BF) is of the order of 10^{-5} or less, hence to decays that are due to highly suppressed processes within the Standard Model. This category includes FCNC processes, which proceed via an internal quark loop but are forbidden at the tree level in the SM, and forbidden processes involving quantum numbers violation. Phase-space suppression or GIM-mechanism suppression can contribute to a further reduction in the branching fraction.

The study of very suppressed beauty and charmed meson decays allows to search for any unpredicted enhancement of their BF’s due to unexpected contributions from New Physics (NP) processes. For forbidden processes, their observation would be unequivocally a signature of NP.

In the SM, the decay $D^0 \rightarrow \mu^+ \mu^-$ belongs to the category of FCNC processes and proceed via a W box diagram, which also contributes to D^0 – \bar{D}^0 mixing, being forbidden at tree level; in addition to this, it is also highly suppressed by the GIM mechanism and by a factor of m_μ^2/m_D^2 due to helicity. Feynman diagrams of two possible Standard Model contributions are shown in Fig. 1.2.

How does the study of D particle differ from that of mesons containing other heavy quarks? The suppression introduced by the GIM-mechanism in the $D^0 \rightarrow \mu\mu$ decay does not have a contribution from t quark in the loop, thus it is stronger than for B mesons, facilitating the observation of NP effects, which can be of the same order of SM contributions. Complications arise from the necessity to separate perturbation terms in heavy-quark

effective theories (HQET) that are usually reintroduced as non-perturbative corrections. This approach works for *heavy* quarks, whose mass is larger than the strong interaction scale $\Lambda_{QCD} \sim 0.2$ GeV. The dimensional parameter Λ_{QCD} sets the scale at which the coupling constant becomes large and the physics can be treated in a non-perturbative way; actually it sets the scale for strong interaction physics. While the b quark is heavy compared to the intrinsic scale of strong interactions ($m_b \gg \Lambda_{QCD}$), $m_c \sim \Lambda_{QCD}$ and this does not allow to simply neglect higher order terms in the expansion in $1/m_q$ (where m_q is the mass of the heaviest quark in the meson) in the heavy-quark effective theory. A typical approach for the construction of a heavy-quark effective theory consists in using the operator product expansion (OPE) starting from the original QCD Hamiltonian, which is formulated at very short distance. In this way we get an Effective Hamiltonian in the form

$$\mathcal{H}_{eff} \propto \sum_n C_n(\mu) \mathcal{O}_n(\mu), \quad (1.43)$$

which is expanded into a set of Wilson coefficients $C_n(\mu)$, containing all information about short-distance physics above the renormalisation scale μ , and of operators $\mathcal{O}_n(\mu)$, which determine the couplings of quarks and particles in the decay. The operators are divided into five classes:

- current-current operators, \mathcal{O}_1 and \mathcal{O}_2 :

$$\mathcal{O}_1 = (\bar{u}_L^\alpha \gamma_\mu q_L^\beta) (\bar{q}_L^\beta \gamma^\mu c_L^\alpha), \quad \mathcal{O}_2 = (\bar{u}_L^\alpha \gamma_\mu q_L^\alpha) (\bar{q}_L^\beta \gamma^\mu c_L^\beta), \quad (1.44)$$

where $q = d, s, b$ and α, β are contracted color indices;

- QCD-penguins operators, \mathcal{O}_3 – \mathcal{O}_6 :

$$\begin{aligned} \mathcal{O}_3 &= (\bar{u}_L^\alpha \gamma_\mu c_L^\alpha) \sum_q (\bar{q}_L^\beta \gamma^\mu q_L^\beta), & \mathcal{O}_4 &= (\bar{u}_L^\alpha \gamma_\mu c_L^\beta) \sum_q (\bar{q}_L^\beta \gamma^\mu q_L^\alpha), \\ \mathcal{O}_5 &= (\bar{u}_L^\alpha \gamma_\mu c_L^\alpha) \sum_q (\bar{q}_R^\beta \gamma^\mu q_R^\beta), & \mathcal{O}_6 &= (\bar{u}_L^\alpha \gamma_\mu c_L^\beta) \sum_q (\bar{q}_R^\beta \gamma^\mu q_R^\alpha), \end{aligned} \quad (1.45)$$

where the gluon emission implies the participation of both left (L) and right (R) $q\bar{q}$ components;

- electromagnetic and chromomagnetic dipole operators, \mathcal{O}_7 and \mathcal{O}_8 :

$$\mathcal{O}_7 = \frac{e}{16\pi^2} m_c (\bar{u}_L \sigma_{\mu\nu} c_R) F^{\mu\nu}, \quad \mathcal{O}_8 = \frac{g_s}{16\pi^2} m_c (\bar{u}_L \sigma_{\mu\nu} T^a c_R) G_a^{\mu\nu}; \quad (1.46)$$

- semi-leptonic operators, \mathcal{O}_9 and \mathcal{O}_{10} :

$$\mathcal{O}_9 = \frac{e^2}{16\pi^2} (\bar{u}_L \gamma_\mu c_L) (\bar{l} \gamma^\mu l), \quad \mathcal{O}_{10} = \frac{e^2}{16\pi^2} (\bar{u}_L \gamma_\mu c_L) (\bar{l} \gamma^\mu \gamma^5 l). \quad (1.47)$$

Together with \mathcal{O}_7 , these are the main contributions to short distance processes in $D^0 \rightarrow \mu^+ \mu^-$.

For the $D^0 \rightarrow \mu\mu$ short distance contribution it is convenient to use an effective description with the W boson and the b being integrated out as their thresholds are reached [15]:

$$\begin{aligned} \mathcal{H}_{eff} &= -\frac{4G_F}{\sqrt{2}} \left[\sum_{q=d,s,b} C_1^{(q)}(\mu) \mathcal{O}_1^{(q)}(\mu) + C_2^{(q)}(\mu) \mathcal{O}_2^{(q)}(\mu) + \sum_{i=3}^{10} C_i(\mu) \mathcal{O}_i(\mu) \right], \\ &\quad m_b < \mu < M_W \\ \mathcal{H}_{eff} &= -\frac{4G_F}{\sqrt{2}} \left[\sum_{q=d,s} C_1^{(q)}(\mu) \mathcal{O}_1^{(q)}(\mu) + C_2^{(q)}(\mu) \mathcal{O}_2^{(q)}(\mu) + \sum_{i=3}^{10} C'_i(\mu) \mathcal{O}'_i(\mu) \right], \\ &\quad \mu < m_b, \end{aligned} \quad (1.48)$$

where the primed quantities indicate where the b has been eliminated (while all the terms of order $1/M_W^2$ above $\mu = m_b$ are retained), and where the dependence on the CKM matrix elements is contained in the Wilson coefficients.

The $D^0(p) \rightarrow \mu^+(k_+, s_+) \mu^-(k_-, s_-)$ (p and k_\pm are the momenta and s_\pm the polarisations) decay amplitude matrix can be expressed as

$$\mathcal{M}_{D^0 \rightarrow \mu^+ \mu^-} = \bar{u}(k_-, s_-) [A_{D^0 \rightarrow \mu^+ \mu^-} + \gamma_5 B_{D^0 \rightarrow \mu^+ \mu^-}] v(k_+, s_+), \quad (1.49)$$

and the decay amplitude is then calculated to be

$$\Gamma_{D^0 \rightarrow \mu^+ \mu^-} = \frac{M_D}{8\pi} \sqrt{1 - 4 \frac{m_\mu^2}{M_D^2}} \left[|A_{D^0 \rightarrow \mu^+ \mu^-}|^2 + \left(1 - 4 \frac{m_\mu^2}{M_D^2}\right) |B_{D^0 \rightarrow \mu^+ \mu^-}|^2 \right]. \quad (1.50)$$

While the $A_{D^0 \rightarrow \mu^+ \mu^-}$ term cancels, in the $B_{D^0 \rightarrow \mu^+ \mu^-}$ term a short-distance and a long-distance contribution can be derived. We thus obtain

$$B_{D^0 \rightarrow \mu^+ \mu^-}^{(\text{s.d.})} \simeq \frac{G_F^2 M_W^2 f_D m_\mu}{\pi^2} F, \quad (1.51)$$

for the short-distance contribution, where

$$F = \sum_{q=d,s,b} V_{uq} V_{cq}^* \left[\frac{x_q}{2} + \frac{\alpha_s}{4\pi} x_q \cdot \left(\ln^2 x_q + \frac{4 + \pi^2}{3} \right) \right], \quad (1.52)$$

and the term $x_q = m_q^2/M_W^2$. In the expression for F , the mass of the leptons in the final state (here m_μ) appears, making the helicity suppression mechanism explicit. The branching fraction for this contribution is

$$\mathcal{B}^{(\text{s.d.})}(D^0 \rightarrow \mu^+ \mu^-) \simeq 10^{-18}. \quad (1.53)$$

The long-distance contribution takes into account the case of a single intermediate particle,

$$B_{D^0 \rightarrow \mu^+ \mu^-}^{(\text{l.d., mix})} = \sum_{P_n} \langle P_n | \mathcal{H} | D^0 \rangle \frac{1}{M_D^2 - M_{P_n}^2} B_{P_n \rightarrow \mu^+ \mu^-}, \quad (1.54)$$

where $P_n = \pi^0, \eta, \eta'$ is the intermediate particle and $B^{(\text{mix})} = B^{(\text{ground state})} + B^{(\text{resonant state})}$ and which contributes as

$$\mathcal{B}^{(\text{l.d., single particle})}(D^0 \rightarrow \mu^+ \mu^-) \simeq 2.5 \cdot 10^{-18}, \quad (1.55)$$

and the case of a two-photon intermediate state, obtained starting from the branching fraction of $D^0 \rightarrow \gamma\gamma$ as

$$\mathcal{B}^{(\text{l.d., } \gamma\gamma)}(D^0 \rightarrow \mu^+ \mu^-) \simeq 2.7 \cdot 10^{-5} \mathcal{B}(D^0 \rightarrow \gamma\gamma). \quad (1.56)$$

where $\mathcal{B}(D^0 \rightarrow \gamma\gamma) < 8.5 \cdot 10^{-7}$ at CL = 90% [16], thus

$$\mathcal{B}^{(\text{l.d., } \gamma\gamma)}(D^0 \rightarrow \mu^+ \mu^-) \lesssim 2.3 \cdot 10^{-11} \text{ at } 90\% \text{ C.L.} \quad (1.57)$$

The current upper limit has been fixed by the LHCb experiment to be [17]

$$\mathcal{B}(D^0 \rightarrow \mu^+ \mu^-) < 6.2(7.6) \cdot 10^{-9} \text{ at 90\% (95\%) C.L.} \quad (1.58)$$

using a data sample corresponding to an integrated luminosity of 0.9 fb^{-1} of pp collisions collected during 2011 at a center-of-mass energy of 7 TeV. The experimental limit is therefore two orders of magnitude greater than the sensitivity of the theoretical prediction, with a strong contribution to the statistical error attributable to particle misidentification.

Different processes due to physics beyond the Standard Model could contribute to the decay channel $D^0 \rightarrow \mu^+ \mu^-$. Some of them could enhance the short-distance effects of several orders of magnitude, like those described by R -parity violating models [15, 18] and models with Randall-Sundrum warped extra dimensions [19].

The LHCb experiment

2.1 The Large Hadron Collider

The Large Hadron Collider (LHC) is the largest and most powerful particle accelerator ever built. It is located at the European Organisation for Nuclear Research (CERN) in Geneva at about 100 m underground in the 27 km long tunnel that previously hosted the Large Electron-Positron collider (LEP).

The LHC is the final stage of a series of particle accelerators (for protons and Pb nuclei, in particular) whose layout is reported in Fig. 2.1: the first stage is the Linac2, which accelerates the particles to 50 MeV; particles are then injected into the PS Booster, where they reach 1.4 GeV; the next step is the Proton Synchrotron (PS) where they accelerate to 25 GeV; particles are then sent to the Super Proton Synchrotron (SPS), which accelerates them to 450 GeV; finally they reach the LHC where they are accelerated to the required energy.

Inside the accelerators, the beams circulate in opposite directions into two beampipes, guided by a strong magnetic field generated by super-conducting magnets. The performances of the accelerator are defined by the centre-of-mass energy of the colliding beams, \sqrt{s} , which represents the available energy to produce new particles, and by the instantaneous luminosity, \mathcal{L} , which is the ratio of the number of events detected in a certain time to the interaction cross-section, σ . The LHC has been designed to reach $\sqrt{s} = 14$ TeV and $\mathcal{L} = 10^{34} \text{ cm}^{-2} \text{ s}^{-1}$.

Particles collide at four locations along the ring of the LHC, which correspond to the position of the four main LHC experiments [20]: A Large

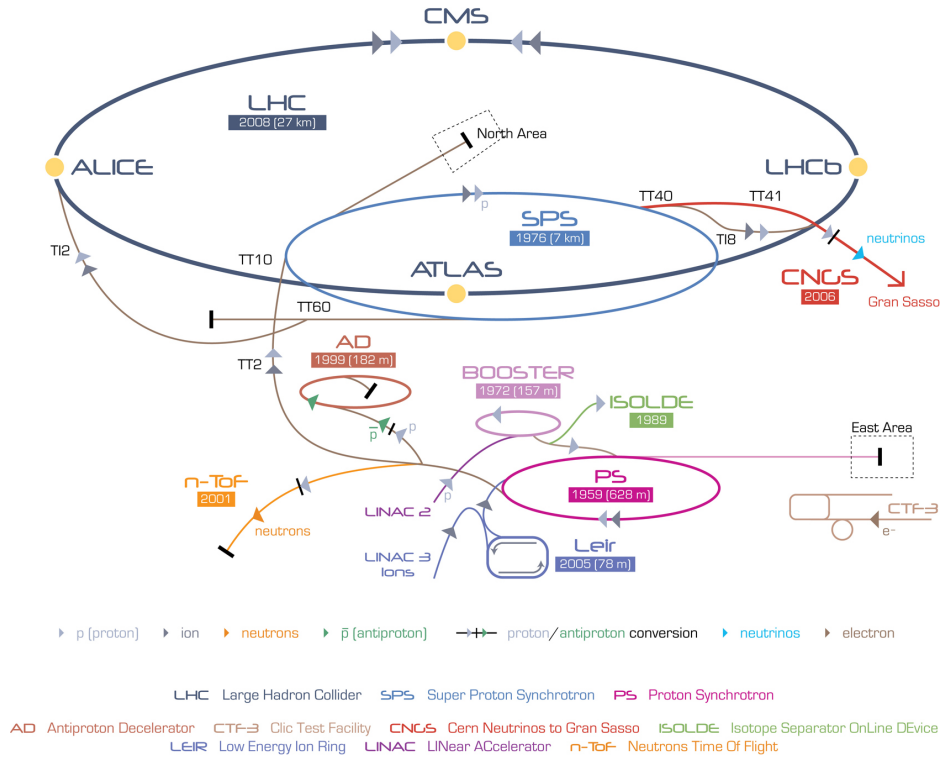


Figure 2.1: Overview of the Cern Accelerator Complex [21].

Ion Collider Experiment (ALICE), A Toroidal LHC ApparatuS (ATLAS), Compact Muon Solenoid (CMS), and Large Hadron Collider beauty experiment (LHCb). The ALICE experiment is focused on the study of Quark Gluon Plasma (QGP) through QCD studies in heavy ion collisions. ATLAS and CMS are general purpose experiments, which study the full spectrum of high-energy physics. LHCb is dedicated to the study of b - and c -hadron decays and will be described in detail in the following Section.

2.2 The LHCb experiment

The LHCb detector [22] has been built in the cavern of the former DELPHI detector at LEP. It has been designed as a high precision experiment devoted to the search of physics beyond the Standard Model through the study of CP violation and rare decays in hadrons containing b and c quarks.

LHCb is a single-arm forward spectrometer covering the pseudorapidity

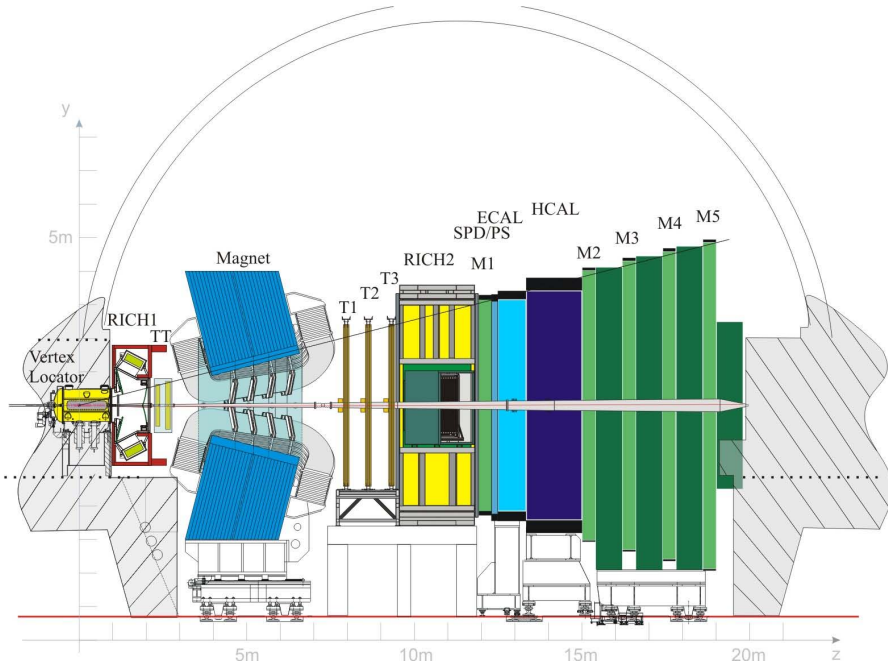


Figure 2.2: Two-dimensional view of the LHCb experiment. The right-handed coordinate system is used that has the z axis along the beam direction, the y axis vertically upwards and the x axis pointing towards the center of the LHC ring.

range $2 < \eta < 5$. This choice for the geometry, which is reported in Fig. 2.2, has been driven by the fact that, at high energy, hadrons from $b\bar{b}$ pairs from p - p collisions are mainly produced in the same forward or backward cone at the typical LHC collision energies ($\sqrt{s} > 1$ TeV).

Data quality is affected by the pile-up caused by high peaks in luminosity. In order to bring the pile-up under control, LHCb operates at lower (with respect to the other LHC experiments) and leveled luminosity. This operational mode allowed to collect data corresponding to an integrated luminosity of $\sim 1 \text{ fb}^{-1}$, $\sim 2 \text{ fb}^{-1}$, and $\sim 320 \text{ pb}^{-1}$ in 2011, 2012, and 2015, respectively.

Excellent resolution, both in momentum and time, are required for an effective separation of the decays of interest from the background. LHCb detectors provide a precise measurement of momentum p , with a relative uncertainty which varies from 0.5% at low momentum p to 1% at 200 GeV/ c . This translates into a precise determination of the invariant mass, whose res-

olution is $\sim 8 \text{ MeV}/c^2$ for $B \rightarrow J/\psi X$ decays, $\sim 22 \text{ MeV}/c^2$ for two-body B decays and $\sim 100 \text{ MeV}/c^2$ for $B_s \rightarrow \phi \gamma$. The impact parameter (IP) is measured with a resolution of $20 \mu\text{m}$ for particles having high transverse momentum p_T . Good decay time resolution is important to resolve B_s^0 flavour oscillations and is measured to be 45 fs for $B_s \rightarrow J/\psi \phi$ and $B_s \rightarrow D_s \pi$. In addition to this, charged particle identification is essential in any flavour physics programme in order to isolate suppressed decays: LHCb detectors guarantee high efficiency ensuring at the same time low particle misidentification: $\varepsilon_e \sim 90\%$ for $5\% \text{ P}(h \rightarrow e)$, $\varepsilon_K \sim 95\%$ for $5\% \text{ P}(\pi \rightarrow K)$, $\varepsilon_\mu \sim 97\%$ for $1\text{--}3\% \text{ P}(\pi \rightarrow \mu)$.

2.3 Tracking System

As already pointed out in Sec. 2.2, the LHCb tracking system includes a vertex locator system (VELO) and four planar stations: the Tracker Turicensis (TT) and the T stations (T1, T2, and T3). They use silicon microstrip detectors, with the exception of the outermost regions of the T stations, the Outer Tracker (OT), where straw-tubes technology is employed.

2.3.1 VERtEX LOcator

The LHCb experiment must guarantee a precise vertex reconstruction, since a displaced secondary vertex is a distinctive feature of the decays LHCb is optimised for; as an example, the average distance between the production vertex and the vertex of a B hadron decay is of approximately 12 mm .

The VERtEX LOcator (VELO) [23] design, represented in Fig. 2.3, has been optimised to provide a precise measurement of the track coordinates close to the interaction region, and of the position of the primary and secondary vertices. It consists of two series of planar half-circular silicon detector modules arranged along the beam direction as in Fig. 2.4 placed at a radial distance of 8 mm from the beam when the detector is in its *closed* configuration. This distance is smaller than the aperture required by the LHC during beam injection and the two halves must therefore be retracted during injection and ramping (*open* configuration). The positioning system has an accuracy of $10 \mu\text{m}$. The detector is contained in a vacuum vessel, which is maintained at the same vacuum level as the LHC beampipe (primary vacuum, 10^{-8} mbar) while the sensors are held inside two boxes under a lower vacuum (secondary vacuum, 10^{-4} mbar). The internal walls of the boxes are

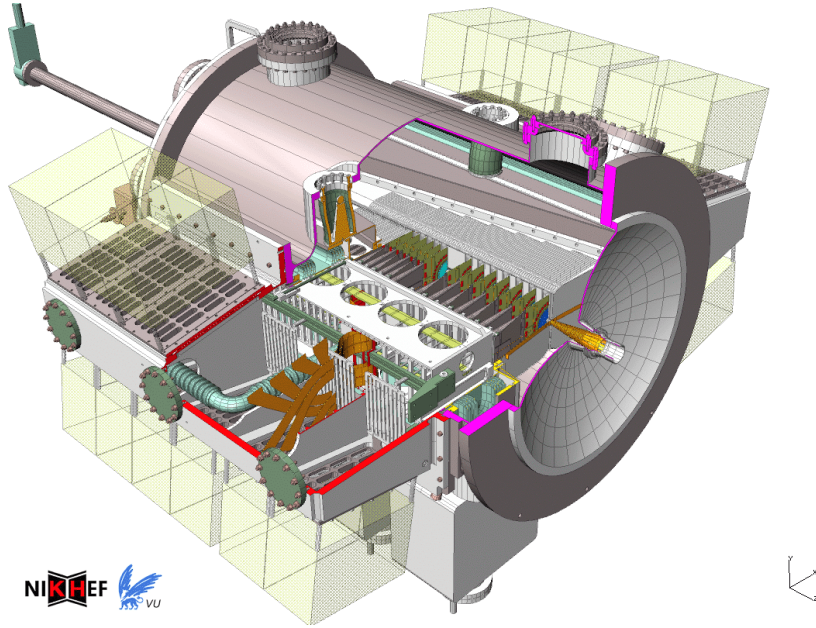


Figure 2.3: Full layout of the VELO.

called RF foils and are designed to suppress weak fields generated by beam bunches passing through the VELO, thus affecting the VELO system due to Radio-Frequency pick-up, and to minimise the material budget (9% of a radiation length) seen by particles from the interaction region.

The optimal angular coverage is reached with pairs of R - and ϕ -segmented sensors (thus providing a radial and an azimuthal measurement, respectively), each with an azimuthal coverage of $\approx 182^\circ$ in order to give a small overlap between the two halves, simplifying the relative alignment. The third coordinate, along the beam axis, is determined from the knowledge of the modules position.

As can be seen in Fig. 2.5, the ϕ -sensors are divided into an inner and an outer part in order to lower the occupancy; the area of the two parts has been chosen in order to equalise the occupancy; for the same reason, the concentric strips of the R -sensors are divided into four segments 45° -wide. The pitch varies from $39.3 \mu\text{m}$ to $78.3 \mu\text{m}$ ($97 \mu\text{m}$) for the inner (outer) part of the ϕ -sensors and from $40 \mu\text{m}$ to $101.6 \mu\text{m}$ for the R -sensors. The strip resolution strongly depends on the pitch, and the best resolution has been measured to be $7 \mu\text{m}$. Its high spatial resolution enables a precise determination of the particles' flight direction close to the primary interaction, resulting in

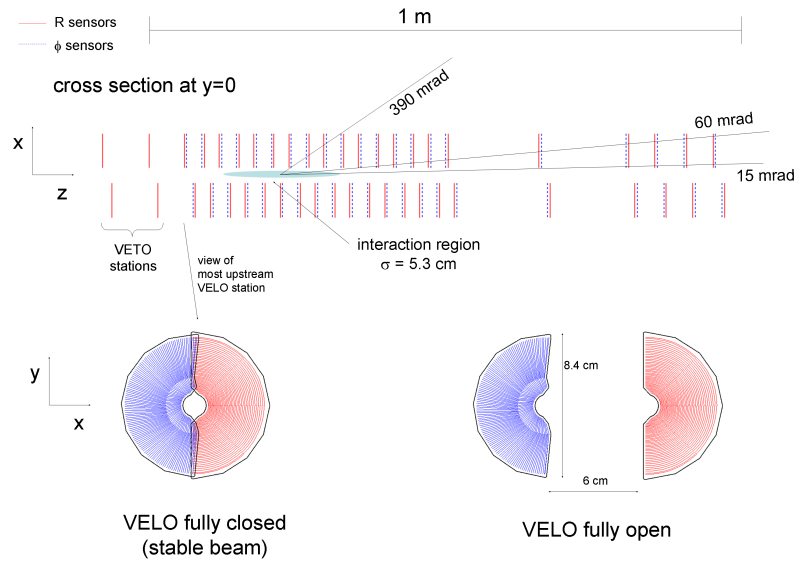


Figure 2.4: Arrangement of the VELO modules along the beam direction (top) and layout of the sensors for the *closed* and *open* configurations (bottom).

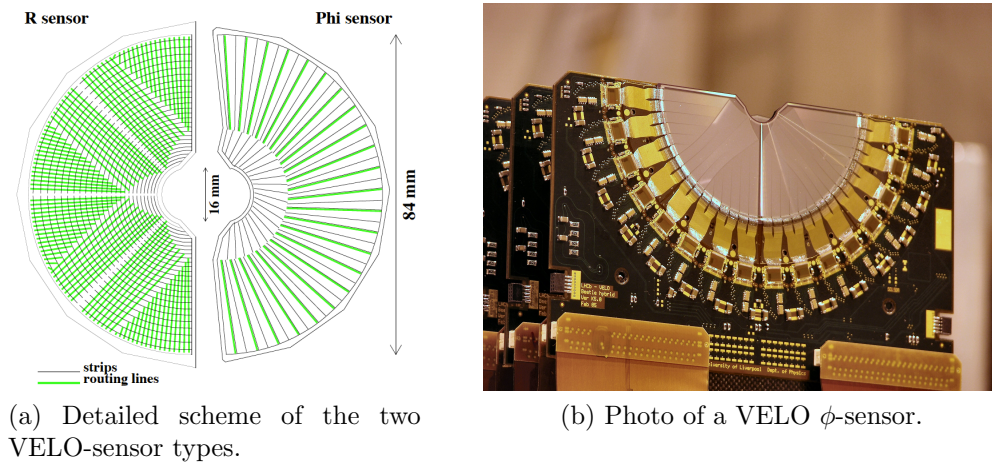


Figure 2.5: The VELO R - and ϕ sensors.

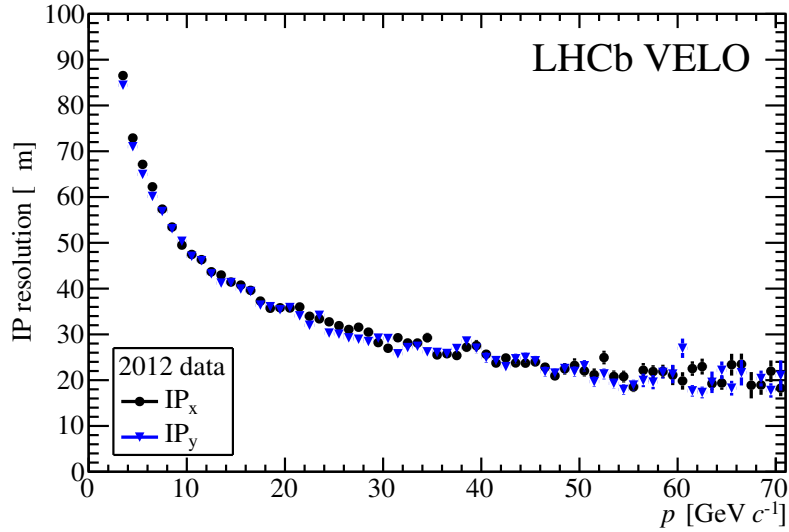


Figure 2.6: IP_x (dark blue circles) and IP_y (blue triangles) resolution as a function of momentum determined with data collected in 2012 [24].

an excellent impact parameter resolution which reaches $\sigma_{IP} \sim 20 \mu\text{m}$ for high-momentum tracks, as can be seen in Fig. 2.6.

The sensors operate in a harsh radiation environment, with the highest radiation level in the innermost region; for this reason a two-phase CO_2 cooling system maintains the temperature of the detector modules below -5°C .

2.3.2 Dipole Magnet

In order to determine the charge and measure the momentum of charged particles, the LHCb experiment uses a dipole magnet whose magnetic field orientation is such that the Lorentz force experienced by charged particles bends their trajectories in the horizontal (xz) plane (see Fig. 2.2 for axes orientation). The magnet is placed between the TT and T1, and its scheme is depicted in Fig. 2.7. Its design had to accommodate the contrasting requests for a residual field inside the RICHs less than 2 mT and a bending power as high as possible between the VELO and the TT. The magnet consists of two identical and symmetrical coils, composed of fifteen pancakes of pure Al-99.7 each with a central cooling. A field mapping has been performed to measure the three components of the magnetic field inside the tracking

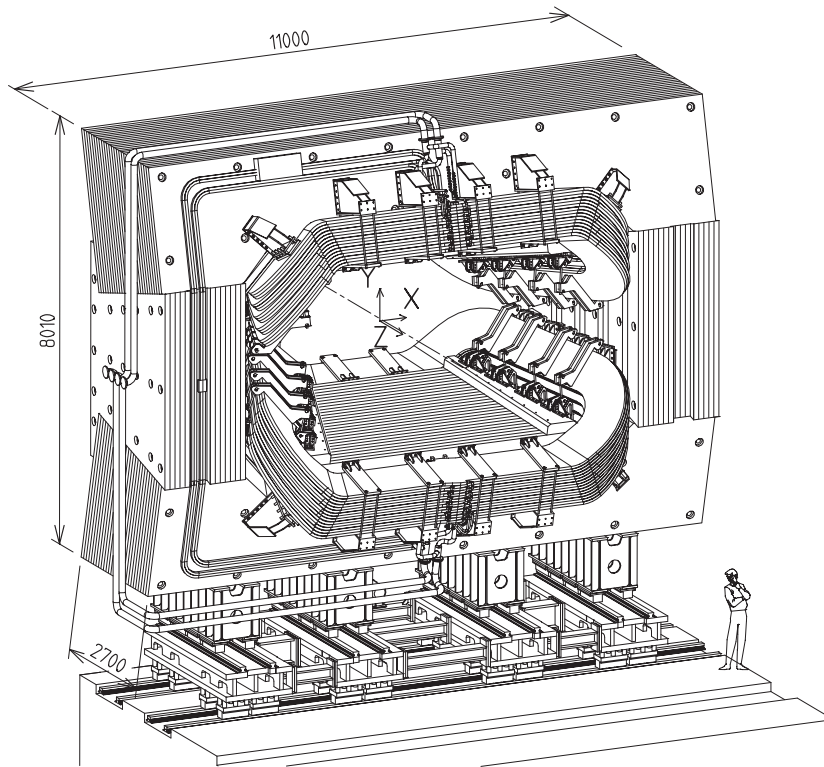


Figure 2.7: Perspective view of the LHCb dipole magnet. The interaction region lies behind the magnet.

volume (which is $3.6 \text{ T}\cdot\text{m}$) with a precision of about $4 \cdot 10^{-4}$. In Fig. 2.8 the main component of the field, B_y , is shown together with the result of the model calculation. In order to perform physics systematics checks, the magnet polarity is periodically switched during data taking. Using data collected in both configuration allows to reduce the effects due to residual asymmetries in the geometrical acceptance.

2.3.3 Tracker Turicensis

The Tracker Turicensis (TT) [25] is located downstream of the VELO and upstream of the magnet. The position is crucial for the fulfillment of its purpose of (offline) reconstruction of the trajectories of long-lived neutral particles decaying outside the acceptance of the VELO, such as the K_S^0 and of low-momentum particles, which are bent outside the acceptance of the experiment before reaching T1. The TT consists of four detection layers

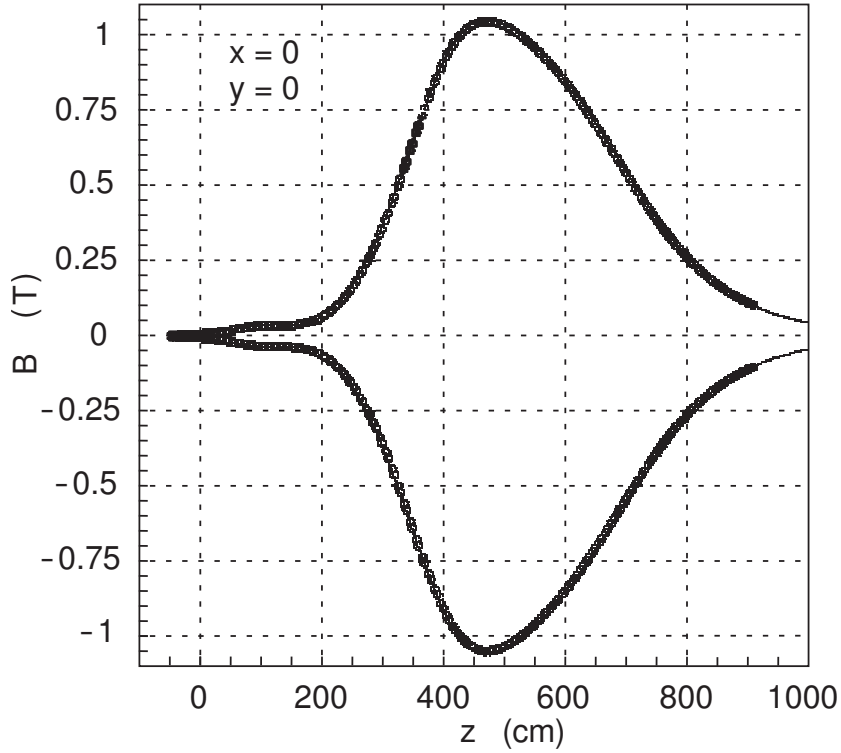


Figure 2.8: y component of the magnetic field as measured along the z axis for both polarities.

rotated by a stereo angle of $0^\circ/+5^\circ/-5^\circ/0^\circ$ arranged in two pairs to aid the track reconstruction algorithms. The active area of the tracker covers the nominal acceptance of LHCb (300 mrad in the horizontal plane, 250 mrad in the vertical plane). The layout of the third layer is shown in Fig. 2.9. The basic unit is the half module, which includes seven silicon sensors organised in sectors of different readout. Their readout hybrids are mounted at one end of the half module. The main advantage of this design is that all the cooling and front-end readout are outside the acceptance of the experiment. The silicon sensors are $500 \mu\text{m}$ thick and each of them is composed of 512 silicon strips with a pitch of $183 \mu\text{m}$; the resulting single-hit resolution is of about $50 \mu\text{m}$. The four layers are housed in a light-tight thermally and electrically insulated module, which is maintained constantly at a temperature below -5°C , and which has a nitrogen flushing system to avoid condensation.

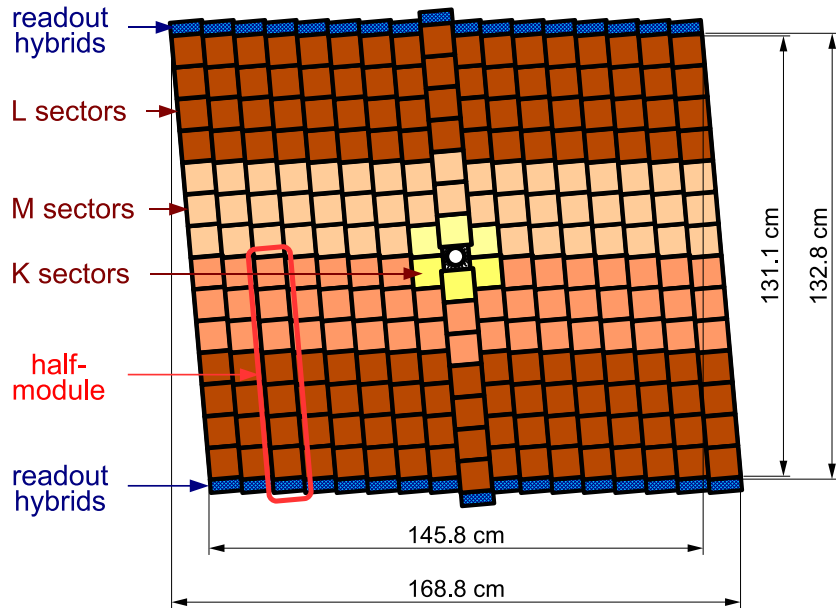


Figure 2.9: Layout of the third TT detection layer. Each colour represent a different readout sector.

2.3.4 Inner Tracker

The Inner Tracker (IT) occupies the innermost region of the T1, T2, and T3 stations as can be seen in Fig. 2.10. This part of the T-stations is the one experiencing the highest particle fluxes ($\sim 5 \cdot 10^{-5} \text{ cm}^{-2} \text{ s}^{-1}$), thus the same detector technology as in TT is used: both detectors use silicon microstrip sensors with a pitch of about $200 \mu\text{m}$, which allows to reach a single-hit resolution of about $50 \mu\text{m}$. The same cooling strategy is also used. Each IT consists of four detection boxes arranged around the beampipe as illustrated in Fig. 2.11. Contrary to the TT, where most of the passive elements is located outside acceptance, the material distribution in the IT is less uniform due to readout hybrids, mechanical supports, cables and cooling located inside acceptance; the material budget varies from $0.015 X_0$ per station for the active area to a peak of $0.30 X_0$ in the narrow region of the cooling rods.

2.3.5 Outer Tracker

The Outer Tracker (OT), shown in Fig. 2.10, covers the remaining area of the T1-T2-T3 stations. Its structure has been optimised for a precise de-

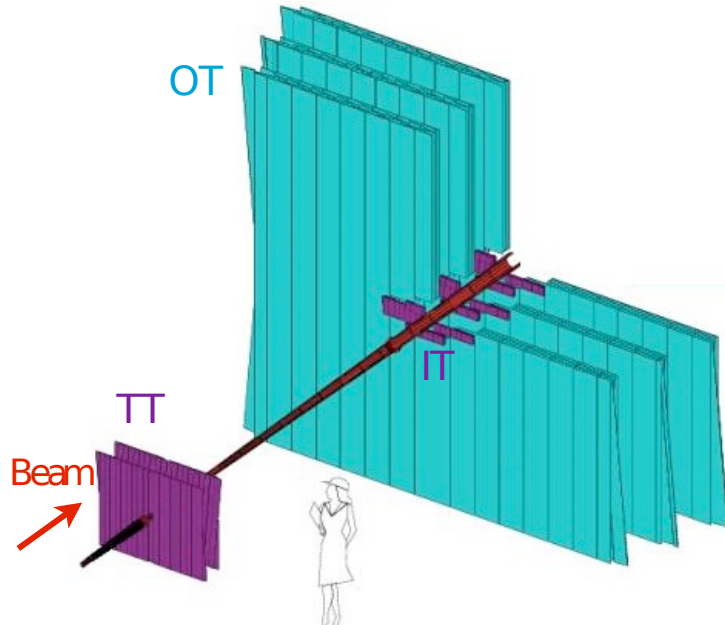
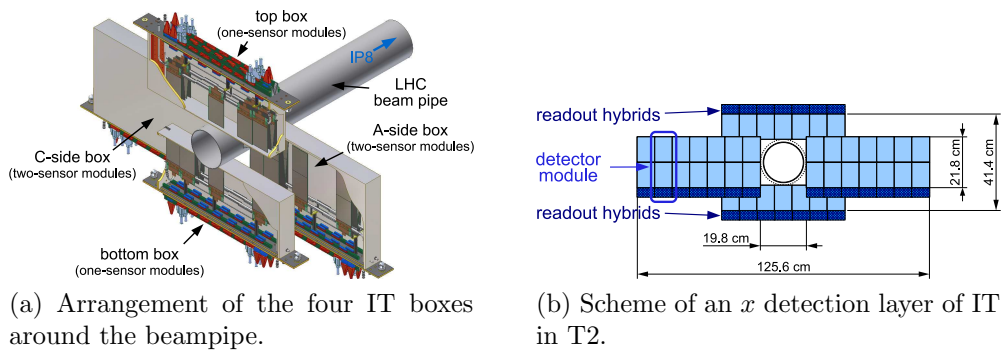


Figure 2.10: Arrangement of the Tracker Turicensis (TT), and the two parts of the T-stations: the Inner Tracker (IT) and the Outer Tracker (OT).



(a) Arrangement of the four IT boxes around the beampipe.

(b) Scheme of an x detection layer of IT in T2.

Figure 2.11: Views of the IT sub-detector.

termination of the reconstructed b -hadrons and so an excellent momentum resolution is needed: a mass resolution of $10 \text{ MeV}/c^2$ translates into a required resolution on the momentum of $\delta p/p \approx 0.4\%$.

The OT is a gas drift detector designed as an array of straw-tube modules, which uses a mixture of Ar (70%) and CO_2 (30%) thus ensuring a fast drift time ($<50 \text{ ns}$, approximately two bunch crossings) and an adequate spatial resolution ($200 \mu\text{m}$). The straw tubes are arranged in three station of four layers each, rotated by $0^\circ/+5^\circ/-5^\circ/0^\circ$ with respect to the vertical axis. This orientation ensures better reconstruction performances in the bending plane. The detection modules are split into two independently movable halves (C-frames) and supported by aluminium structures hosting all detector services, sustained by a stainless steel structure (OT bridge) equipped with rails. Thanks to the chosen arrangement, all the detector services and supports are placed outside the LHCb acceptance, hence the material budget is mainly due to the active part of the detector only (3.2 % of X_0 per station).

2.3.6 Track reconstruction

The track reconstruction software combines the hits from the VELO, the TT, the IT, and the OT subdetectors to form all the particle trajectories. Tracks are divided into five categories, as illustrated in Fig. 2.12:

- **long tracks** traversing the full tracking system, from the VELO to the T stations. They ensure a precise determination of the particle momentum, thus being the most important set of tracks for b -hadron decay reconstruction;
- **upstream tracks** traversing the VELO and the TT. This kind of track is peculiar of low momentum particles, which are bent outside the detector acceptance by the magnetic field. However, they also pass through RICH1 where they may generate Cherenkov photons, thus allowing to understand backgrounds in the RICH particle identification algorithm;
- **downstream tracks**, which are only visible in the TT and in the T stations. Usually attributable to decay products of the decay of long lived particle that decay outside the VELO acceptance;
- **VELO tracks** only visible in the VELO and useful for primary vertex reconstruction. A momentum estimation is not possible since the B

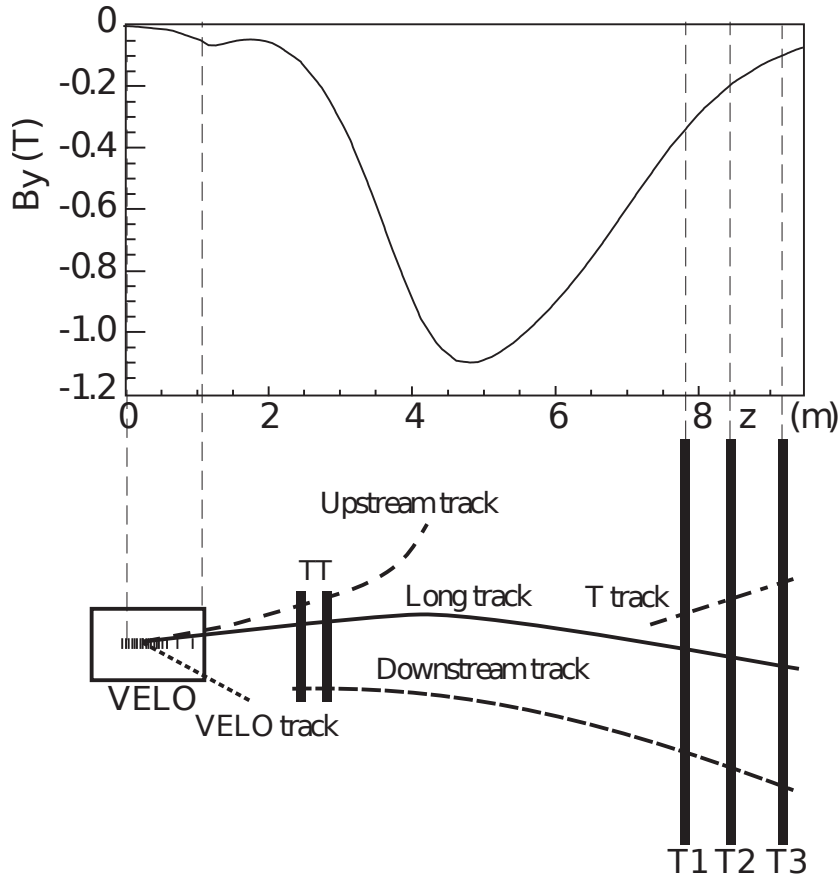


Figure 2.12: Classification of the various track types that can be reconstructed in the LHCb tracking system. The main B-field component (B_y) is reported above as a reference.

field is very weak inside the VELO and these tracks can be described as straight lines;

- **T tracks** are only visible in the T stations. They are typically produced in secondary interactions.

The track reconstruction starts from the search of track segments in the VELO and in the T stations, where the magnetic field is low. These segments act as the *seed* of the full track reconstruction. Once all candidate tracks have been found by matching the seeds with other tracking hits, the trajectories are refitted with a Kalman filter [26] which accounts for multiple scattering

and magnetic field, and corrects for dE/dx losses. The χ^2 variable of the fit is used to monitor the quality of the reconstructed track.

2.4 RICH system

Hadronic multibody final states that are typical of b - and c -hadrons decay modes often have very similar topology but different flavour content. In this case the invariant mass is not always sufficient to discriminate between different final states, and the information provided by the RICH system, whose primary role is the identification of charged hadrons (π , K , p), becomes fundamental. In addition to this, RICH subdetectors also give a contribution to the identification of charged leptons (e and μ), which complements the information from the calorimeters and the muon system, respectively. The necessity for two RICH detectors arises from the fact that at large polar angles the momentum spectrum is softer while at small polar angles it is harder: the upstream detector, RICH1, covers the low momentum range (from ~ 1 GeV/c up to 60 GeV/c) thanks to an aerogel and a fluorobutane (C_4F_{10}) radiators, while the downstream detector, RICH2, is optimised to cover the high momentum range (from ~ 15 GeV/c up to and beyond 100 GeV/c) using a tetrafluoromethane (CF_4) radiator (see Fig. 2.13). While RICH1 covers the full angular acceptance (from ± 25 mrad to ± 300 mrad in the horizontal plane and ± 250 mrad in the vertical plane), RICH2 has a limited geometrical acceptance (from $\sim \pm 15$ mrad to ± 120 mrad in the horizontal plane and ± 100 mrad in the vertical plane). Both subdetectors use a combination of flat and spherical mirrors to focus the Cherenkov light and reflect the image out of the spectrometer acceptance. Hybrid Photon Detectors (HPDs) are used to detect the Cherenkov photons in the wavelength range 200–600 nm. The HPDs are divided in pixels in order to measure the position of the incoming photon.

2.4.1 RICH1

The RICH1 is located upstream of the magnet, between the VELO and the TT subdetectors. A scheme of the RICH1 subdetector is shown in Fig. 2.14(a). Its design has been optimised to satisfy the following criteria:

- minimisation of the material budget within the particle acceptance: to satisfy this requirement, lightweight spherical mirrors have been

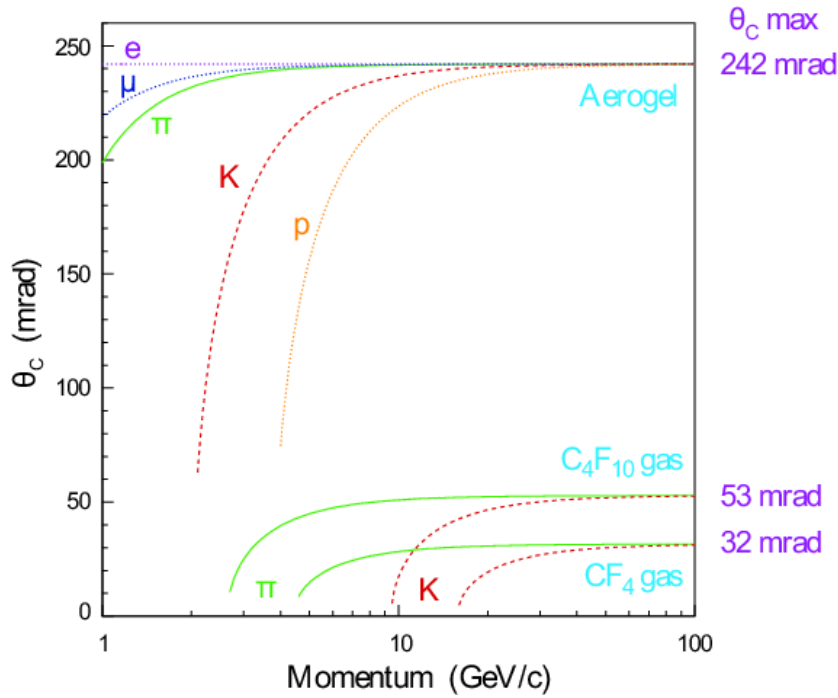


Figure 2.13: Cherenkov angle, defined as $\theta_C = \frac{1}{n\beta}$, as a function of momentum for the three different RICH radiators.

chosen, and all the other components are placed outside acceptance; this lead to a total radiation lenght of $\sim 8\%$ X_0 ;

- the necessity for hosting the beryllium beampipe;
- shielding of the HPDs from the field generated by the LHCb dipole magnet; they are surrounded by large iron shield boxes and placed in MuMetal cylinders in order to correctly operate in magnetic fields up to 50 mT.

As previously said, the RICH1 uses two different radiators: an aerogel and a gas. The aerogel covers the range of refractive indices between gas and liquid. Despite being a solid it has an extremely low density and a refractive index tuneable in the range 1.01–1.10, thus being ideal for the identification of particles with momentum of a few GeV/c. In LHCb the aerogel radiator was mainly used for the identification of protons; nevertheless, it has been proven to be not effective and for this reason it has been removed during

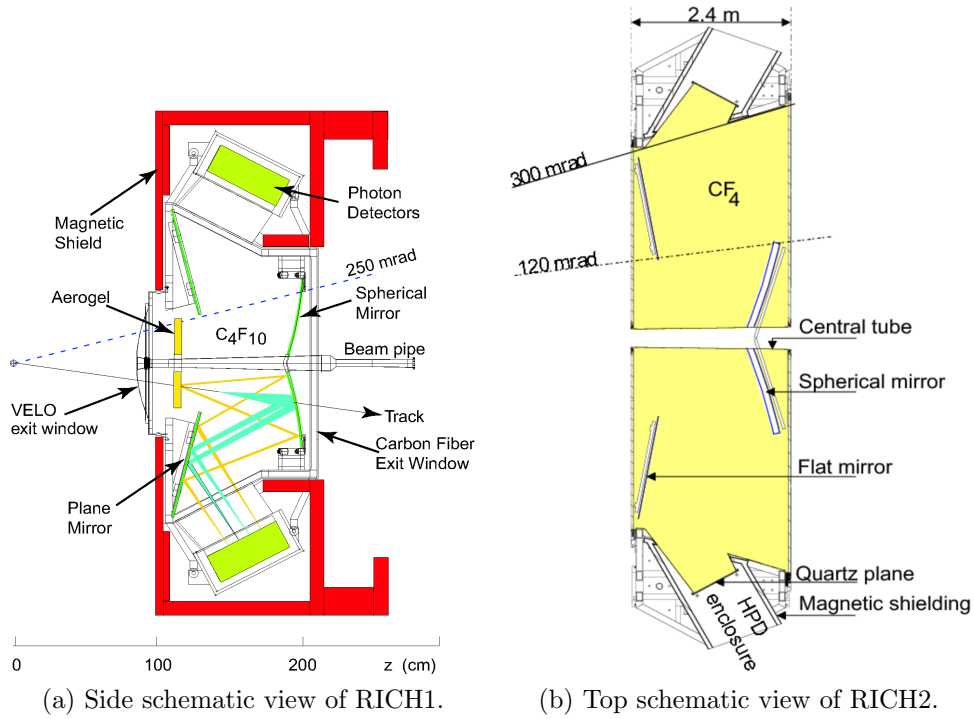


Figure 2.14: Layout of the two Ring Imaging Cherenkov detectors at LHCb.

the Long Shutdown 1, with the positive consequence of increasing the gas volume thus intensifying the photon production.

2.4.2 RICH2

The RICH2 is located between T3 and the first muon station, M1. Its structure is shown in Fig. 2.14(b), which clarifies how unlike RICH1, RICH2 is developed horizontally, with the HPDs on the left and on the right of the beamline. The overall design had to comply with the same constraints as for RICH1. In this case the total radiation length including the gas radiator is $\sim 0.15 X_0$.

2.4.3 RICH PID performances

The projection of the Cherenkov photons on the photon detectors is affected by the imperfection of the imaging system. This causes the images formed

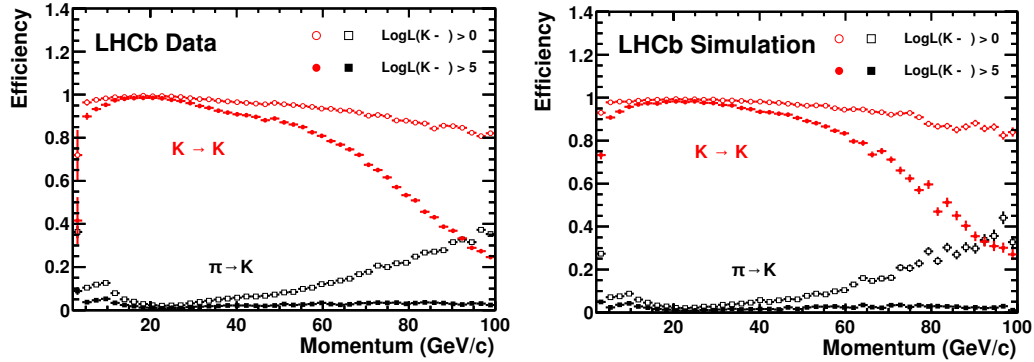


Figure 2.15: Kaon identification efficiency and pion misidentification fraction in data (left) and simulation (right) as a function of momentum. Two different PID requirements have been imposed on the sample, resulting in open and filled marker distribution.

on the photon detector planes to be distorted. For this reason two alternative pattern recognition techniques are preferred to the simple fitting of the circles: the “local” and the “global” method. The first approach treats each track independently to determine a value for the Cherenkov angle, defined as $\theta_C = 1/n\beta$, for every hit in the photon detector plane, and a likelihood is calculated for each mass hypothesis. This approach is only valid for low multiplicity of tracks, because the overlapping of rings due to different particles can form a background. In this cases the global approach is preferred, which implements a simultaneous fit to all track hypotheses, taking into account the information from both RICH1 and RICH2. The discriminating variable for the particle identification is the so called $\Delta \log \mathcal{L}$: the likelihood for a certain mass hypothesis is taken as the difference of the likelihood logarithm under a generic hypothesis and the pion mass hypothesis, which is taken as a reference; in this way the $\Delta \log \mathcal{L}$ for pion hypothesis is always zero:

$$\Delta \log \mathcal{L}(X - \pi) = \log \mathcal{L}(X) - \log \mathcal{L}(\pi) \equiv DLL(X - \pi) \quad (2.1)$$

where $X = e, \mu, K, p, \pi$.

The RICH particle identification performance on data has been studied in the control samples $K_s^0 \rightarrow \pi^+\pi^-$, $\Lambda \rightarrow p\pi^-$, and $D^{*+} \rightarrow D^0(K^-\pi^+)\pi^+$, which provide background-free samples of π , K and p .

The performances for kaon efficiency (kaons identified as kaons) and pion misidentification fraction (pions misidentified as kaons) is shown in Fig. 2.15

as a function of momentum for data and simulation. Results are shown with two different cuts on PID, one optimising the efficiency and the other maximising the pion rejection fraction: in the first case, a likelihood for the kaon hypothesis larger than that for the pion hypothesis is required, i.e. $\Delta \log \mathcal{L}(K - \pi) > 0$, and this results in a kaon efficiency of $\approx 95\%$ with a pion misidentification fraction of $\approx 10\%$; in the second case a stricter requirement is used on PID, $\Delta \log \mathcal{L}(K - \pi) > 5$, and this reduces the pion misidentification fraction to $\approx 3\%$ with a modest reduction in kaon efficiency to $\approx 90\%$. These values are averaged over the momentum range 2–100 GeV/c. For all the distributions, a good agreement data–simulation is clear.

2.5 Calorimeters

The calorimeter system, which is located between the first two muon stations, has been optimised for energy measurement and for the identification of neutral hadrons, electrons and photons by selecting high transverse energy (E_T) particles. The accurate reconstruction of π^0 and prompt photons is essential for the study of B-meson decays and for flavour tagging in general, therefore the calorimeter system has a fundamental role for the LHCb physics programme.

The sub-detectors constituting the calorimeter system are:

- the Scintillator Pad Detector (SPD);
- the Pre-Shower (PS);
- the Electromagnetic CALorimeter (ECAL);
- the Hadronic CALorimeter (HCAL);

and their design follow a classical scheme: the ECAL detects electrons and photons and is followed by the HCAL for charged and neutral hadrons; in order to select electrons from the charged pion background, the PS has been built before the ECAL; in addition to this, in order to reject the background of electrons from high- E_T π^0 s the SPD has been installed before the PS. The calorimeter system is segmented into tiles in the xy plane, with a variable lateral segmentation to cope with the hit density, which varies by two orders of magnitude over the detector area. In particular, three different granularities have been chosen for the ECAL and projectively for SPD and PS, while HCAL is segmented into two zones with larger cell sizes. The segmentation

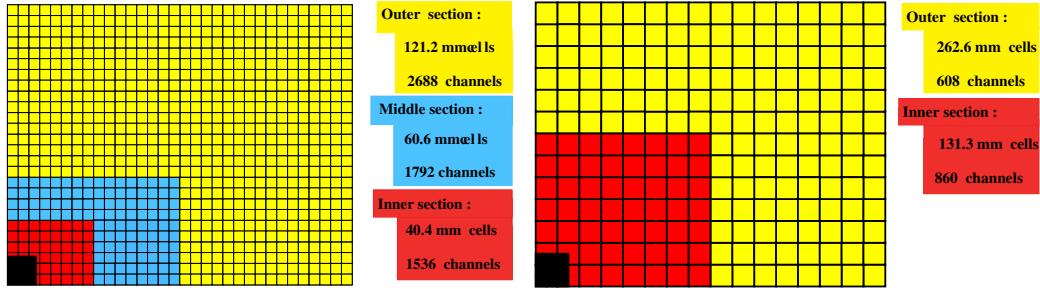


Figure 2.16: Lateral segmentation of the SPD, PS and ECAL (left), where the cell dimensions are relative to the ECAL, and of the HCAL (right). One quarter of the detector is shown.

scheme is shown in Fig. 2.16. All calorimeters have the same working principles: scintillation light is collected by wavelength-shifting (WLS) fibers and transmitted to a photomultiplier tube (PMT). The single fibres of the SPD and PS cells are read out by multianode photomultiplier tubes (MAPMT), while the fibre bunches in HCAL and ECAL require individual phototubes.

2.5.1 Pre-Shower and Scintillator Pad Detector

The Pre-Shower (PS) and Scintillator Pad Detector (SPD) consist of two planes of rectangular scintillator pads separated by a 15 mm thick lead converter ($\sim 2.5 X_0$). The two detector planes are not identical: due to the projectivity requirements, the SPD is smaller than the PS by $\sim 0.45\%$. The two sub-detectors are divided vertically into two halves that can slide independently on horizontal rails in order to allow service and maintenance work. An ionizing particle crossing the scintillator produces light, which is guided by the WLS fibre to clear fibres and finally a MAPMT pixel. The long clear fibres allowed the positioning of the photomultiplier tubes outside the detector acceptance.

The information from SPD (PS) is combined with data from ECAL to reject $\pi^0 \rightarrow \gamma\gamma$ ($\gamma(\pi^\pm)$) background from the e^- candidate selection. The e/π separation performances had been measured at the CERN SPS with electrons and pions beams of momenta in the range 10–50 GeV/c. Pion rejection of 99.6%, 99.6%, and 99.7% were achieved with electron retentions of 91% , 92% , and 97% for 10, 20, and 50 GeV/c beams, respectively. The γ/e separation at the trigger level is achieved using the SPD information. In principle, charged particles deposit energy in the scintillator material while

neutral particles do not interact; nevertheless, other processes can lead to energy deposit in the scintillator resulting in a background. The dominant process is the photon conversion in the detector material before the SPD. Two other sources have been investigated with a photon beam and beams of e and π of different energies:

- photon interactions in the SPD that produce charged particles inside the SPD;
- *back splashes*, *i.e.* interactions due to backward moving particles generated in the lead absorber or in the ECAL.

The misidentification probability is of about 0.9% and 1.4%, respectively. These results are in very good agreement with Monte Carlo simulation studies.

2.5.2 Electromagnetic CALorimeter

For the Electromagnetic CALorimeter (ECAL) the “shashlik” technology has been chosen, in which sampling scintillator and lead absorbers alternate, and they are read out by plastic WLS fibres. This technology ensures modest energy resolution, fast time response, acceptable radiation resistance and robustness. The design energy resolution is

$$\frac{\sigma_E}{E} = \frac{10\%}{\sqrt{E}} \oplus 1\% \quad (E \text{ in GeV}), \quad (2.2)$$

which results in a B mass resolution of 65–75 MeV/ c^2 depending on the considered decay channel. The hit density varies over the active volume by two orders of magnitude, thus the calorimeter is divided into three sections of increasing granularity approaching the beampipe. Each module is 42 cm thick, which corresponds to a total thickness of 25 X_0 and a corresponding Molière radius of 3.5 cm to fully contain high energy photons showers.

2.5.3 Hadronic CALorimeter

The sampling Hadronic CALorimeter (HCAL) structure consists of alternating absorber layers of iron and scintillator, oriented with the scintillating tiles that run parallel to the beam axis and hence to the particles flow. The longitudinal length of tiles and iron spacers correspond to the hadron λ_I in steel, and the detector thickness corresponds to 5.6 λ_I . The light is collected

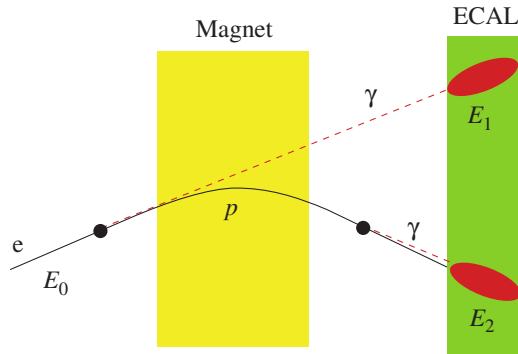


Figure 2.17: Illustration of Bremsstrahlung correction used for electron identification.

by WLS fibres running along the detector towards the back side where PMTs are housed. The energy resolution can be approximated by

$$\frac{\sigma_E}{E} = \frac{80\%}{\sqrt{E}} \oplus 10\% \quad (E \text{ in GeV}). \quad (2.3)$$

2.5.4 Calorimeters PID performances

The electron identification is based on ECAL information about track momentum and energy of charged clusters, and matching between the corrected barycenter position of the cluster with the extrapolated track impact point. The identification takes advantage of Bremsstrahlung photons emitted by electrons before the magnet, as depicted in Fig. 2.17: if an electron radiates photons in the material before the magnet, a separate cluster with energy E_1 is seen in the ECAL; if it radiates after the magnet, the Bremsstrahlung photon will not lead to a separate cluster. For electron identification the corresponding cluster energy E_2 will be compared to the track momentum ($E_2 = p$), while the energy of the electron at the origin is $E_0 = E_1 + E_2$. Further improvement is obtained by using the track energy deposit in the PS and in the HCAL. The average efficiency to identify electrons from $J/\psi \rightarrow e^+e^-$ decays in $B^0 \rightarrow J/\psi K_S^0$ events in the calorimeter acceptance is of about 95%, with a pion misidentification fraction of 0.7%.

The information from ECAL is also used for photon reconstruction and identification. They are identified as clusters without an associated track.

Due to ECAL granularity, in a channel like $B^0 \rightarrow \pi^+\pi^-\pi^0$, for a transverse momentum of the π^0 about 3 GeV/c, the reconstruction of the π^0

decay is a resolved pair of well separated photons, while for higher transverse momentum the photon pairs cannot be resolved as a pair of clusters. About 30% of the π^0 from $B^0 \rightarrow \pi^+\pi^-\pi^0$ lead to a single cluster that can be ascribed to a merged π^0 .

2.6 Muon System

Many final states of B-decays that are sensitive to CP violation contain muons. In particular, two muons are present in the final state of the two *gold-plated* decays

$$B_d^0 \rightarrow J/\psi(\mu^+\mu^-)K_s^0 \text{ and } B_s^0 \rightarrow J/\psi(\mu^+\mu^-)\phi,$$

which play a major role in CP asymmetry and oscillation measurements. Muons are also foreseen in rare B decays, such as the FCNC $B_s^0 \rightarrow \mu^+\mu^-$, which may reveal possible effects due to physics beyond the SM [27]. For these reasons, efficient muons triggering and identification are crucial requirements for the LHCb experiment.

2.6.1 Overview

The main requirement for the muon sub-detector is to provide a high- p_T muon trigger and must correctly identify the bunch crossing the muons belong to, with a time resolution better than 25 ns. It also has to provide offline muon identification with an efficiency above 90% while maintaining the pion misidentification probability below 1.5%, since an efficient and with low contamination muon identification is fundamental for both tagging and clean reconstruction of B decays with muons in the final state. The Muon System [28, 29, 30], whose scheme is shown in Fig. 2.18, consists of five rectangular stations (M1–M5) of scaling transverse dimensions, which guarantees an inner and outer acceptance of 20 (16) mrad and 306 (258) mrad in the bending (non-bending) plane, respectively. This corresponds to an acceptance of $\sim 20\%$ for muons from inclusive b semileptonic decays.

The first station, M1, is placed in front of the calorimeters. For this reason it provides a hits position measurement that is not affected by the multiple scattering caused by the huge material of ECAL and, in particular, of HCAL. Also if it is not used for muon identification purposes, it is fundamental to improve the p_T measurement for the first level trigger. Stations M2 to M5 are placed downstream of the calorimeters and they are interleaved

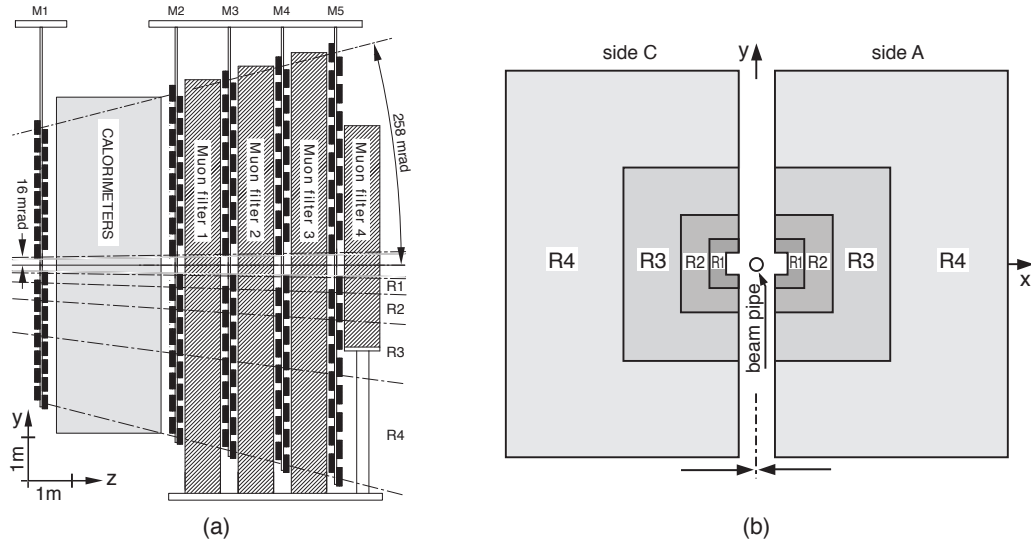


Figure 2.18: Side (left) and front (right) view of the LHCb Muon System.

Station	Position (m)
M1	12.1
M2	15.2
M3	16.4
M4	17.6
M5	18.8

Table 2.1: Mean position of the five muon stations as measured from the interaction point.

with 80 cm thick iron absorbers. The total material budget including the calorimeters is of about $20 \lambda_I$, thus the minimum momentum of a muon to cross all the muon stations is approximately 6 GeV/c. Another iron absorber is placed after M5 in order to attenuate the last muon station from particles emerging from the tunnel. The distance from the interaction point of the muon stations is summarised in Table 2.1. Since the detector modules are arranged into two layers per each station, the reported position is defined as the mean value of the positions of the two layers. Each station is divided into four concentric regions (R1, R2, R3, R4) of segmentation scaling in the ratio 1:2:4:8, optimised to have approximately the same particle flux and

channel occupancy over the four region of a given station.

2.6.2 Detector Technology

The detector technology of choice has been determined taking into account the following parameters:

- **rate capability and ageing:** the detector materials and the front-end electronics must have good ageing properties in order to guarantee ten years of LHCb data-taking without significant performance losses. The particle flux varies of a factor of about $2 \cdot 10^3$ from the inner region of the first station (M1R1) to the outer region of the last one (M5R4), thus different detector performances and technologies are required;
- **time resolution:** the correct bunch crossing must be identified with at least 95% efficiency within a 20 ns window for each of the two layer in a station;
- **spatial resolution:** this parameter is crucial for both the p_T measurement accuracy and the muon detection efficiency, thus it influences the sub-detector granularity. Inclined tracks can fire more than one channel generating a large geometrical cluster. Furthermore, since each muon station consists of two detection layers, inclined tracks traversing the station can hit two non-projective channels. The cluster size depends on the intrinsic detector spatial resolution, on the two layers separation, and on the cross-talk between adjacent channels. The constraints for the spatial resolution are the following: since M1 and M2 are used for the measurement of the transverse momentum, their x resolution is limited by the required precision on p_T ; the limit on the y dimension depends on the required rejection of background triggers which do not point to the interaction region; the probability for a crossing particle to fire more than one channel must be minimised, so the cross talk between adjacent readout channels must be limited. The required cluster size varies between 1.1 and 1.2 for the outer and the inner regions, respectively.

Based on the above considerations, Multi-Wire Proportional Chambers (MWPCs) have been adopted for the Muon System with the exception of the innermost region of the first station (M1R1), which hosts triple Gas Electron Multiplier (GEM) chambers.

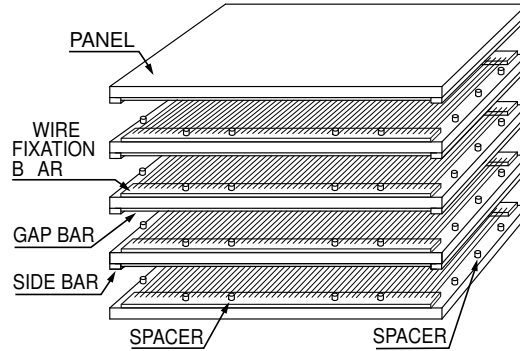


Figure 2.19: Exploded schematic view of a multi-wire chamber.

2.6.2.1 Multi-Wire Proportional Chambers

The MWPCs are composed of four (M2–M5) or two (M1) OR-ed active gas gaps. The scheme for a four gap chamber is shown in Fig. 2.19. The gaps, each having a wire spacing of 2 mm and a gas gap of 5 mm, have been shown to ensure a time resolution of about 4 ns using a non-flammable gas mixture of Ar/CO₂/CF₄ in the ratio 40/55/5. The *double gap* resulting from the OR of the signals of two adjacent gas gaps has an efficiency above 95% in a 20 ns window at a gas gain of $G \simeq 10^5$, achieved at a voltage of 2600–2700 V. The main cluster size contribution is due to the cross talk generated by a particle traversing the chamber between the edge of two adjacent pads. A lower limit of 2.2 cm for the MWPC cathod pad x dimension is necessary not to exceed a cluster size of 1.2.

2.6.2.2 Triple Gas Electron Multiplier chambers

The innermost region of the first muon station, M1R1, is the one experiencing the highest charged particle flux, hence the one with the most stringent requirements: it must be able to sustain a rate up to 500 kHz/cm² and must have special radiation hardness to ensure ten years of LHCb operation without showing ageing effects. The only way to obtain such a performance in a wire chamber is to decrease the gain, at the price of a worse signal-to-noise ratio. The triple-GEM detector technology was then selected. The M1R1 area hosts 12 chambers with active area 20×24 cm² each. Two triple-GEM detectors are superimposed and their readout pads logically OR-ed. A cross section of the detector is shown in Fig. 2.20: three GEM foils are sandwiched between anode and cathode planes, so that the ionisation electrons, produced

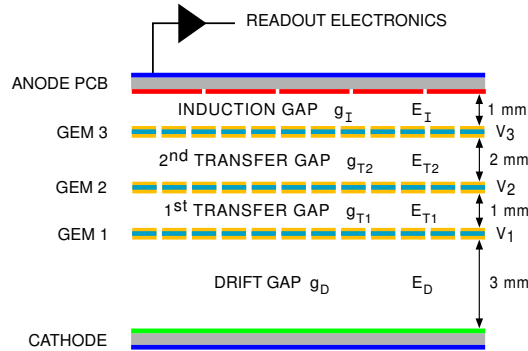


Figure 2.20: Schematic side view of a triple-GEM detector.

in the drift gap between the cathode and the first foil, are guided by electric fields through the three foils where they are multiplied, and they finally drift to the anode in the induction gap. The induced current signal is read on the pads. Tests on prototypes have shown how the mixture Ar/CO₂/CF₄ in the ratio 45:15:40 allows to achieve a time resolution better than 3 ns. The efficiency is above 96% in a 20 ns window at a gain of $6 \cdot 10^3$, with a maximum pad cluster size of 1.2.

2.6.3 Readout

The requirements of spatial resolution and rate capability vary strongly over the detector, hence detector size and granularity change from station to station and from region to region, even if detectors in the same station/region are equal. All the chambers are segmented into *physical pads*: anode wire pads or cathode pads in the MWPCs and anode pads in the GEM chambers. Each physical pad is read out by one front-end (FE) electronics channel. The detector read-out is different depending on the position in the System: all R4 chambers have wire read-out, while in regions R2 and R3 in M2 and M3 both wires and cathode pads are read out, with the anode wires grouped into vertical strips to measure the track x coordinate and the y provided by the cathode pads. The remaining chambers have pad read-out. The situation is summarised in tables 2.2 to 2.4.

The size of the physical pads is often limited by the noise and dead-time acceptable levels on FE channels, which are linked to the rate on the pad and to its electrical capacitance. This lead to physical pads that are smaller than required by spatial resolution. In these cases a *logical pad* is built OR-ing up

	M1/2/3/4/5
R1	12
R2	24
R3	48
R4	192

Table 2.2: Number of chambers per each region in the stations of the Muon System.

	M1	M2/3	M4/5
R1	GEM	W+2P	P
R2	2P	W+2P	P
R3	P	P	P
R4	W	W	W

Table 2.3: Chamber technology in the LHCb Muon System (W = anode wires, P = cathode pads, 2P = double cathode readout).

	M1	M2/3	M4/5
R1	384	224	192
R2	384	224	96
R3	192	192	96
R4	48	48	48

Table 2.4: Number of physical channels per chamber in the LHCb Muon System.

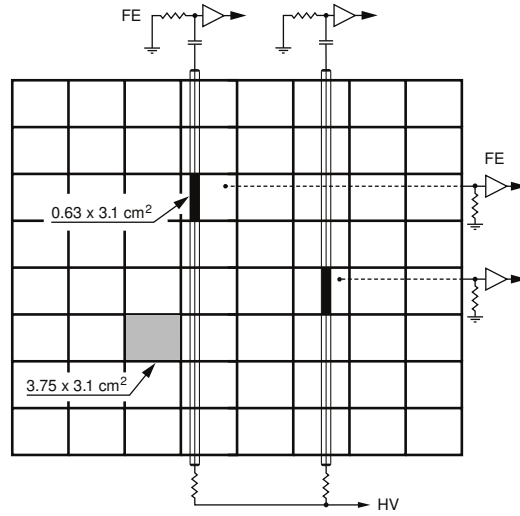


Figure 2.21: Scheme of the mixed readout adopted for R1-R2 regions in M2-M3 muon stations. Here the situation in M2R1 is represented. The coincidence between crossing vertical wire pads and cathode pads, as the one in grey, defines the logical pad, shown in black.

to four adjacent physical pads through the FE electronics. In some cases the required spatial resolution imposes x logical pad size which are too small to be built. This happens in R1-R2 of M2-M3. The solution is a mixed readout: a narrow wire-strip defines the x resolution, and a cathode pad defines the y resolution; the logical pads are then obtained as the AND of the wire and cathode pads, as illustrated in Fig. 2.21. The first station, M1, is the one experiencing the highest channel occupancy, therefore the signal from the logical pads are not further processed. On the contrary, in other regions of the subdetector it is possible to reduce the number of output logical fibres further OR-ing several contiguous pads building a large *logical channel*, in the form of horizontal (y) and vertical (x) strips. The information on the logical pad is then reconstructed by the coincidence of crossing strips. The sector defined by the length of x and y logical channel strips is the logic unit and is called *trigger sector*. In Fig. 2.22 the partitioning of a quadrant in M2-M3 in sectors is shown.

The relationship between physical channels, logical channels, logical pads and trigger sectors for the various parts of the muon system is summarised in numbers in tables 2.5 to 2.7.

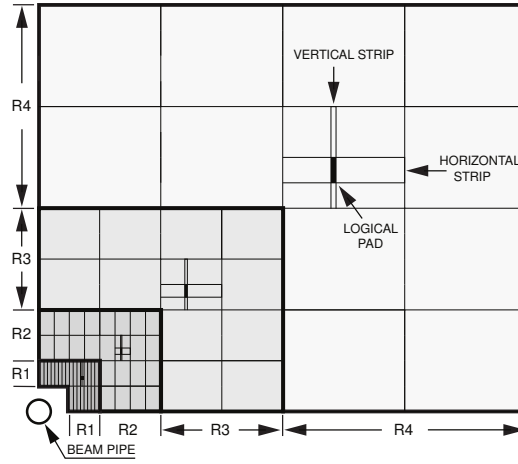


Figure 2.22: Front view of one top quadrant of stations M2 and M3 showing the sectors and a horizontal and a vertical strip per region.

	M1	M2/3	M4/5
R1	2PC-P = 1LP = 1LC	2PC-P = 6LP = 1LC-X 2PC-W = 8LP = 1LC-Y	2PC-P = 1LP = 1LC
R2	4PC-P = 1LP = 1LC	8PC-P = 12LP = 1LC-X 2PC-W = 4LP = 1LC-Y	2PC-P = 1LP 1LC-X = 4LP 1LC-Y = 3LP
R3	4PC-P = 1LP = 1LC	2PC-P = 1LP 1LC-X = 4LP 1LC-Y = 24LP	4PC-P = 1LP 1LC-X = 4LP 1LC-Y = 6LP
R4	4PC-W = 1LP = 1LC	2PC-W = 1LP 4LP = 1LC-X 24LP = 1LC-Y	8PC-W = 1LP 1LC-X = 4LP 1LC-Y = 6LP

Table 2.5: Relationship between physical channels (pads PC-P or wires PC-W), logical pads (LP), and logical channels (x view LC-X or y view LC-Y) in the LHCb Muon System. Physical channels are considered in pairs (*e.g.* 2PC-P is one double-gap), thus 2PC-P = 1LP = 1LC means that a double-gap corresponds to one logical pad and coincides also with a logical channel.

	M1	M2/3	M4/5
R1	192	384	96
R2	96	192	48
R3	48	96	24
R4	12	24	6

Table 2.6: Number of logical pads per chamber in the LHCb Muon System.

	M1	M2/3	M4/5
R1	-	6×8	-
R2	-	12×4	3×4
R3	-	24×4	6×4
R4	-	24×4	6×4

Table 2.7: Trigger sector size, reported in number of logical pads, per region in the LHCb Muon System.

2.6.4 Electronics

The electronics can be divided into the front-end electronics, mounted directly on the muon detectors, and the off-detector electronics, located in dedicated crates close to the sub-detector. A simplified overview of the architecture is shown in Fig. 2.23. The electronic chain has to prepare the information needed by the L0 muon trigger processor and to send data to the DAQ system. The process can be schematised as follows:

- the front-end CARDIAC boards perform the amplification, shaping and discrimination of the $\approx 122k$ chamber signals. In this step the time alignment to correct for different cable lengths and different chamber behaviours is performed;
- the logical-channel signals are generated by the logical OR of the physical channels directly on Front End boards and, when the trigger sector spans more than one FE board, on special Intermediate Boards (IB);
- the signals from the logical channels are sent to the Off Detector Electronics (ODE) boards where they are tagged with the number of the bunch crossing (BX identifier) and routed to the trigger processors via

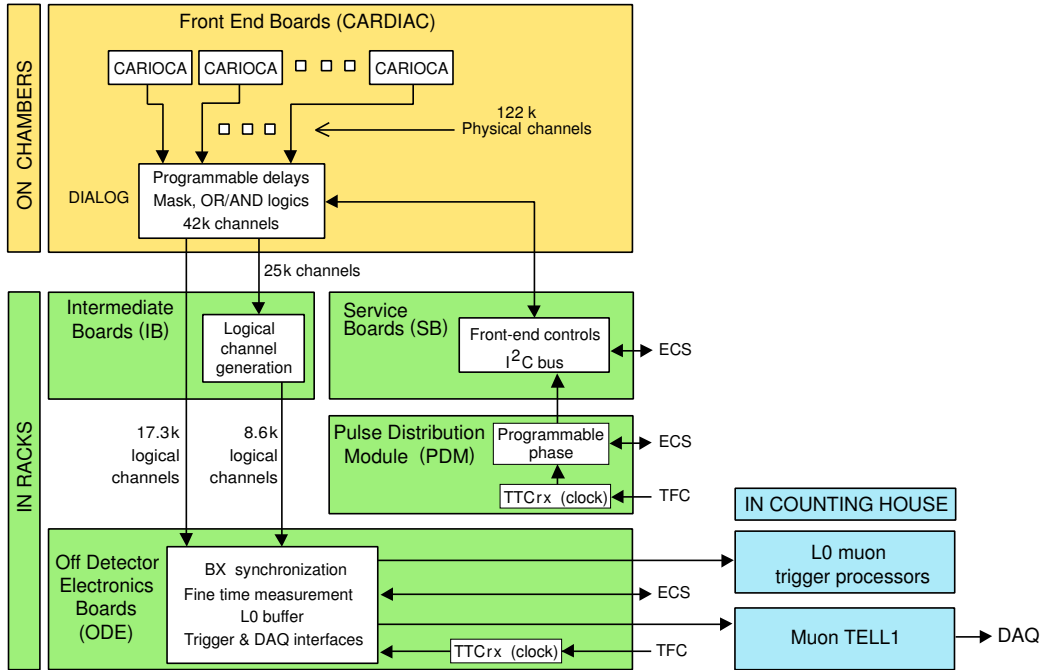


Figure 2.23: Scheme of the LHCb Muon System electronic chain.

zero-suppressed optical links; on the ODE also the time information, measured by the TDC, is added and data are transmitted to the TELL1 boards and from there to the DAQ system.

In the following the electronic chain will be described in detail.

2.6.4.1 Front-End Board (FEB)

Three dedicated radiation hard Application Specific Integrated Circuits (ASICs) have been developed to adapt the readout scheme to the different regions in the Muon System: CARIOCA, DIALOG and SYNC.

The chamber readout is performed via CARDIAC front-end boards directly plugged onto the chambers, each equipped with two CARIOCA chips and one DIALOG chip.

The CARIOCA is a front-end amplifier-shaper-discriminator chip. The current pre-amplifier can handle the large spread in detector capacitances encountered in the muon chambers (from 20 pF in M1R1 to 220 pF in M5R4 chambers). The dead time of a fired channel is in the range 50–60 ns. The CARIOCA allows for the setting of different thresholds for all the channels.

The DIALOG chip receive the outputs from the two CARIOCA chips and performs the logical OR of corresponding pads in the two layers of a chamber to form the logical channels.

For the GEM chambers a special version of the CARIOCA chip, the CARIOCAGEM, has been produced, which has lower threshold and longer shaping time to cope with the lower gas gain.

2.6.4.2 Service Boards and Pulse Distribution Module

The FEBs are managed by the Service Boards (SB), which handle the threshold settings for the CARIOCA chip and the setting of the AND/OR logics in the DIALOG chip. Each SB can control up to 192 CARDIAC boards.

A Pulse Distribution Module (PDM) resides in each of the 10 crates containing the SBs and is used for the time alignment of the Muon System.

2.6.4.3 Intermediate Board

The Intermediate Boards (IBs) are essential whenever the generation of the logical channels is not possible at the DIALOG level, *i.e.* when the logical channel spans more than one FEB. This is the case everywhere except for the whole M1 and the innermost region, R1, of the other stations.

2.6.4.4 Off Detector Electronics board

On the racks that host the IBs, also a total of 152 ODE is installed. Each board receives up to 192 logical channels and outputs data to the L0 muon trigger and to the DAQ system. The chip SYNC was especially developed for the LHCb muon ODEs. It has 8 input channels connected to one logical channel each, and one ODE boards hosts 24 SYNC chips. Each SYNC input channel has an independent TDC circuit, which measures and monitors the time phase of the input signal within the bunch crossing period. All the SYNC chips mounted on the same ODE are driven by the same master clock, which is synchronous with the LHCb BX structure. The SYNC provides the time compensation tagging each logical signal with a BX identifier. The resulting information is sent to the L0 trigger every 25 ns and stored in a pipeline, the *L0 buffer*, where it waits 4 μ s for the *L0 Decision Unit response*. In case of affirmative response from the Decision Unit, the event information is sent to the TELL1 and finally to the DAQ.

2.7 Trigger

The LHCb detector was conceived to operate at $\mathcal{L} = 2 \cdot 10^{32} \text{ cm}^{-2} \text{ s}^{-1}$, reduced by a factor ~ 50 with respect to the LHC nominal luminosity, in order to limit the number of p - p collisions per event, thus reducing the radiation damage and facilitating the triggering and reconstruction due to a lower channel occupancy. At the LHCb luminosity, the rate of visible interactions¹ is about 10 MHz, which has to be reduced to a maximum of about 3 kHz to match the processing time and allow the storage for the offline analysis. The reduction is achieved in two trigger levels: the Level-0 (L0) trigger, which is an hardware-implemented trigger; the High Level Trigger (HLT), which consists of a software application running on the CPUs of an event-filter farm (EFF). The L0 trigger operates synchronously with the 40 MHz bunch crossing frequency, while the HLT is executed asynchronously.

The trigger architecture for Run I and Run II is illustrated in Fig. 2.24 and the two main levels in the trigger are explained in more detail in the following.

2.7.1 Level-0 trigger

The aim of the L0 trigger is to reduce the LHC beam crossing rate of 40 MHz to a rate at which the HLT can process the event. As depicted in Fig. 2.25, the information collected for each event is sent to the L0 Decision Unit (L0-DU) which make the final decision performing an OR of the decisions of three sub-systems: the Calorimeters, the Muon System, and the Pile-Up system. Hence the discriminating variables are the transverse energy, E_T , deposited in the calorimeters, the transverse momentum, p_T , of muons and the multiplicity of primary interactions.

The Calorimeters Triggers look for high E_T particles (e , γ , π^0 or hadrons) forming clusters of 2×2 cells and selecting the clusters with the largest transverse energy. Particle identification is assigned according to the information from SPD, PS, ECAL and HCAL. The E_T for all HCAL cells is summed to reject beam crossing without visible interactions. The number of SPD cells with a hit are counted to measure the charged track multiplicity in the crossing.

¹An interaction is defined to be visible if it produces at least two charged particles that can be reconstructed from the hits in the VELO and T1–T3.

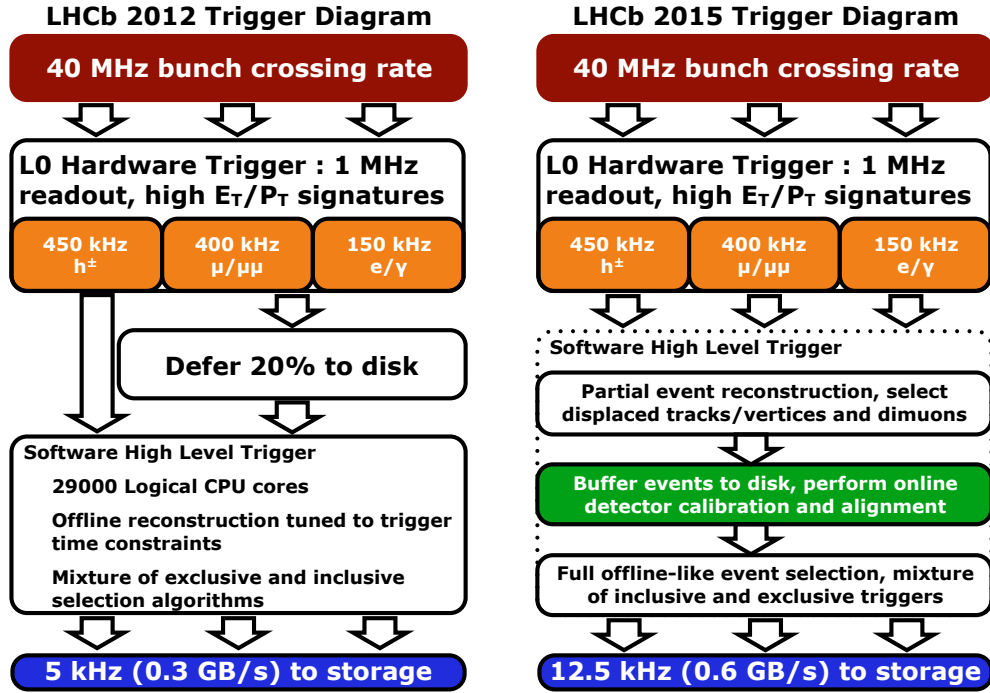


Figure 2.24: The LHCb trigger schemes for Run I (left) and Run II (right).

The Muon Trigger selects the two muons with the highest p_T for each quadrant of the muon detector. The muon chambers allow stand-alone muon reconstruction with a resolution on the transverse momentum of $\sim 20\%$.

The Pile-Up system, placed upstream of the VELO, rejects events with multiple visible interactions. The system uses two VELO R -sensor modules to estimate the primary vertex positions by measuring the radii of traversing tracks. If the distribution of the position in z of the primary vertices shows a second peak in addition to the highest found peak, the event can be rejected.

The time between the $p-p$ interaction and the decision of the L0-DU is fixed to a maximum of $4 \mu\text{s}$, including the time-of-flight of the particles, cable and front-end electronics delays ($\sim 2 \mu\text{s}$).

The L0 trigger selectivity can be adjusted depending on the running conditions. During Run I, in order to optimise the resources use, a fraction of $\sim 20\%$ of L0-accepted events was deferred to disk in order to be processed during the inter-fill time.

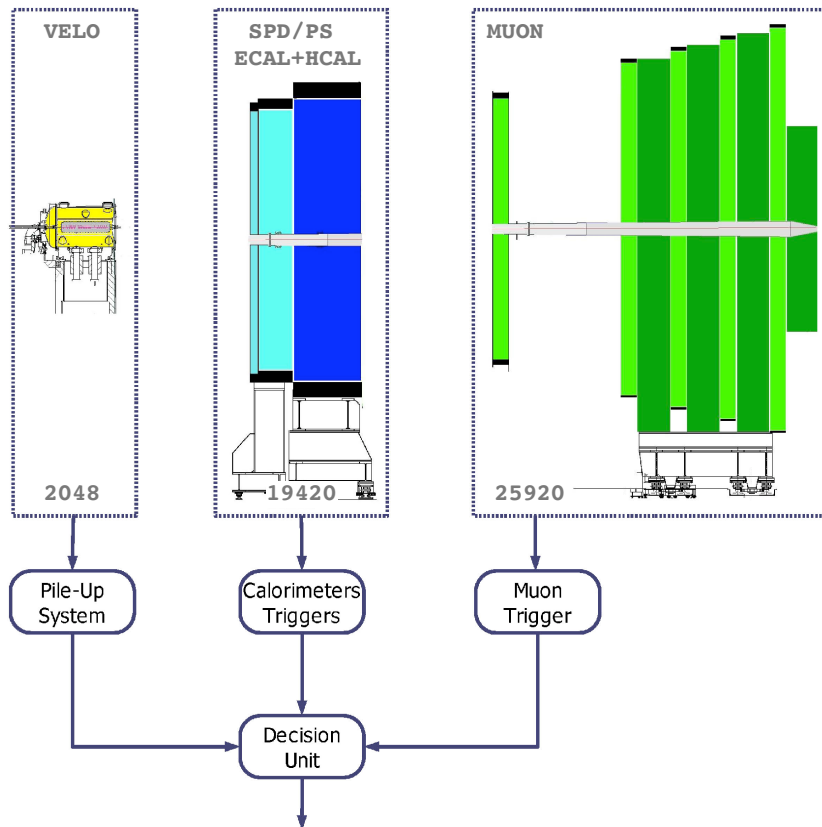


Figure 2.25: Overview of the L0 trigger. Numbers are related to the channels received by each one of the three sub-systems: every 25 ns the pile-up system receives 2048 channels from the pile-up detector, the calorimeters triggers receives 19420 channels from SPD, PS, ECAL, and HCAL, finally the muon trigger handles the 25920 logical channels from the Muon System.

2.7.2 High Level Trigger

The High Level Trigger (HLT) is a software trigger implemented in C++ whose algorithms run on an event filter farm (EFF) of ~ 2000 CPUs. Its software nature makes it extremely flexible, so that it can be modified when needed to match running conditions and physics requirements.

The HLT is divided into two phases that are executed in sequence: HLT1, which has to confirm the L0 decision and to perform a partial event reconstruction; HLT2, where a complete event reconstruction is performed.

The HLT1 is divided into *alleys*, one for each L0 sub-trigger. Level-0 objects (clusters from the calorimeter and muon tracks) are further processed to add information from VELO and T-stations. About $\sim 15\%$ of these events are selected by multiple triggers, and will consequently pass by more than one alley.

The rate of events accepted by HLT1 alley is sufficiently low to allow HLT2 to perform a full event reconstruction at the same precision as the off-line analysis. The HLT selection differs from the off-line reconstruction in not using a Kalman filter since this is too CPU consuming. Very loose cuts are used to select a set of tracks to form composite particles (*e.g.* $\phi \rightarrow K^+K^-$ or $J/\psi \rightarrow \mu^+\mu^-$) that are subsequently used for different inclusive (*e.g.* $B \rightarrow \phi X$) and exclusive (*e.g.* $B \rightarrow \phi J/\psi$) selections. The final trigger is the logical OR of the inclusive and exclusive selections, and the event rate is reduced to about 2 kHz, which can be written to storage for further analysis.

During Run II the trigger underwent the most innovative interventions. The 20% increase in multiplicity due to the increased luminosity reflects in an increment of the signal, thus the trigger has to be more selective, since the maximum read-out rate is limited to 1 MHz. In this phase 100% of the events can be buffered to disk before HLT2 while performing the online alignment and calibration of the sub-detectors. The new streaming strategy also allows to only store the event candidates information for a selection of physics analyses thanks to a direct trigger reconstruction called Turbo Stream, with the advantage of reducing the event size of one order of magnitude. Currently, the 20% of the HLT output bandwidth is dedicated to the Turbo Stream.

2.7.3 Trigger decision categories: TIS and TOS

An event that has been written on tape has been necessarily selected by the trigger. Accepted events are identified by the trigger decision that inter-

vened. In particular two categories can be identified:

- Trigger On Signal (TOS): the trigger was fired by particles belonging to the studied decay;
- Trigger Independent of Signal (TIS): events that passed the trigger selection because of particles not used to reconstruct the decay under study. This means that removing a TIS candidate the trigger will still accept the event.

2.8 Simulation in LHCb

The Monte Carlo production in LHCb uses a software package called Gauss [31] to simulate the events. The procedure starts with Pythia [32] to simulate the proton collisions, then EvtGen [33] creates the particle decays. After the generation phase, Geant4 [34] is used to propagate the created particles through a simulated version of the LHCb detector. This step makes use of the Detector Description Data Base (DDDB), which stores information about the size, shapes and materials composing the detector. Finally, the simulation of the digital output of the detector is done using a software called Boole [35], which simulates the digital output of the detector. The Moore [36] package allows to re-apply the software trigger on the Boole output events.

2.9 Reconstruction and analysis

The necessity to store the enormous amount of data collected by the experiments at the LHC is a crucial point to deal with. The so-called Worldwide LHC Computing Grid (WLCG) [37] provides the computing resources that store, distribute and analyse the data. It is organised in a multi-tier structure, where each tier provides a specific set of services. The events filtered by the EFF are first stored at the Tier-0 at CERN. These data contain basic information on the detector, like the number of hits on a system or the read-out response of sub-detectors, and are stored in a file format called RAW. The RAW data are then copied to different Tier-1s to be further processed. After, the full event reconstruction is performed (in LHCb this is done using the Brunel package). The output of the reconstruction contains physics quantities like primary vertex coordinates, track trajectories, and momen-

tum and energy of calorimeter clusters. At this point data are saved in the file format called SDST.

Despite the huge storage capabilities provided by the WLCG, only a small fraction of the data produced at LHCb can be stored on disk. Since the fraction of events useful for each single analysis is rather small, it becomes mandatory to apply a preselection of events. This stage is named *Stripping*. The Stripping procedure applies loose selections on the collected data, filtering the sample and creating the candidates that will be used in the final analysis. The output file format is called DST and contains the possible candidates together with the information of the reconstruction phase and also the RAW data relative to each event. Stripping lines corresponding to similar physics programmes are grouped into *Streams*, so to decrease the amount of time required to extract the information about the signal decays. The DSTs can be used for user analysis and they are stored on disk for a faster and more efficient access. The corresponding RAWs and SDSTs are then transferred to magnetic tapes.

The LHCb Upgrade

The outstanding results obtained during Run I and Run II show that the LHCb detector is performing extremely well. Nevertheless, to fully exploit its flavour physics potential, LHCb has planned a high-luminosity phase to perform very high precision measurements so that the experimental sensitivity could approach the same order of magnitude of the theory uncertainties. This cannot be achieved without upgrading the detector [38, 39]. The upgraded detector will go beyond the limitations due to the fact that the trigger yield on hadronic events saturates already at $4 \cdot 10^{32} \text{ cm}^{-2} \text{ s}^{-1}$, as shown in Fig. 3.1, because of the available bandwidth and the limited discriminating power of the hadronic hardware trigger. The strategy is to increase the luminosity to $\mathcal{L}_{inst} = 2 \cdot 10^{33} \text{ cm}^{-2} \text{ s}^{-1}$ completely removing the L0, and to reading out the entire detector at 40 MHz. The following assumptions are made for the upgrade:

- the proton beams will collide at \sqrt{s} of 14 TeV;
- the instantaneous luminosity in the LHCb experiment will be at least $\mathcal{L}_{inst} = 2 \cdot 10^{33} \text{ cm}^{-2} \text{ s}^{-1}$, and will be achieved with a bunch separation of 25 ns and a pile-up of $\nu = 7.6$;
- the polarity of the LHCb dipole magnet will change with a similar frequency as in Run I and Run II, to achieve the same amount of collected data with each configuration for a better control of potential systematic biases.

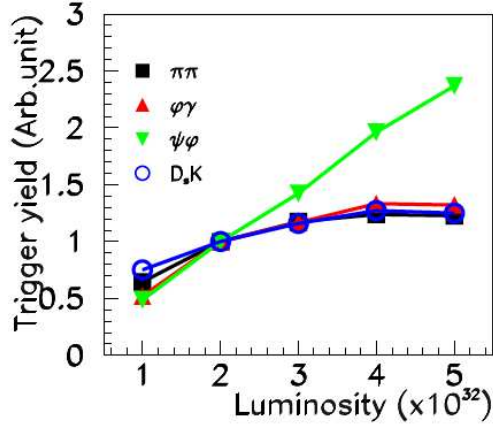


Figure 3.1: Trigger yield for different B mesons decays. Each point is normalised to the trigger yield expected in nominal conditions at $\mathcal{L} = 2 \cdot 10^{32} \text{ cm}^{-2} \text{ s}^{-1}$.

The consequence of the 40 MHz readout is that all the sub-detector front-end and back-end electronics (only compatible with the current 1 MHz readout) must be replaced and the sub-detectors must be adapted to the new conditions.

In this Chapter the physics justification for the high luminosity phase is presented together with the modifications foreseen for the LHCb detector; in particular, the new Muon System will be described in detail in the last section.

3.1 Physics Motivation

The current detector has been demonstrated to be able to achieve all the purposes foreseen for the first phase of data taking, allowing to significantly extend the precision of many key observables in B and D physics. However the upgrade is mandatory for improving the selection efficiency for hadronic final states in B and D decays. The upgraded version of the detector, with the possibility to run at higher luminosity, the removal of the hardware trig-

ger and the strengthening of particle identification capabilities will allow to collect 50 fb^{-1} of data in ten years of operation. First of all, the upgraded experiment will play a key role in the field of quark flavour physics, which provides a powerful method for the search for New Physics effects and their potential characterisation. In addition to this, a considerable number of physics areas of interest will benefit from the increased sample size available with the upgrade: examples include opportunities in the lepton sector (including the search for lepton-flavour violation in τ decays and for low-mass Majorana neutrinos), electroweak physics such as the determination of the weak mixing angle, the search for long-lived new particles and QCD studies. The upgraded LHCb experiment can thus be regarded as a multi-purpose forward detector, which will be able to make measurements complementary to, or of higher sensitivity than, those possible at the LHC general-purpose detectors, ATLAS and CMS.

In the search for effects of processes beyond those foreseen in the Standard Model in quark flavour physics, the studies can be divided into two main categories:

- **exploration:** this category includes decay modes or observables *a priori* very sensitive to New Physics, but which are currently not accessible. Their existence means that the physics gain of the upgrade cannot be assessed by mere applying a “ $1/\sqrt{N}$ ” scaling to the expectations of the existent detector;
- **precision studies:** these include the measurement of known parameters with improved sensitivity, which will allow for more precise comparison with the theory.

The topics in the “exploration” group are expected to migrate to the category of “precision studies” in the upgrade phase.

As examples of key studies, three cases are briefly introduced in the following.

In the Standard Model, the Cabibbo-Kobayashi-Maskawa (CKM) matrix determines the coupling of quarks to weak charged currents determining weak-interaction eigenstates deriving from mass eigenstates mixing. The complex phase appearing in CKM elements is the source of CP violation. The measurement of the angle γ , defined as $\gamma = \arg[-V_{ud}V_{ub}^*/(V_{cd}V_{cb}^*)]$, of the Unitarity Triangle from $B \rightarrow DK$ decays is a SM benchmark. It is one of the least well known parameters of the quark mixing matrix: its value is known with an uncertainty of 10° with negligible theoretical uncertainties,

at the level of $\delta\gamma/\gamma = \mathcal{O}(10^{-6})$. Data collected during Run III are expected to improve its precision by a factor of 10 [40].

Decays dominated by $b \rightarrow s$ penguin loop transitions like $B_s^0 \rightarrow \Phi\Phi$ are particularly interesting for being highly sensitive to NP contributions and their effect could appear in both time-dependent CP violation, which is predicted to be close to zero in the SM, and in angular distributions. A first measurement of the CP -violating weak phase Φ_s in LHCb has already been published [41] and increasing the data set to the integrated luminosity of the upgraded LHCb, the statistical uncertainty is expected to reach 0.03, which is close to the accuracy of SM predictions from theory, which is 0.02.

Like $B_s^0 \rightarrow \Phi\Phi$, the decays $B_s^0 \rightarrow \mu\mu$ and $B^0 \rightarrow \mu\mu$ are forbidden at tree level: due to the absence of direct FCNC, they can only occur via higher order penguin diagrams. New Physics may contribute to these decays, which are highly suppressed in the SM, enhancing the branching fraction beyond the SM predictions. First evidence for $B_s^0 \rightarrow \mu\mu$ has been found in LHCb [42], then its observation and the evidence for $B^0 \rightarrow \mu\mu$ from the combined analysis of data collected from LHCb and CMS has been published [43]. The presented results are consistent with SM predictions, and larger data sets may allow a distinct observation of $B^0 \rightarrow \mu\mu$ and a higher precise measurement of the BF thus revealing possible effects of NP.

3.2 The upgrade of the LHCb detector

The main innovation introduced by the upgrade will be the implementation of the 40 MHz read-out, which will require the replacement of all the front-end electronics. In addition to this, several subsystems of the LHCb detector have to be modified to cope with the new data taking conditions. Figure 3.2 shows the side view of the upgraded LHCb detector. The main changes are introduced in the following.

In addition to the full 40 MHz readout, the trigger strategy (schematised in Fig. 3.3 will take advantage of the removal of the L0 trigger (which was responsible for the largest inefficiencies in the trigger chain). Currently, the 20% of the HLT output rate is dedicated to the Turbo stream, and its contribution is foreseen to grow so that after the LHCb upgrade the majority of the analyses will profit from it.

The challenge for the VERtEx LOcator (VELO) is to maintain and possibly improve its performances at the increased intended luminosity, and also to be sufficiently radiation hard; this can only be achieved with a complete

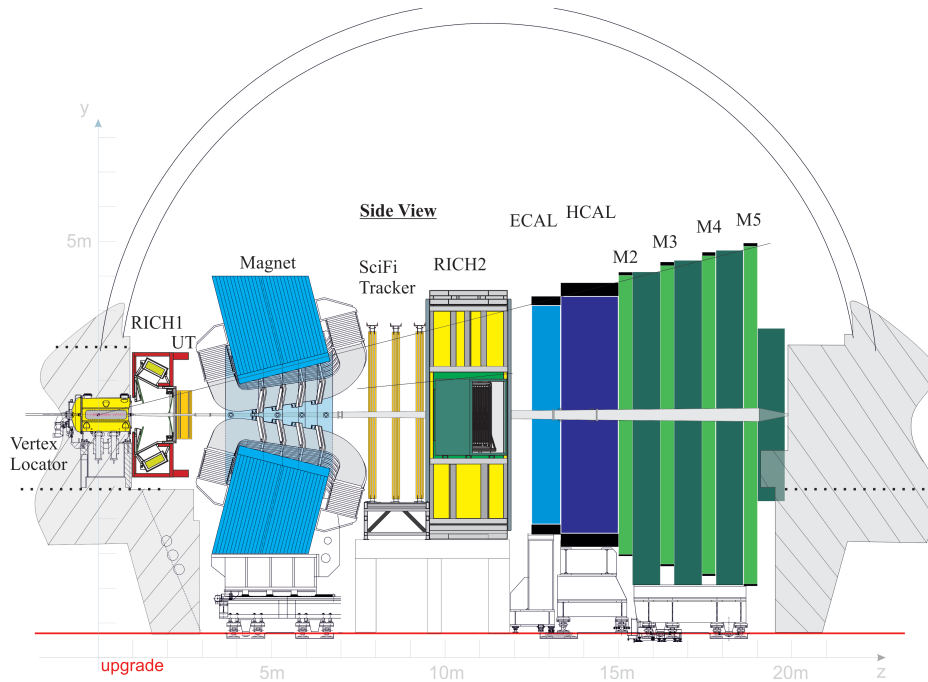


Figure 3.2: Two-dimensional view of the LHCb experiment in its upgraded configuration.

replacement of the silicon sensors and of the electronics. The conceptual layout will remain unvaried but the strip technology will be replaced with pixels of reduced thickness (from $300 \mu\text{m}$ to $200 \mu\text{m}$) to cope with the increased track multiplicity. The expected performances on the IP resolution are shown in Fig. 3.4.

The TT needs to be substituted because the integrated front-end chip is not compatible with the 40 MHz read-out and cannot be replaced without damaging the module, for the current bounding of four consecutive sensors to form strips will lead to unacceptably high occupancy at high luminosity, and finally for being not sufficiently hard. The TT will be substituted with the Upstream Tracker (UT), which will still consists of four planes of silicon strips. The improvement include thinner sensors (from $500 \mu\text{m}$ to $250 \mu\text{m}$) with finer segmentation. In addition to this, the signal will be processed at the sensors rather than being taken out with long cables, allowing to reduce the electronic noise. Hits in the Upstream Tracker will play a major role in the rejection of ghost tracks. The requirement of having three or more UT hits on tracks reconstructed in all sub-detectors (long tracks) is expected to

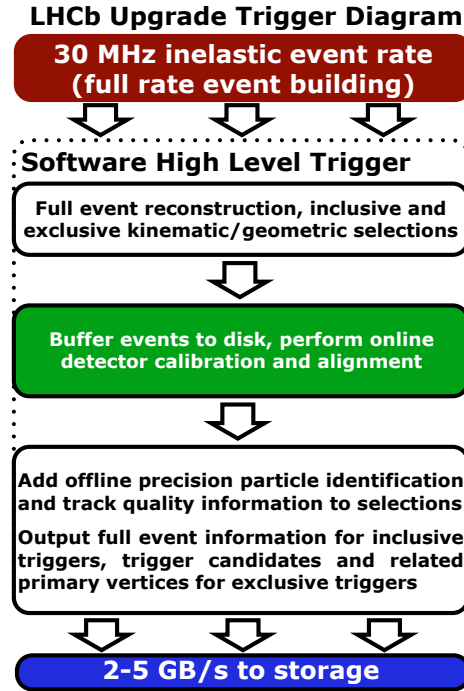


Figure 3.3: Foreseen trigger scheme for Run III in the LHCb experiment.

reduce the ghost track rate of a factor 2 – 4.

The T stations geometry was chosen to limit the maximum occupancy of the OT in the external region to 10% at design luminosity. Improvements have already been made to be able to collect data at an instantaneous luminosity of $5 \cdot 10^{32} \text{ cm}^{-2} \text{ s}^{-1}$ with a maximum occupancy of 25%. Nevertheless, at upgrade conditions the OT occupancy is expected to definitely be intolerable. The solution is to replace the modules with scintillating fiber mats, which allow optical signal transportation outside the acceptance volume and its read-out by Silicon Photonmultipliers (SiPMs). The new modules will be hosted in three stations of four layers each, rotated by a stereo angle of $0^\circ/+5^\circ/-5^\circ/0^\circ$. The new Scintillating Fibre Tracker (SciFi Tracker) has been designed to reach an efficiency on the single hit ε_{hit} of about 99% and a spatial resolution on the single hit on the bending plane σ_{hit} of about $100 \mu\text{m}$.

For what concerns the RICH sub-detectors, a change of the overall structure is not required. Significant modifications are only planned for RICH1, whose optical layout has to be modified to reduce the large foreseen occu-

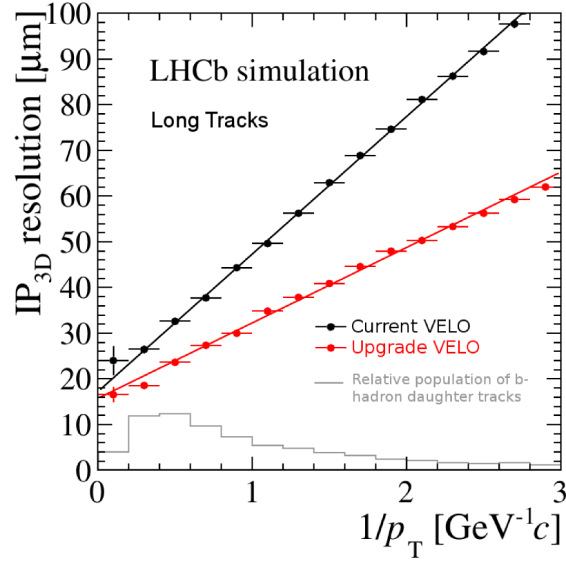


Figure 3.4: Impact parameter resolution as a function of $1/p_T$ for particles reconstructed in all tracking sub-detectors. The current VELO is shown in black circles with the upgraded VELO is represented by red squares. Both are evaluated at $\nu = 7.6$ and $\sqrt{s} = 14$ TeV. The grey histogram shows the b -hadron daughter tracks relative population in each bin.

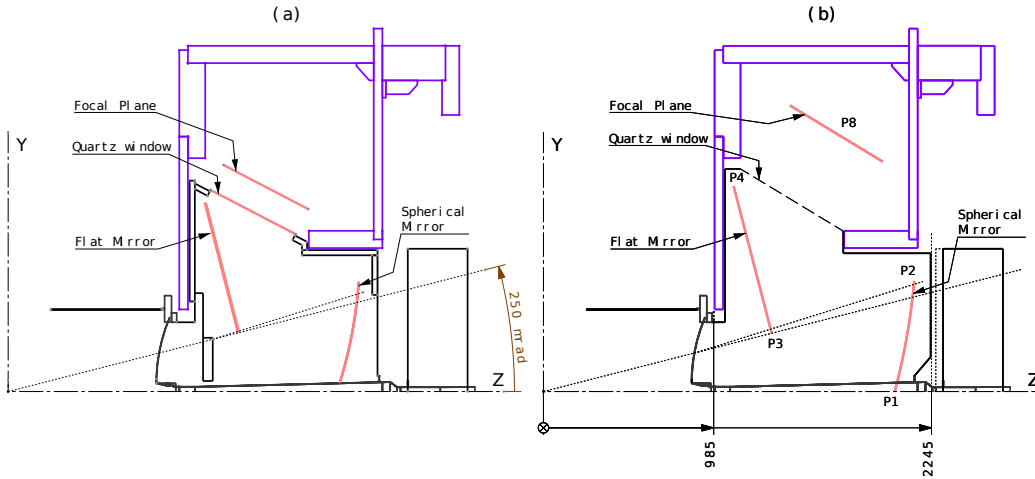


Figure 3.5: Layout of the optical geometry for the current (a) and upgraded (b) RICH1 sub-detector.

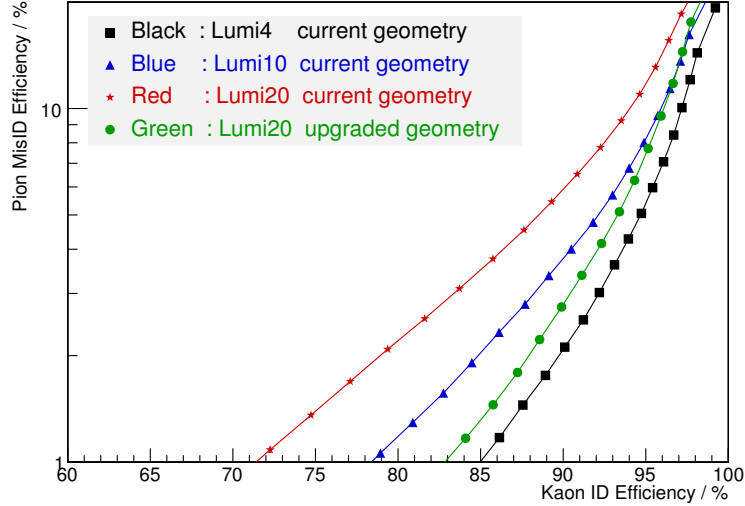


Figure 3.6: Pion misidentification as a function of kaon identification efficiency for the instantaneous luminosities of $3.9 \cdot 10^{32}$ (Lumi4), $10 \cdot 10^{32}$ (Lumi10), $20 \cdot 10^{32}$ (Lumi20), studied using the current geometrical layout of RICH1. The performances corresponding to Lumi20 with the upgraded geometry are also reported.

pancy in the central region of the detector. To halve the occupancy, the focal length of the spherical mirrors will be increased by a factor of $\approx \sqrt{2}$. To restore the focusing, the spherical mirrors radius of curvature will also increase. The changes will also improve the Cherenkov angle resolution reducing the aberrations of the spherical mirrors. The features of the upgraded RICH1 are visible from the comparison of Fig. 3.5 (a) and (b). The particle identification performance for the current geometry is shown in Fig. 3.6 corresponding to three different luminosities, and is compared to the expected performances for the upgraded sub-detector at the instantaneous luminosity of $20 \cdot 10^{32} \text{ cm}^{-2} \text{ s}^{-1}$: as the luminosity increases, the plot shows a loss in performance that is mostly recovered when using the upgraded RICH1.

During the first two runs of data taking, the Calorimeter system performed well despite the decision to operate at higher luminosity than foreseen. In view of Run III the removal of SPD and PS is foreseen, since their main use is in the L0 trigger. As a consequence, the Calorimeter system design will be simpler, with great advantages in terms of calibration and

project costs. The modules of ECAL and HCAL already meet the requirements for the upgrade. The current Photonmultipliers will be kept and the gain will be reduced by a factor of 5 to keep the same mean anode current as today. As in the previous cases, the new readout at 40 MHz will require new design of the front-end and back-end electronics. Radiation damage studies show a sizeable degradation for the innermost modules of HCAL, but they are not expected to remain operational for the full life span of the upgrade: the eventual loss of HCAL central cells is expected not to impact upon the physics performance of the experiment. ECAL modules are expected to be able to remain operational up to an integrated luminosity of $\sim 20 \text{ fb}^{-1}$ so the substitution of the most irradiated modules is only foreseen for the third Long Shutdown of the LHC.

The current muon stations M2 to M5 already meet the requirements for the upgrade, with the usual exception of the readout electronics. This is not true for the first muon station, M1, which will be removed. The upgrade programme for the Muon System will be discussed in more detail in the next Section.

3.3 The upgraded Muon System

3.3.1 Upgrade requirements and overview

For the upgrade, the Muon System must ensure high reconstruction and identification efficiencies for muons while keeping the misidentification fraction of other particles as low as possible [44]. Being the most shielded sub-detector, the Muon System will tolerate particle rates up to an instantaneous luminosity of $2 \cdot 10^{33} \text{ cm}^{-2} \text{ s}^{-1}$ at the collision energy of 14 TeV in all stations apart from M1, which will thus be removed; the particle flux is expected to be very high in the innermost region of M2, and so the installation of additional shielding around the beam-pipe in front of M2 is foreseen. Finally, the off-detector readout electronics only provides information at the limited rate of 1 MHz; for this reason the current Off Detector Electronics (ODEs) boards will be substituted by the new ODEs (nODEs) based on a new radiation tolerant custom ASIC, the nSYNC. In addition to these changes, new algorithms are under study that are able to improve the pion rejection performances at high pile-up conditions.

3.3.2 Detector performances at high luminosity

The detector requirements that have been described in the previous subsection must be maintained up to an instantaneous luminosity of $2 \cdot 10^{33} \text{ cm}^{-2} \text{ s}^{-1}$ and for an integrated luminosity of 50 fb^{-1} . The main limiting factor in the detector efficiency is the intense flux of charged and neutral particles and the related appearance of ageing effects in the long run.

It has been possible to test the high-rate behaviour of the MWPCs at the CERN Gamma Irradiation Facility (GIF) using a 100 GeV muon beam superimposed upon the 662 keV γ flux of variable intensity from a ^{137}Cs radioactive source [45]. The detectors were tested with current densities corresponding to the value expected in the most irradiated chamber of M2 at the instantaneous luminosity of $1 \cdot 10^{33} \text{ cm}^{-2} \text{ s}^{-1}$, which corresponds to 30 nA/cm^2 . The muon beam also allowed to study the behaviour of the front-end electronics. The tests showed no deterioration in the performance, except for dead time effects. Possible space charge effects that might arise at $2 \cdot 10^{33} \text{ cm}^{-2} \text{ s}^{-1}$ will be of minor importance. The four gas gaps construction of the chambers guarantees the necessary redundancy in the system to control potential inefficiencies. These results have been confirmed in two dedicated test runs in 2012: one at $10^{33} \text{ cm}^{-2} \text{ s}^{-1}$ with 50 ns bunch spacing, and one at lower luminosity but with 25 ns bunch spacing. Data collected during the past years at LHCb have been used to extrapolate the behaviour of the system at the upgrade conditions, since the particle rates measured in the various stations and regions of the muon detector are found to scale very well with the luminosity over several orders of magnitude. The extrapolated rates are reported in Table 3.1.

The ageing effect on MWPCs has been studied in tests at the CERN GIF and the ENEA Calliope Gamma Facility, accumulating a total charge of about 0.45 C/cm with no degradation in performances. This value only represents the 70% of the maximum integrated charge expected in the inner region of M2 after the ten years of data taking. As a consequence, detector ageing is expected to be a concern only after LS3, when about half of this luminosity will have been collected.

3.3.3 Upgraded detector layout

A fundamental task is currently performed by the first muon station, M1, for it guarantees an adequate muon momentum resolution in the L0 trigger. This is not the case for the upgrade, when the huge hit occupancy would make

Region	Rates (kHz/cm ²)		
	Minimum	Average	Maximum
M2R1	162±28	327±60	590±110
M2R2	15.0±2.6	52±8	97±15
M2R3	0.90±0.17	5.4±0.9	13.4±2.0
M2R4	0.12±0.02	0.63±0.10	2.6±0.4
M3R1	39±6	123±18	216±32
M3R2	3.3±0.5	11.9±1.7	29±4
M3R3	0.17±0.02	1.12±0.16	2.9±0.4
M3R4	0.017±0.002	0.12±0.02	0.63±0.09
M4R1	17.5±2.5	52±8	86±13
M4R2	1.58±0.23	5.5±0.8	12.6±1.8
M4R3	0.096±0.014	0.54±0.08	1.37±0.20
M4R4	0.007±0.001	0.056±0.008	0.31±0.04
M5R1	19.7±2.9	54±8	91±13
M5R2	1.58±0.23	4.8±0.7	10.8±1.6
M5R3	0.29±0.04	0.79±0.11	1.69±0.25
M5R4	0.23±0.03	2.1±0.3	9.0±1.3

Table 3.1: Expected rates on the muon sub-detector when operating at an instantaneous luminosity of $2 \cdot 10^{33} \text{ cm}^{-2} \text{ s}^{-1}$ at $\sqrt{s} = 14 \text{ TeV}$. The reported values are averages, in kHz/cm², over the chamber with minimum illumination, the entire region, and the chamber with maximum illumination. The values are obtained from an extrapolation of measured rates at 8 TeV [28].

the association of M1 hits to muon track segments impossible; in addition to this, as a consequence of the foreseen Lower Level Trigger (LLT), the muon momentum resolution requirements can be relaxed; finally, the first station is not used for muon identification purposes. In the upgrade programme the removal of station M1 has thus been scheduled.

The performance of the remaining stations, M2 to M5, already meets the requirements for the upgrade for what concerns trigger and particle identification efficiency. Their physical layout will not be modified, however two critical situations require a solution:

- in the logical channels in M5R4, which result from the logical OR of

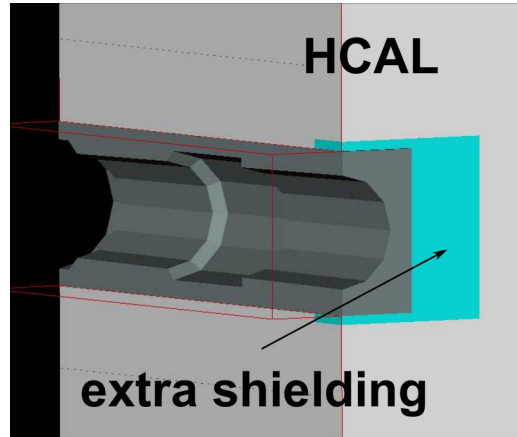


Figure 3.7: Location of the extra shielding foreseen behind HCAL [28].

24 front-end channels and reach an area of 0.5 m^2 , the occupancy is already high and this leads to inefficiencies of a few percent due to dead time. To reduce these inefficiencies, which will become more severe at the upgrade luminosity, it is planned to increase the granularity of the logical channels by removing the IBs and replacing them by new ODEs;

- in the present detector, the nuclear interaction length in front of M2 is $6.8 \lambda_I$, 33% less compared to the thickness foreseen in the original design. The reduced thickness has an acceptable absorption when running at design luminosity. However, the hit rate is expected to be very high in the innermost muon chambers, especially because of insufficient absorption of particles produced in hadron showers close to the beam-pipe. To ensure a better absorption of the particle flux, a lead and tungsten shielding will be installed around the beam-pipe behind HCAL, as indicated in Fig. 3.7.

3.3.4 Upgraded read-out and control electronics

The task of the muon read-out electronics is to convert the analogue signals extracted from the detector front-end channels into logical channels to input to the L0-muon trigger processors. The Muon System read-out architecture has to be reoptimised for the upgrade for several reasons:

- the TDC information is only extracted at 1 MHz;

- the Timing Fast Control (TFC) that provides all the synchronisation signals in the present clock distribution system would need to be maintained in operation or emulated for the Muon System alone;
- the possible obsolescence of electronics components has to be taken into account.

The solutions have been already identified and include the replacement of the ODE, SB and PDM with new electronics boards, maintaining the present crates and power supply based on the MARATON system; the upgraded electronics will have to maintain the electric and mechanical compatibility with the current system and also to allow a TDC readout at 40 MHz, to allow for possible increase in read-out channel granularity, and finally to minimise the number of read-out links. More in detail, the main component of the new read-out will be the new Off-Detector Electronics board (nODE). The nODE will have up to 192 input channels.

The core of the nODE will be a new radiation tolerant custom ASIC, the new SYNC chip (nSYNC), which will integrate all the required functionalities of clock synchronisation, bunch crossing alignment, hits production, time measurements, histogram capability and buffers, in addition to the zero suppression algorithm for the TDC data and the interfaces to the data acquisition and TFC/ECS systems. In particular, the nSYNC will have 48 input channels, equipped with a 4-bit TDC each, which will measure the phase of incoming signals with respect to the LHCb master clock. The TDC information will be used to build a histogram of the incoming signal phase in order to perform a fine-time synchronisation that is crucial to achieve the required Muon System efficiency.

The DAQ interface must allow the data transfer of the binary hit information to the corresponding TELL40 boards. The interface must allow the data transfer of the TDC information to the TELL40 boards. A hit map will provide the data geographic addressing that will be used for the trigger algorithm and for TDC data decoding. Such a choice will allow an optimisation of the bandwidth usage.

A single type of nODE is foreseen therefore a modularity of 96 bits per hit link is required to fit all the trigger unit topologies present in the various stations and regions of the Muon System. The nODE will also be compatible with the current IB boards. In this way a simple replacement of an IB with a nODE will reduce the logical channel dimension and their occupancy.

The current Muon Front-End Control electronics (MuFEC) based on the SB and the PDM, which is used to control, monitor and test each channel

of the detector front-end, will maintain the present architecture for what concerns the crate allocation and module partitions. The new MuFEC will use the GBT and Versatile link components to implement a TFC interface compliant with the new standard foreseen for the LHCb upgrade. The new system will be built using three new components: a new PDM board (nPDM); a new SB (nSB); a new backplane to dispatch the communication channels from the nPDM to the nSB boards. The replacement of the CANbus with a faster optical data link will allow all system operations to be directly performed via software. The MuFEC upgrade will benefit from the new architecture avoiding the use of obsolete components and improving control and monitoring speed.

Muon Identification at LHCb

The importance of muons in LHCb is related to the fact that they are present in the final state of many of the key decays, sensitive to new physics effects, that are studied at the LHCb experiment. In addition to this, they are crucial for the flavour tagging of neutral B mesons.

The main requirement for the muon identification procedure is to provide high muon efficiency while maintaining the incorrect identification probability (misidentification probability) for other particles as low as possible [46].

4.1 The Muon Identification procedure

In the muon identification strategy adopted by the LHCb experiment four steps can be distinguished:

- **IsMuon**: the first step is a loose binary selection based on the penetration of muons through the muon stations and, in particular, through the calorimeters and the iron filters; IsMuon has been optimised to provide high efficiency and it also ensures a reduction of the misidentification probability of hadrons to the percent level;
- **muDLL**: a likelihood for the muon and the non-muon hypotheses can be associated to muon candidates, based on the pattern of hits around the extrapolation of charged particles trajectories to the muon stations. The logarithm of the ratio between the likelihoods for the muon and

the non-muon hypotheses is used as a discriminating variable and is called muDLL;

- **DLL**: the information from the muon system can be combined with information from the calorimeters and the RICHes. In this case, the discriminating variable DLL is the logarithm of the ratio between the likelihoods for muon and pion hypotheses.
- **Multivariate methods**: in particular the Boosted Decision Tree and the ProbNN (this one belonging to the Neural Networks category). Multivariate algorithms will be described more in detail in the appendix.

Other variables can be introduced that allow to further reject false candidates. A cut on the quality of the tracks associated to a muon candidate can be introduced that takes into account the number of tracks that share a hit with a given muon candidate; this variable is called NShared and will be described in more details later in this chapter.

4.1.1 IsMuon selection

Muon candidates are selected by extrapolating the tracks reconstructed in the tracking system to the muon stations and searching for a hit within a Field of Interest (FoI) around the extrapolated track. In order to take into account the stopping power for high-energy muons in matter, the number of station required to trigger IsMuon is a function of the track momentum p , as shown in Table 4.1. Also the size of the FoI is a function of p because of the multiple scattering that can modify the particle trajectory when traversing the material, and is defined as

$$FoI = a + b \cdot e^{-c \cdot p}. \quad (4.1)$$

The parameters a , b , and c are different for every station and region and are optimised separately in both x and y directions. The values for the parameters have been determined using muons from a full detector Monte Carlo simulation.

4.1.2 Likelihood for muon and non-muon hypotheses

To associate a probability of being muons to muon candidates, a discriminating variable D^2 is introduced that is defined as the average squared distance

IsMuon	
Momentum range (GeV/c)	Requirement
$3 < p < 6$	M2 and M3
$6 < p < 10$	M2 and M3 and (M4 or M5)
$p > 10$	M2 and M3 and M4 and M5

Table 4.1: Stations required to have hits as a function of momentum range in order to trigger IsMuon decision.

of the hits in the muon chambers with respect to the extrapolation of the tracks weighted by the pad resolution:

$$D^2 = \frac{1}{N} \sum_i \left\{ \left(\frac{x_{\text{closest}}^i - x_{\text{track}}^i}{\text{pad}_x^i} \right)^2 + \left(\frac{y_{\text{closest}}^i - y_{\text{track}}^i}{\text{pad}_y^i} \right)^2 \right\}, \quad (4.2)$$

where the index i runs over the stations containing hits within the FoI, $(x_{\text{closest}}^i, y_{\text{closest}}^i)$ are the coordinates of the closest hit to the track extrapolation point for each station, denoted by $(x_{\text{track}}^i, y_{\text{track}}^i)$, and $\text{pad}_{x,y}^i$ is half of the pad size in the x, y direction. Finally, N correspond to the total number of stations containing hits within their FoI.

The likelihoods¹ are computed as the cumulative probability distributions of D^2 , taking into account the narrower distribution close to zero for true muons than for the other particles erroneously selected by IsMuon. The D^2 distribution for muons is influenced by multiple scattering, therefore it depends on the momentum p and the polar angle θ of the analysed sample. To avoid any dependance of the muon likelihood on the calibration sample, the tuning is performed in bins of momentum and detector regions. For what concerns the non-muon hypothesis, the likelihood is calibrated with the D^2 distribution for protons, since the other charged hadrons present a component due to decays in flight that make their distribution very similar to that of true muons. For the protons, hits found in the muon system can be due to shower punch-through. This effect presents a momentum dependence, although less important than in muons, hence the tuning of the non-muon likelihood is performed separately for the four detector regions, due to their different granularity.

¹Since they will be described in detail later, their treatment will be omitted here.

The likelihood is defined, for each candidate, as the integral of the calibrated D^2 probability density function from 0 to the measured value D_0^2 . As already stated, the variable muDLL corresponds to the logarithm of the ratio between the muon and non-muon hypotheses.

4.1.3 Combined likelihood

Muon identification performance obtained with information from muon system can be improved combining these muon and non-muon likelihoods with the likelihoods from the RICH system and the calorimeter system. A combined log-likelihood is obtained for each track and for each of the different mass hypotheses by summing the logarithms of the likelihoods obtained using the three sources. The non-muon likelihood obtained in the muon system is assigned to the electron, pion, kaon and proton hypotheses. The difference in the combined log-likelihoods for the muon and pion hypotheses (that is the variable DLL) is then used to identify the muons.

4.1.4 Hits sharing as a discriminating variable

The same hit can be used to build multiple tracks. Reducing the number of tracks sharing hits is considered to be a way to reduce the misidentification probability. Tracks passing the IsMuon criterion are classified on the basis of a variable named NShared. If more than one track uses the same hits, a score of +1 is added to the track to which the hit is more distant. Selecting muons with NShared = 0 has been shown to reduce the probability of incorrectly identified hadrons (as muons) due to nearby true muons in high multiplicity events.

4.2 Performance of the Muon Identification

The way to extract the performance of the muon identification procedure from data is to select signal (muons) and background (pion, proton, kaon) candidates from specific two body decays using kinematical cuts and, if necessary, improving the purity by using the *tag and probe* technique: particle requirements are applied to one track (tag) and the other (probe) is used to calculate the muon efficiency or the misidentification probability. The $J/\psi \rightarrow \mu^+\mu^-$ decay is an abundant source of muons. Amongst the requirements, in order to reduce the combinatorial background, one of the muons is

usually required be identified as a tag, while the other (probe) is only required to have $p_T > 0.8$ GeV/c. The proton sample is selected from the $\Lambda^0 \rightarrow p\pi^-$ decay, while pions and kaons derive from the $D^{*+} \rightarrow \pi^+ D^0 (\rightarrow K^- \pi^+)$ decay.

The efficiency of a generic muon identification requirement, $\varepsilon_{\text{muonID}}$, is evaluated starting from the relation:

$$\varepsilon_{\text{muonID}} = \frac{S_{\text{true}}}{S_{\text{true}} + S_{\text{false}}}, \quad (4.3)$$

where S_{true} and S_{false} are the number of signal events satisfying and not satisfying the muon identification requirement. The two numbers are extracted from data using

$$S_{\text{true,false}} = N_{\text{true,false}} - B_{\text{true,false}}. \quad (4.4)$$

$N_{\text{true,false}}$ are obtained by counting the number of J/ψ candidates with invariant mass lying within a window around the J/ψ mass; $B_{\text{true,false}}$, the number of background events within the same mass window, is computed by extrapolating to the signal window the mass fit done in the J/ψ sidebands. The same procedure applies for the proton misidentification, while for the kaon and the pion the Eq. 4.3 is still valid but $S_{\text{true,false}}$ and $B_{\text{true,false}}$ are extracted from a full fit of the signal and background shapes to the invariant mass distribution of the D^0 candidates.

The performances are evaluated for tracks extrapolated within the geometrical acceptance of the muon detector and are separately described for the different requirements in the following.

4.2.1 Performance of IsMuon selection

The performance of the binary selection IsMuon is evaluated on the basis of the efficiency of finding hits within the FoIs for tracks extrapolated to the muon system, ε_{IM} . Its trend as a function of the muon momentum, for different transverse momentum ranges, is shown in Fig. 4.1(a). ε_{IM} varies weakly with transverse momentum, and a drop of $\sim 2\%$ is visible at low p for the lowest p_T interval, due to tracks close to the inner limit of the geometrical acceptance. The average efficiency is measured to be $\varepsilon_{\text{IM}} = (98.13 \pm 0.04)\%$ for particles with $p > 3$ GeV/c and $p_T > 0.8$ GeV/c.

In Fig. 4.1, also the misidentification probabilities for protons $\mathcal{P}_{\text{IM}}(p \rightarrow \mu)$ (b), pions $\mathcal{P}_{\text{IM}}(\pi \rightarrow \mu)$ (c), and kaons $\mathcal{P}_{\text{IM}}(K \rightarrow \mu)$ (d), are reported. For all the three sources of background, \mathcal{P}_{IM} decrease with increasing transverse

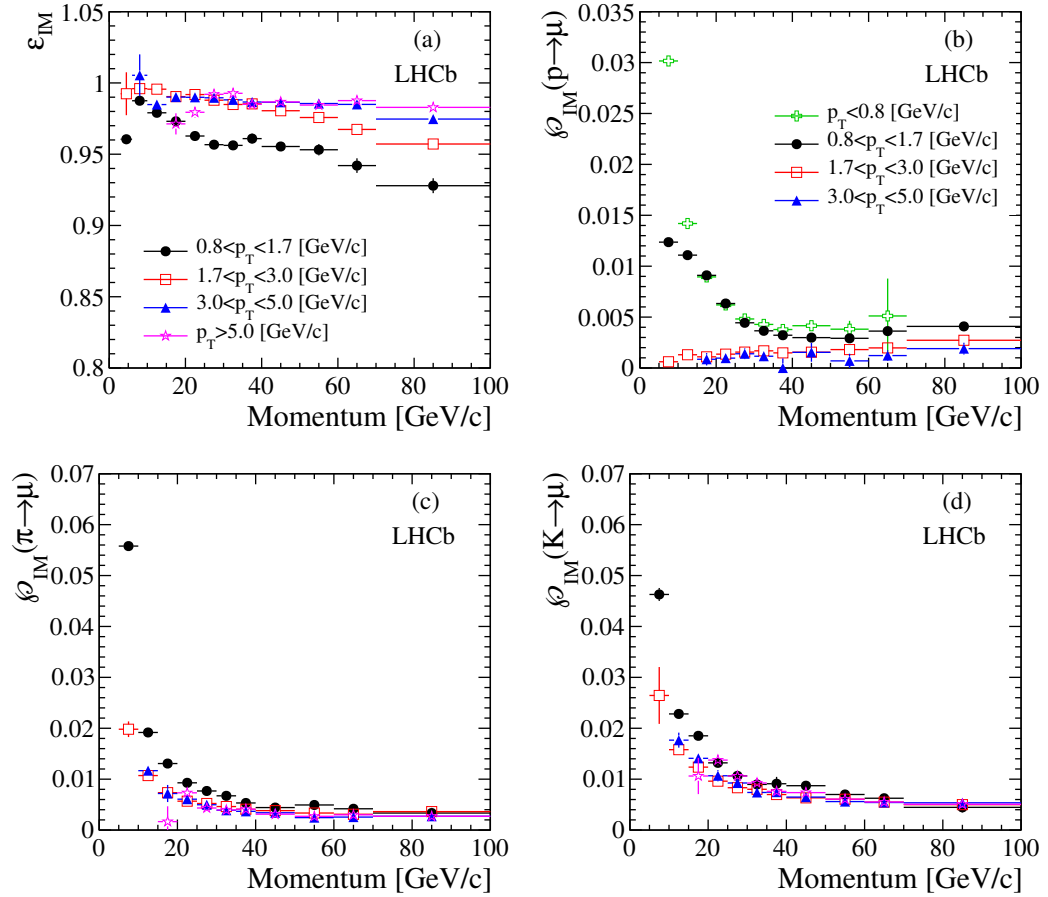


Figure 4.1: IsMuon efficiency ϵ_{IM} (a) and misidentification probability as a function of momentum in ranges of transverse momentum for protons $\mathcal{P}_{\text{IM}}(p \rightarrow \mu)$ (b), pions $\mathcal{P}_{\text{IM}}(\pi \rightarrow \mu)$ (c), and kaons $\mathcal{P}_{\text{IM}}(K \rightarrow \mu)$ (d).

momentum, as expected from the fact that tracks with higher p_T traverse the muon system in more external regions, which have lower occupancy. The misidentification probability drops with momentum (only in the lowest p_T ranges for the protons) reaching a *plateau* at about 40 GeV/c.

At low momentum, the misidentification probability lies within 0.1–1.3% for protons, while for the kaon and pions the values are within 0.6–4.5% and 0.2–5.6% respectively. This discrepancy arises from the fact that, for pions and kaons, decays in flight are the dominant source of misidentification probability at low momentum. For particles with $p > 3$ GeV/c, the average values for the misidentification probabilities are $\mathcal{P}_{\text{IM}}(p \rightarrow \mu) = (1.033 \pm 0.003)\%$, $\mathcal{P}_{\text{IM}}(\pi \rightarrow \mu) = (1.025 \pm 0.003)\%$, and $\mathcal{P}_{\text{IM}}(K \rightarrow \mu) = (1.111 \pm 0.003)\%$, evaluated in the whole p_T spectrum.

4.2.2 Performance of muon likelihoods

Figure 4.2 shows the performance of the muon identification efficiency, $\varepsilon_{\text{muDLL}}$, and of the misidentification probabilities as a function of the selection cut muDLL, for different momentum ranges. All the values are to be intended *given IsMuon*, hence the curves start at the probability corresponding to the IsMuon requirement.

When taking into account large momentum tracks ($p > 10$ GeV/c), the muon efficiency does not vary as a function of momentum up to muDLL ~ 2 , while the misidentification probabilities show a strong momentum dependence in the whole p spectrum. For this reason, in order to achieve a misidentification probability independent from the momentum, the muDLL cut must depend on p .

4.2.3 Performance of combined selection

The most used particle identification requirement after the application of IsMuon selection is the DLL, which enriches the information of the variable muDLL including data from the RICH and the calorimeter. The choice for the cut value must be a compromise between the purity of the signal and the efficiency needed for the specific application. The DLL has been shown to be more effective than muDLL in the discrimination power of muons from pions and kaons, as can be seen in Fig. 4.3, which compares the efficiency as a function of pion and kaon misidentification probability for both DLL and muDLL.

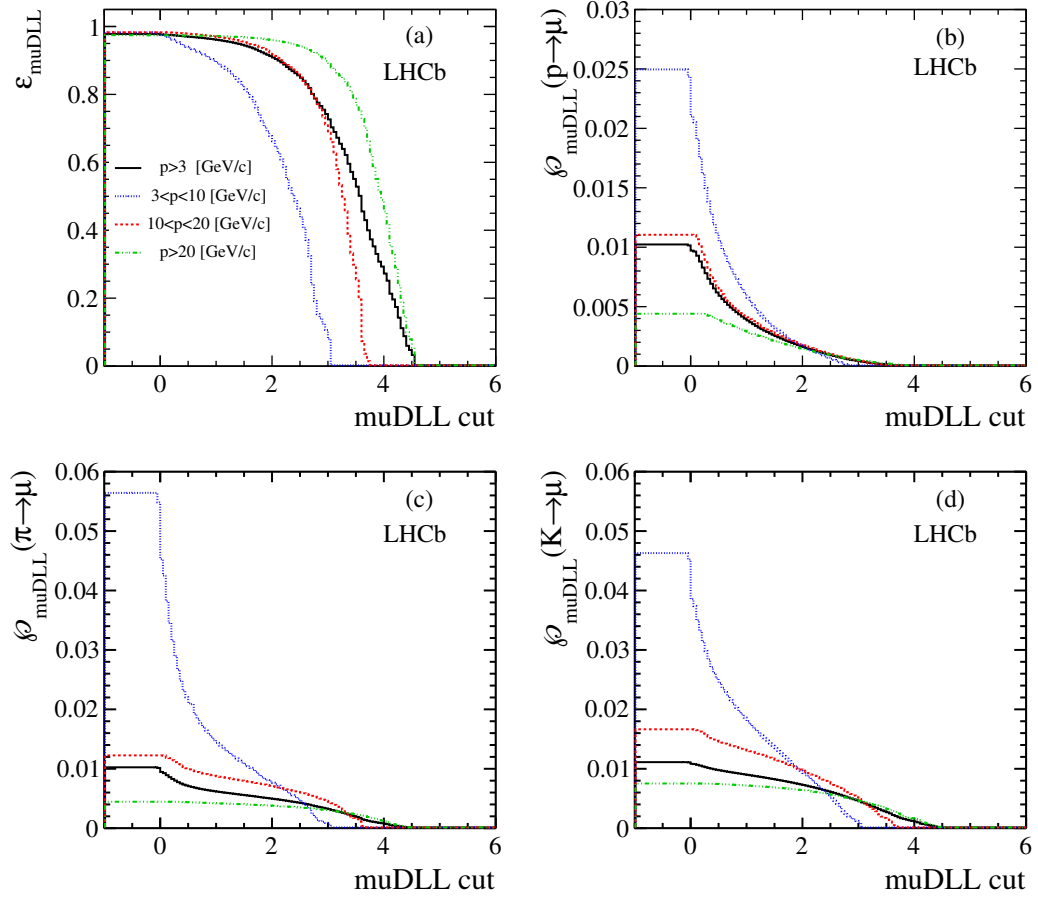


Figure 4.2: The muDLL efficiency ϵ_{muDLL} , for muons (a) and the misidentification probability for protons (b), pions (c), and kaons (d) as a function of the muDLL cut in ranges of particle momentum.

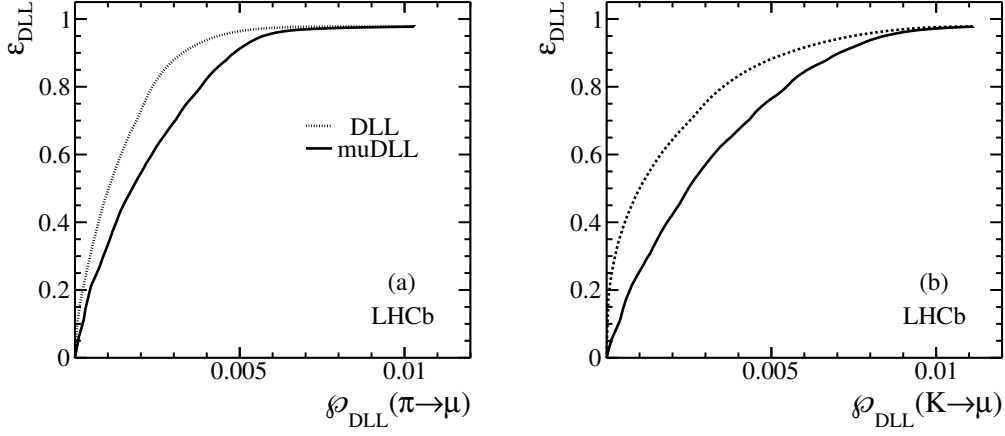


Figure 4.3: Average efficiency ε_{DLL} as a function of the pion (a) and kaon (b) misidentification probabilities for particles with $p > 3$ GeV/c.

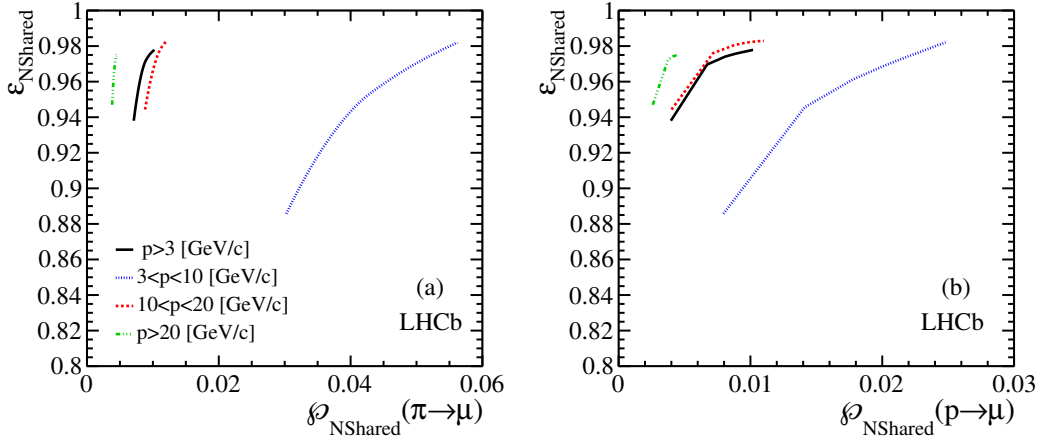
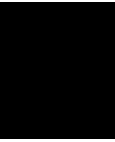


Figure 4.4: The muon efficiency $\varepsilon_{\text{NShared}}$ as a function of the pion (a) and proton (b) misidentification probabilities.

4.2.4 Performance based on hits sharing

As already mentioned, an effective way to reduce the incorrect identification of hadrons and muons at high occupancy is to introduce a cut in the variable NShared. In Fig. 4.4 the muon efficiency as a function of the misidentification probability for corresponding NShared cut is reported, both for pions and protons (kaons behave as pions due to similar decay-in-flight pollution at low

momentum), showing how `NShared` is particularly effective at low momenta, where the FoI size is bigger (see Eq. 4.1).



A novel muon identification algorithm

As already mentioned in Ch. 4, misidentification of charged mesons, in particular of pions, has an almost irreducible component attributed to decays in flight, together with a combinatorial component that is relevant especially when $p < 10$ GeV/c.

The currently used muon identification algorithm was conceived in a low-occupancy scenario, and for this reason it was optimised to maximise the efficiency, without considering mandatory to fight the combinatorial background, which was expected to be substantially negligible. Contrary to expectations, the luminosity of the first years of data taking was already higher than foreseen causing the background to be higher than expected, and the situation will become even more difficult during Run III. In this way the necessity to suppress the combinatorial background more effectively independently from the detector occupancy, and to develop algorithms more tolerant to station inefficiencies arises.

5.1 The new algorithm

The muon identification in LHCb can be improved rethinking the discriminating variable D^2 in order to include information from the multiple scattering experienced by muons and other particles while travelling through

matter, which can introduce correlations between the hits in the muon system.

The new variable can be expressed in general terms as

$$\chi_{\text{COR}}^2 = \delta \vec{x}^T \mathbf{V}^{-1} \delta \vec{x} \quad (5.1)$$

where $\delta \vec{x}$ is the distance in the x and y directions between the track extrapolation to each of the M2–M5 muon stations and the hit position in the corresponding station, weighted by the covariance matrix, \mathbf{V} . The covariance matrix is the sum of two contributions:

$$\text{Var}_{jj}^{\text{RES}} = \sigma_{\text{RES},j}^2, \quad (5.2)$$

a diagonal matrix taking into account the pad resolution, and

$$\text{Var}_{jk}^{\text{MS}} = \sum_{z_i < z_j, z_k} (z_j - z_i)(z_k - z_i) \sigma_{\text{MS},i}^2, \quad (5.3)$$

which accounts for the error introduced by the multiple scattering. As a consequence of the multiple scattering, the *true* trajectory of a particle can be tilted so that the corresponding hits on the muon system are not always the *closest* ones to the extrapolation of the track. Therefore the hit combination with the best value for the χ_{COR}^2 does not always coincide with the combination of hits that are closest to the extrapolated track. This concept can be clarified by looking at Fig. 5.1, showing several hits leaved by particles traversing the muon system and indicated by X. When there is more than one hit on the same station (M3, M5 in the example), the bottom one is drawn to be the closer one to the extrapolated track, which is represented as a dotted line. An algorithm selecting the closest hits to the track extrapolation would always choose the option A, while the χ_{COR}^2 would choose the option B.

While the choice of the combination can be straightforward when the mean number of hits within the FoI is $\lesssim 1$, this can become more ambiguous after the upgrade, when the occupancy in the muon chambers and so the mean number of hits within the FoIs, $N(M)$, will increase. In this situation, the evaluation of the discriminating variable for each of the combination of hits that allows to find the one with the best χ_{COR}^2 could be too slow to be feasible. For this reason it has been decided to limit the search to the five best matches in every station, so that the number of combination is:

$$N(M2) \times N(M3) \times N(M4) \times N(M5) \leq 5^4. \quad (5.4)$$

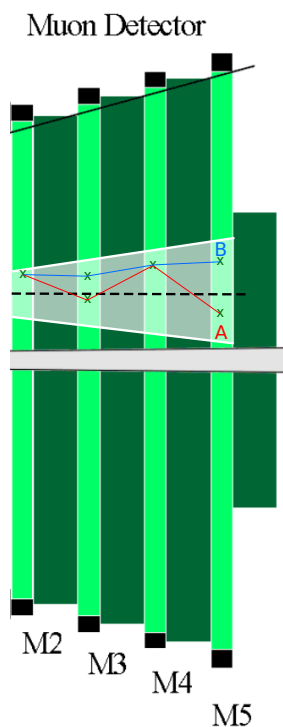


Figure 5.1: Illustration of the two possible track reconstructions from the hits X in the Muon Station for an algorithm that always chooses the hits closest to the extrapolated track (A) and for the χ^2_{COR} algorithm (B).

A brief explanation for the contributions to the covariance matrix is given in the following.

5.1.1 Multiple scattering through small angles

Particles travelling through the detector undergo the influence of the material composing it, which has random effects to be taken into account, *e.g.* the multiple scattering, some of them that can be studied in a deterministic way, *e.g.* the energy loss and the mean multiple scattering.

Multiple Coulomb scattering deflects charged particles by many small-angle scatters, causing a relatively small but random change of the direction of flight, whose distribution can be considered in a good approximation Gaussian for small deflection angles, applying the central limit theorem of statistics to a large number of independent scattering events. Defining [3]:

MS contribution	z position (m)	z/X ₀
ECAL+SPD+PS	12.8	28
HCAL	14.3	53
M23 filter	15.8	47.5
M34 filter	17.1	47.5
M45 filter	18.3	47.5

Table 5.1: Position and thickness in units of radiation length for the scattering media contributing to the multiple scattering encountered by particles traversing the muon system.

$$\theta_0 = \theta_{\text{plane}}^{\text{rms}} = \frac{1}{\sqrt{2}} \theta_{\text{space}}^{\text{rms}} \quad (5.5)$$

and using the Gaussian approximation for the angular distribution, the deflection angle can be written as:

$$\theta_0 = \frac{13.6\text{MeV}}{\beta c p} z \sqrt{x/X_0} [1 + 0.038 \ln(x/X_0)] \approx \frac{13.6\text{MeV}}{\beta c p} z \sqrt{x/X_0} \quad (5.6)$$

where p , βc and z are the momentum, the velocity and the charge of the incident particle, and x/X_0 is the thickness of the scattering medium in units of radiation length.

Multiple Coulomb scattering produces errors correlated from one layer to the next, *i.e.* the proper error matrix described in 5.3 is non-diagonal. The $\sigma_{\text{MS},i}$ corresponds to θ_0 ; the position along the z axis and the thickness in units of radiation length for the considered scattering centers are summarised in Table 5.1.

5.1.2 Chamber resolution

All the muon stations involved in the muon identification procedure entirely consist of Multi-Wire Proportional Chambers, which allow the localisation of ionising particles crossing the active area of the detector by collecting the charge of the cascades of ionisation (avalanches). Assuming that the avalanche gives rise to only one pulse on the pad nearest to the trajectory in the i -th chamber, the errors ε_i can be assumed to have the following normalised distribution:

$$P(\varepsilon_i) = 0 \quad \text{for } |\varepsilon| > d_i/2 \quad (5.7)$$

$$P(\varepsilon_i) = 1/d_i \quad \text{for } |\varepsilon| < d_i/2 \quad (5.8)$$

where d is the pad size along the considered x or y direction. The corresponding RMS chamber error, $\sigma_{\text{MS},i}$ in 5.2, is then

$$\sigma_{\text{MS},i} = \sqrt{V(\varepsilon_i^2)} = \left[1/d_i \cdot \int_{-d_i/2}^{+d_i/2} \varepsilon^2 \cdot d\varepsilon \right]^{1/2} = d_i/\sqrt{12}. \quad (5.9)$$

5.2 Test on Monte Carlo for the upgrade

As a first approach, the new algorithm has been tested on a Monte Carlo for the upgrade, so to study the effect of the correlation terms in the covariance matrix of the χ_{COR}^2 in a situation of high occupancy of the muon system. For this purpose it has been necessary to

- implement a “tuned” Monte Carlo, since the official LHCb Monte Carlo for the upgrade does not reproduce correctly the effect of the presence of the cavern and the accelerator (and therefore their interactions with particles), and the low energy background;
- develop a tool that emulates the digitisation process therefore allowing to study various parameters of interest (particle fluxes, flux of “ghost” particles, occupancies, muon ID, ...).

This study has been conducted on a simulated sample of $J/\psi \rightarrow \mu^+\mu^-$ generated using PYTHIA 8 [32] produced at an instantaneous luminosity of $\mathcal{L} = 2 \cdot 10^3 \text{ cm}^{-2} \text{ s}^{-1}$ and at a centre-of-mass energy of $\sqrt{s} = 14 \text{ TeV}$, with low production and tracking thresholds for electrons and photons (10 keV instead of 30 keV), which includes the geometry of the surroundings of the detector together with an updated description of the beampipe shielding. The tool performs the muon identification procedure from scratch, selecting all the particles generated inside a cylinder with radius 3 mm and length in z 500 mm centered in the interaction point, extrapolating the tracks to center of the magnet where a p_T kick is applied to take into account the effect of the magnetic field; the tracks are then extrapolated in the muon system and finally hits are searched in the muon stations within the Field of Interest;

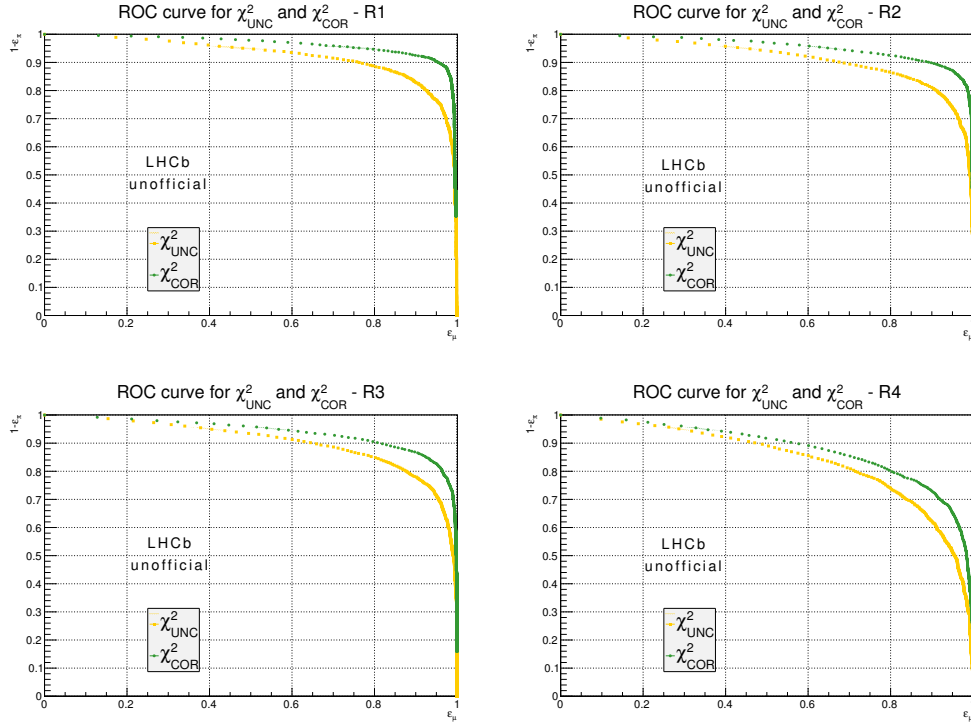


Figure 5.2: ROC curves comparing the performances of the χ^2 algorithm with (χ^2_{COR}) and without (χ^2_{UNC}) the inclusion of the multiple scattering terms in the error matrix separately for the different regions of the muon system.

at this point IsMuon selection is applied in the usual way followed by the application of the new algorithm.

The plots in Fig. 5.2 show the pion rejection efficiency as a function of the efficiency for true muons separately for each region of the muon system. The comparison of the two ROC (Receiver Operating Characteristic) curves shows how taking into account the off-diagonal terms in the covariance matrix of the errors, due to the multiple scattering, improves the muon identification quality. The D^2 variable is expected to behave like χ^2_{UNC} and this encourages the use of the χ^2_{COR} to improve the current procedure for the muon identification.

5.3 Validation on data

The promising results obtained for the χ_{COR}^2 on the Monte Carlo for the upgrade have encouraged to test the tool on real data, thus the algorithm has been included as an official tool available to LHCb users for offline studies.

5.3.1 The $K_S^0 \rightarrow \mu^+ \mu^-$ case

In the context of the search for the $K_S^0 \rightarrow \mu^+ \mu^-$ performed with the Run I data [47], a dedicated MVA classifier (see Appx. A for a detailed description) that uses the χ_{COR}^2 and that includes additional information from the muon detector that is not used in the standard muon identification procedure has been developed, *i.e.*:

- a Match variable that represents the “quality” of the muon hits, considering that hits having only one detector view, in the x or in the y direction, are usually due to noise or spillover. No distinction between 1-view and 2-view hits is made in the D^2 variable. In this case, the variable has value 0 if nothing is found, 1 if the hit is 1-view only and 2 if the hits has both x and y ;
- a Match Distance, representing the distribution of bidimensional residuals expressed in number of σ ;
- an Isolation variable that takes into account the distance in number of σ between the best hit and the closest track extrapolation (in the currently used version the isolation is only taken into account through the NShared variable);
- information on Timing and Cluster Size, since out-of-time hits and large clusters are usually due to background hits.

The procedure has also been modified as follows:

- all good quality long tracks with a momentum above the threshold of 3 GeV/c are extrapolated to the muon stations. The field of interest is defined starting from the distance between the track extrapolation and the muon hit position taking into account the uncertainty on the extrapolation and the resolution of the muon detector:

$$\sigma_{x,y} = \sigma_{x,y}^{\text{extr}} \oplus \text{padsiz}_{e_{x,y}} / \sqrt{12}. \quad (5.10)$$

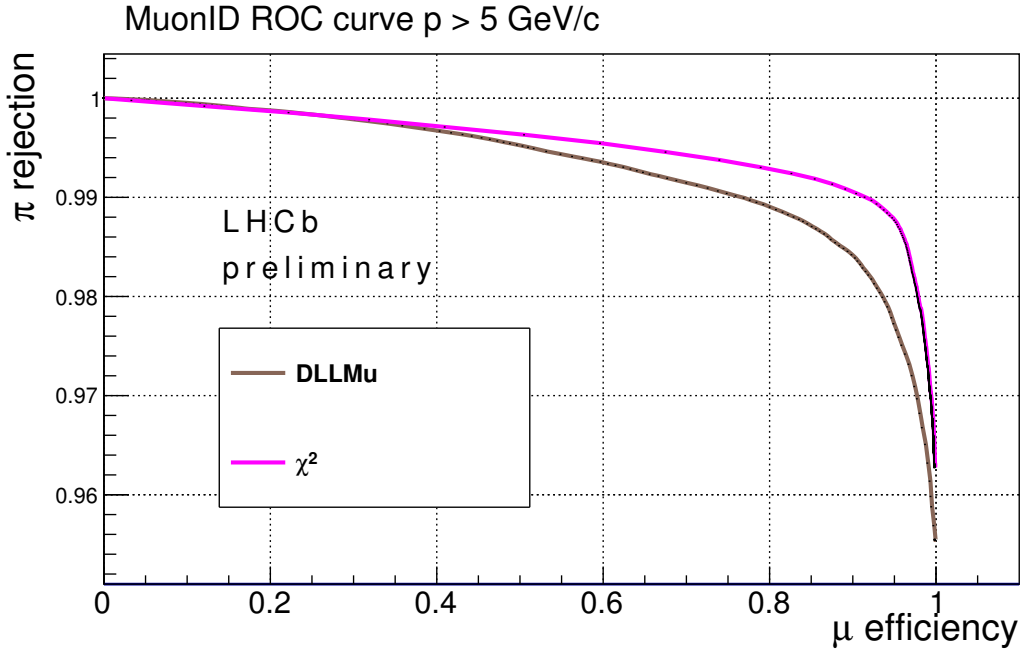


Figure 5.3: ROC curves for muon identification based on IsMuon and a cut in the variable muonDLL (DLLMu) or the χ^2_{COR} (χ^2) for tracks with $p > 5 \text{ GeV}/c$.

A search window of 8σ is used for both x and y . All hits within this window are retained;

- for each extrapolated track, the best hit per station is chosen between the closest five matches in every station. For each combination of hits, the χ^2_{COR} is computed to choose the best set of hits;
- as a first try, only “high-quality” hits (Match variable value = 2, cluster size < 10) are used; lower-quality hits are only used if high-quality ones are not found;

The algorithm has been tested using full-DST data samples of $K_S \rightarrow \pi^+\pi^-$ to have a fully unbiased sample of pions, and of $B^+ \rightarrow J/\psi K^+$ to have a low- p_T sample of muons, which are selected with tag and probe method. Both samples are obtained from data collected by LHCb at a centre-of-mass energy of $\sqrt{s} = 8 \text{ TeV}$ during 2012. The second sample is reweighted to have the same distributions as $K_S \rightarrow \pi^+\pi^-$ for the variables p , p_T , and N_{tracks} ,

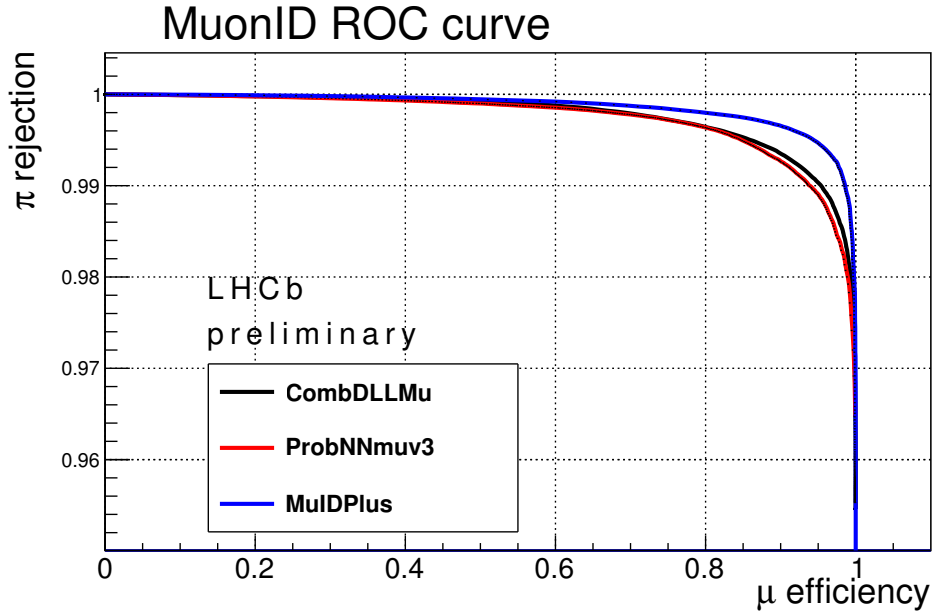


Figure 5.4: ROC curves for muon identification based on the different classifiers described in the legend.

which are strongly correlated with the detector response but are not used as discriminating variables.

The pion sample is obtained from stripping line `KS02MuMuNoMuID` applying detachment and quality cuts on the K_S vertex, and for a kaon mass window between 492 and 504 MeV/c^2 . The pion tracks must be TIS at all levels. After this selection the sample contains $1.24 \cdot 10^6$ tracks. The muon sample is obtained from the stripping line `Bs2MuMuLinesBu2JpsiK` with detachment and quality cuts on the B vertex. Only B candidates with mass $5250 < m_B < 5320 \text{ MeV}/c^2$ and J/ψ candidates within $3070 < m_{J/\psi} < 3130 \text{ MeV}/c^2$ are retained. The tag tracks are required to have $\text{ProbNNv3} > 0.3$ while probe tracks must be TIS at all levels. The resulting sample contains $530 \cdot 10^3$ candidates. The used sample is biased by the `IsMuon` requirement at stripping level, hence the results obtained for the muon efficiency are to be intended as relative to `IsMuon == 1`. The discriminating power of this new method is compared to the standard DLL on Fig. 5.3 that shows how the misID probability for 90% muon efficiency increases of approximately 1% just using the variable that includes the information from the correlations among the muon stations.

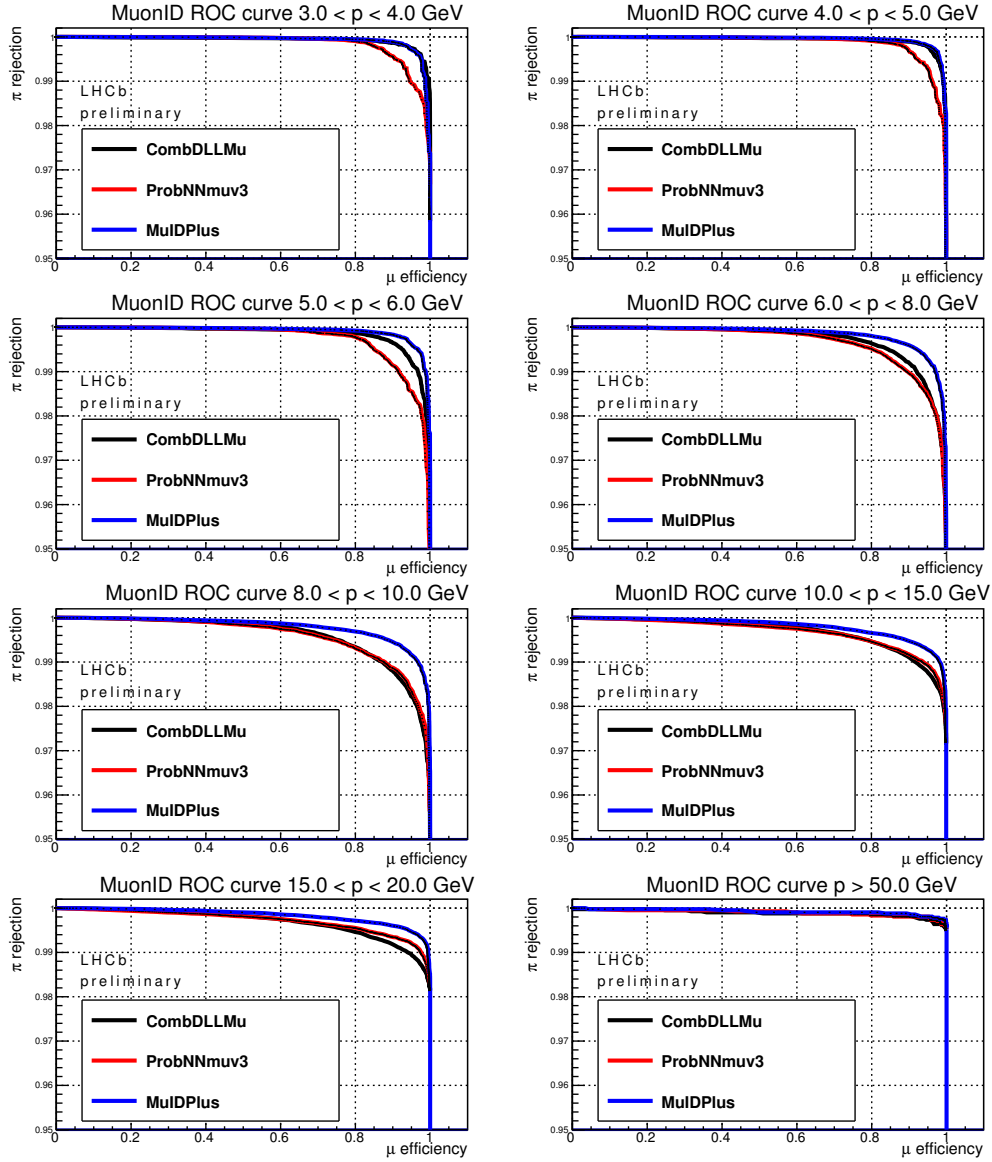


Figure 5.5: ROC curves for muon identification based on the classifiers described in the legends for different momentum bins.

The final classifier, MuIDPlus, is then obtained training a Boosted Decision Tree (BDT) on the 21 muon detector variables, in addition to variables from the tracker, the RICHs and the CALOs that are relevant for muon identification. The BDT is trained on half of the calibration samples, and the performances are checked using the other half of the sample. The resulting ROC curve is compared to the ones of the CombDLL and of the latest tune of ProbNN classifiers in Fig. 5.4. The same curves are compared for different momentum bins in Fig. 5.5, showing how the MuIDPlus classifier performances are always equivalent (at low momentum) or even better than CombDLL and always better than ProbNN.

For the same classifiers, the pion misidentification probability evaluated for 90% muon efficiency is reported in Fig. 5.6. The new classifier is capable to reduce the misID probability of a factor $\gtrsim 2$ with respect to the others (Fig. 5.6 (a)) and its performances are more stable when the track multiplicity increases (Fig. 5.6 (b)).

5.3.2 The $J/\psi \rightarrow \mu^+\mu^-$ case

The previous subsection showed how the BDT that includes the new χ_{COR}^2 improves the muon identification performances and reduces the misidentification probability when applied to the study of the $K_S^0 \rightarrow \mu^+\mu^-$ decay. However, this decay is characterised by a soft p_T spectrum of the daughter muons. Thus it becomes important to extend the study in order to see whether the observed improvement in the performance is reproduced when the method is applied to other physics channels with different muon kinematic spectra. The performance of the muon identification has thus been studied on muons from $J/\psi \rightarrow \mu^+\mu^-$ decays, using the $D^0 \rightarrow K^-\pi^+$ decay, with the D^0 selected from $D^{*+} \rightarrow D^0\pi^+$, as a sample of pions for the misidentification.

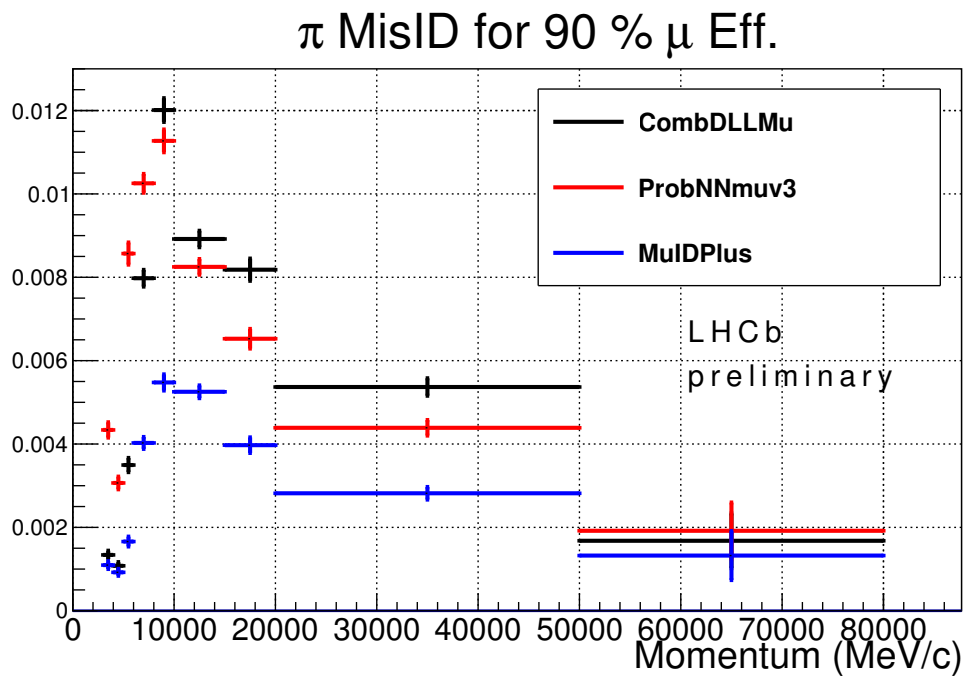
This study uses the BDT grown on the data samples used for the analysis of the decay $K_S^0 \rightarrow \mu^+\mu^-$. For this reason it is fundamental to stress that the results shown in this context are relative to the test of the BDT on a sample having kinematic features (the muon transverse momentum distribution, in particular) that are different from those of the training sample. This implies that the classifier is not optimised for the examined case, with the consequence of introducing a detrimental bias on the performances shown by MuIDPlus, which will result in the attenuation (or even a concealing) of the eventual improvement with respect to the currently used algorithm.

The analysed data sample is obtained using the data collected during 2012, with a magnetic field with negative polarity. The reconstruction has been done in the Reco14 framework and the stripping used is Stripping21r1p1a for 2011 and Stripping21r0p1a for 2012, which include the additional variables required for this study. The selection criteria are different for the signal and for the background. The mass window for the $D^{*+} \rightarrow D^0\pi^+$ decay is $(m_{D^*} - m_{D^0}) \in [144.5, 146.5] \text{ MeV}/c^2$. The pion from the D^0 is required to be in acceptance and must not have triggered the event at L0 nor at Hlt1. It also has to pass IsMuon selection. For the kaon, a request on the confidence that the track is actually due to a kaon is made (`ProbNnk > 10`).

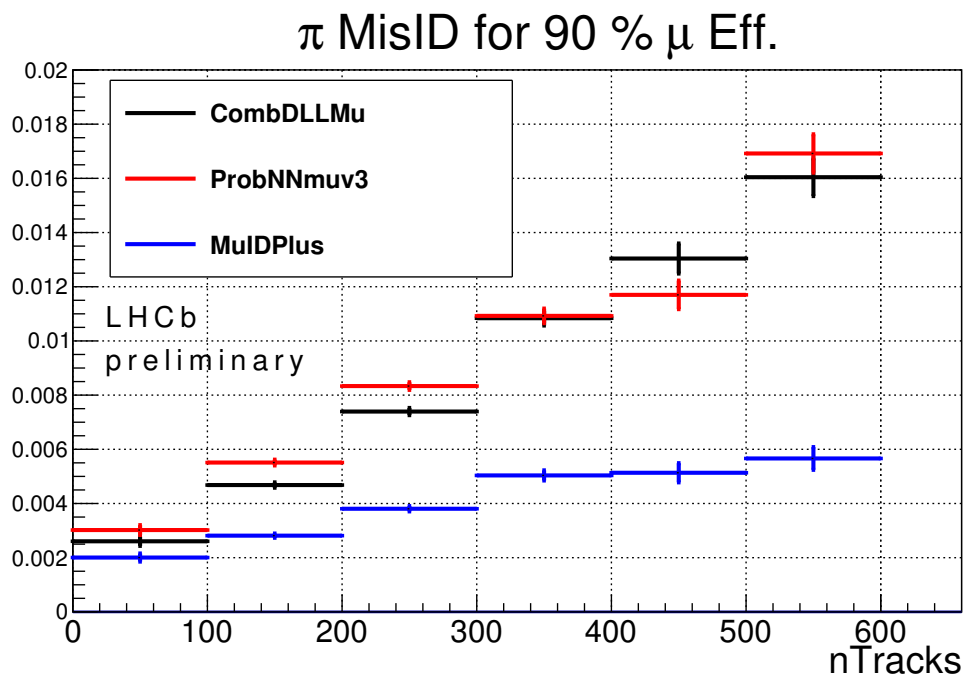
For the muon selection from the $J/\psi \rightarrow \mu^+\mu^-$ decay, the tag and probe method is applied. In order to be identified as the tag muon, a particle must have $p > 6 \text{ MeV}/c$ and $p_T > 1.5 \text{ MeV}/c$, be in acceptance and satisfy IsMuon requirement. The window for the dimuon mass is $m_{\mu\mu} \in [2.9, 3.3] \text{ MeV}/c^2$. The probe muon particle is required to be TIS at all levels to ensure that the sample is unbiased. In addition to this it only has to be in acceptance and to satisfy the IsMuon requirement.

The ROC curve for the MuIDPlus BDT is compared to that of the ProbN-Nmuv3 and CombDLL classifiers in Fig. 5.7. This study confirms that MuID-Plus has always better performances than ProbNN, although the expected improvement with respect to CombDLL is not reproduced. The tuning of the BDT on a sample which is sensibly different from the one it is applied has surely played a role in the observed behaviour, thus the performances are expected to improve considerably after the tuning of the BDT on an analogous sample.

The same curves are shown in Fig. 5.8 in bins of p and in Fig. 5.9 in bins of $Ntracks$. The behaviour observed in the integrated plot is reproduced in all the different bins of momentum and multiplicity.



(a)



(b)

Figure 5.6: Pion misidentification probability for 90% muon efficiency for the classifiers described in the legend as a function of momentum (a) and of the number of tracks (b).

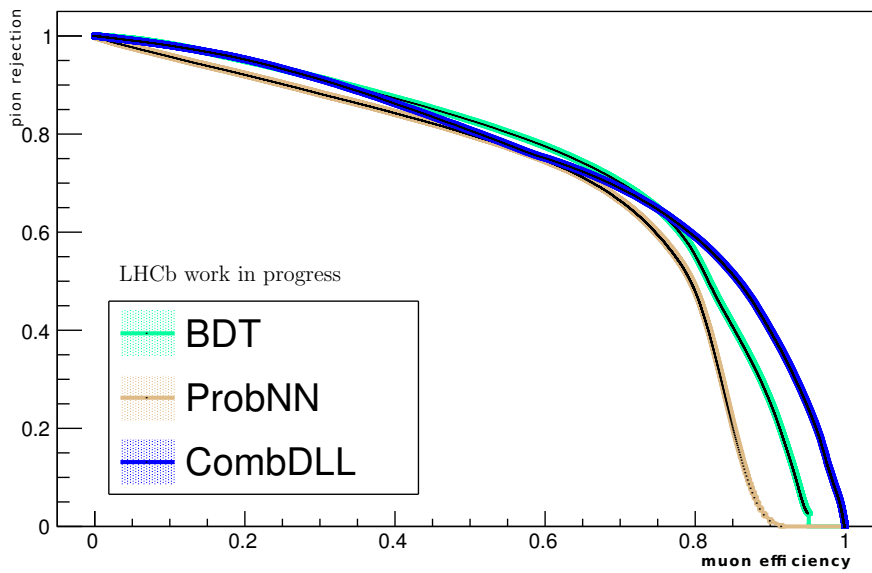


Figure 5.7: ROC curves for muon identification based on the different classifiers described in the legend.

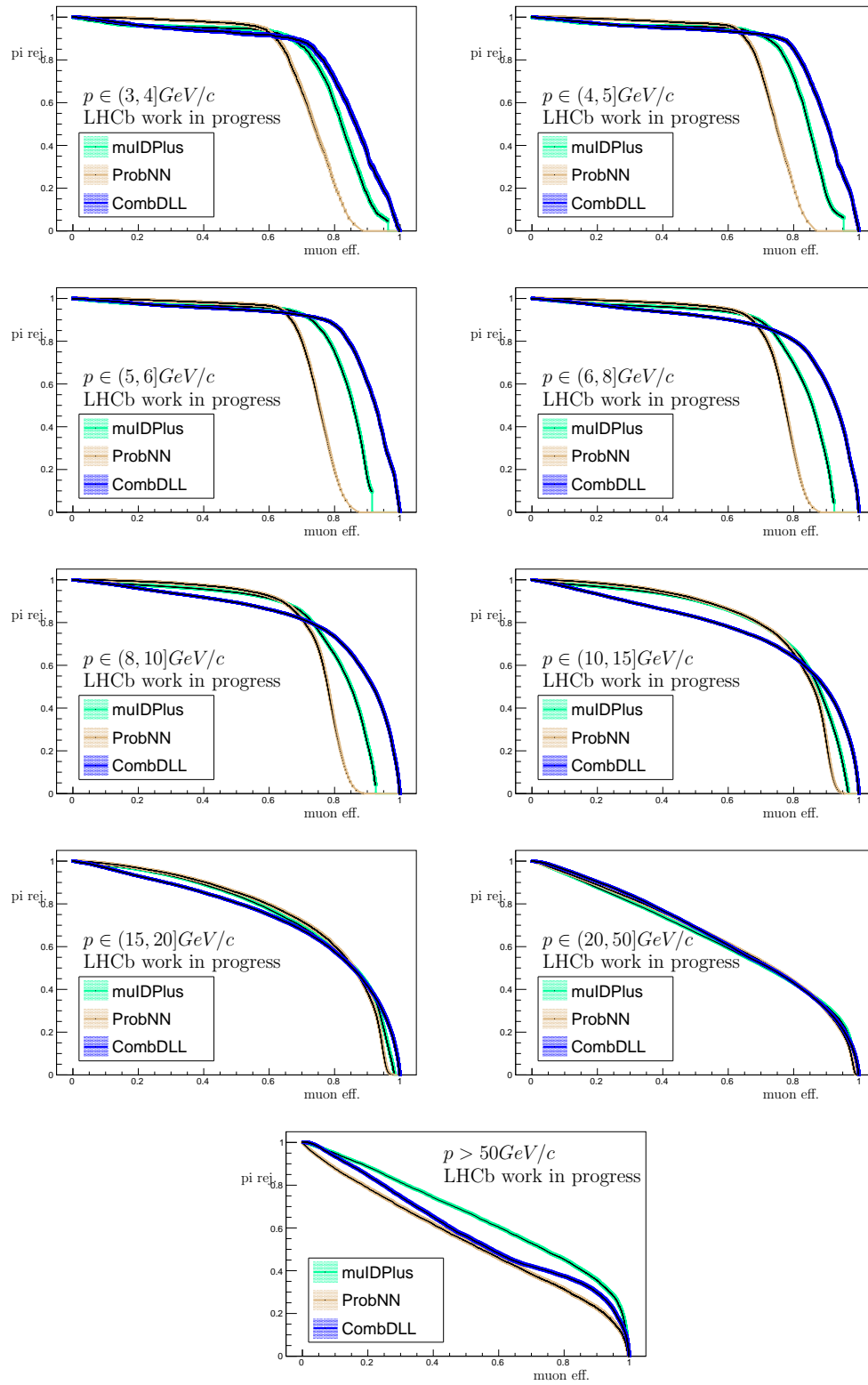


Figure 5.8: Pion rejection as a function of muon identification efficiency for the classifiers described in the legends for different momentum bins.

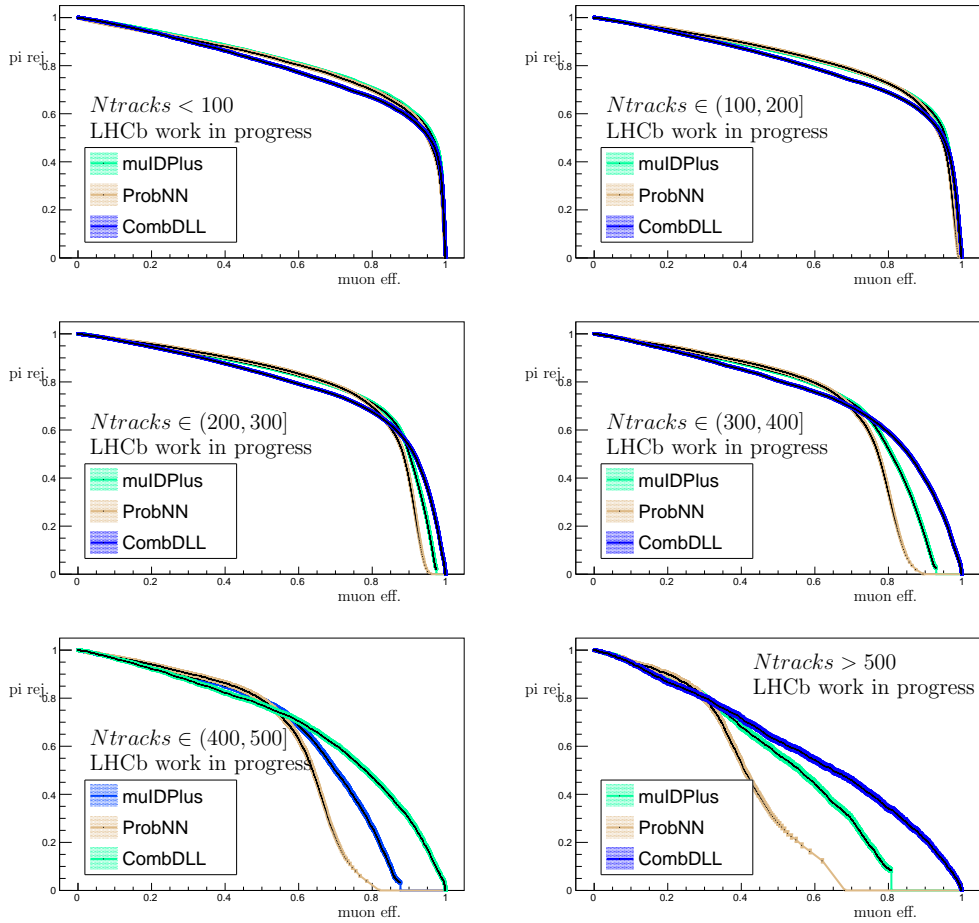


Figure 5.9: Pion rejection as a function of muon identification efficiency for the classifiers described in the legends for different multiplicity bins.

The $D^0 \rightarrow \mu^+ \mu^-$ decay case

The LHCb experiment has set the upper limit for the branching fraction of the rare $D^0 \rightarrow \mu^+ \mu^-$ decay to $\mathcal{B}(D^0 \rightarrow \mu^+ \mu^-) < 6.2(7.6) \cdot 10^{-9}$ at 90% CL (95% CL) [17], thus two orders of magnitude are still to be explored before reaching the sensitivity of the theoretical prediction.

The search for the $D^0 \rightarrow \mu^+ \mu^-$ decay starts from the study of the decay $D^{*+} \rightarrow D^0(\rightarrow \mu^+ \mu^-)\pi^+$ (and of its charge conjugate), with the D^{*+} directly produced in pp collisions. Because of the presence of two muons in the final state, this represents the typical decay that would benefit from an improvement of the muon identification techniques. Indeed, because of the analogous topology to the signal and of the similarity of the pion and the muon masses, the $D^{*+} \rightarrow D^0(\rightarrow \pi^+ \pi^-)\pi^+$ decay can significantly contribute to the peaking background in both the dimuon and the $m(\pi\mu\mu) - m(\mu\mu)$ mass distributions around the D^0 mass and the $D^* - D^0$ mass difference, respectively, when both pions are misidentified as muons. This implies that the background due to $D^0 \rightarrow \pi^+ \pi^-$ events cannot be eliminated by a side-band subtraction, instead it requires an appropriate application of misidentification-probability knowledge. Also other two-body hadronic decays of the D^0 contribute to the background when both the decay products are misidentified as muons, with a greater branching ratio compared to $D^0 \rightarrow \pi^+ \pi^-$, as summarised in Table 6.1. Nevertheless, in these other channels there is a large mass difference between the misidentified kaon and a real muon that shifts most of these events out of the D^0 mass window.

An additional source of background that has to be rejected is due to the random combination of two real muons. This contribution, called *combina-*

Decay	Branching fraction
$D^0 \rightarrow K^-\pi^+$	$(3.93 \pm 0.04)\%$
$D^0 \rightarrow K^+K^-$	$(4.01 \pm 0.07) \cdot 10^{-3}$
$D^0 \rightarrow \pi^+\pi^-$	$(1.421 \pm 0.025) \cdot 10^{-3}$

Table 6.1: Branching fraction of the main hadronic two-body decays of the D^0 , which contribute to the background in the search for $D^0 \rightarrow \mu^+\mu^-$ decay [48].

torial background, has a smooth dependency on both the dimuon and the $m(\pi\mu\mu) - m(\mu\mu)$ invariant mass in the proximity of the D^0 mass and of the D^0 and $D^* - D^0$ mass difference, respectively.

As anticipated, $D^0 \rightarrow \mu^+\mu^-$ events are searched for in the decay channel $D^{*+} \rightarrow D^0(\rightarrow \mu^+\mu^-)\pi_s^+$. This method, which is usually referred to as *tagged*, allows to determine if the D meson is a D^0 or a \bar{D}^0 by measuring the charge of the pion. The Q-value for this process is low thus the pion is *soft* (*i.e.* it has low momentum, ~ 5 GeV/c) and this complicates the reconstruction; nevertheless the study of the complete decay chain $D^{*+} \rightarrow D^0(\rightarrow \mu^+\mu^-)\pi_s^+$ allows to suppress part of the background thanks to the additional information achievable from the D^{*+} . To avoid any bias while analysing the data, the region where the excess of decay events is expected is *blinded*, *i.e.* data in this region is removed and will be available only after the whole procedure will be completed and verified.

In the search for the $D^0 \rightarrow \mu^+\mu^-$, the branching fraction (or its upper limit, if no signal is observed) is obtained from the normalisation of the $D^{*+} \rightarrow D^0(\rightarrow \mu^+\mu^-)\pi^+$ to the $D^{*+} \rightarrow D^0(\rightarrow \pi^+\pi^-)\pi^+$ decay as:

$$\mathcal{B}(D^0 \rightarrow \mu^+\mu^-) = \frac{N_{D^{*+} \rightarrow D^0(\rightarrow \mu^+\mu^-)\pi^+}}{N_{D^{*+} \rightarrow D^0(\rightarrow \pi^+\pi^-)\pi^+}} \cdot \frac{\varepsilon_{\text{tot}(\pi\pi)}}{\varepsilon_{\text{tot}(\mu\mu)}} \cdot \mathcal{B}(D^0 \rightarrow \pi^+\pi^-) \quad (6.1)$$

$$= \alpha N_{D^{*+} \rightarrow D^0(\rightarrow \mu^+\mu^-)\pi^+}; \quad (6.2)$$

where α is the so-called *single events sensitivity*, that is the branching fraction that would correspond to the observation of a single signal event. The ratio of the efficiencies can be factorised as:

$$\frac{\varepsilon_{\text{tot}(\pi\pi)}}{\varepsilon_{\text{tot}(\mu\mu)}} = \frac{\varepsilon_{\text{sel}(\pi\pi)}}{\varepsilon_{\text{sel}(\mu\mu)}} \cdot \frac{\varepsilon_{\text{acc}(\pi\pi)} \cdot \varepsilon_{\text{rec/sel}(\pi\pi)} \cdot \varepsilon_{\text{trig}(\pi\pi)}}{\varepsilon_{\text{acc}(\mu\mu)} \cdot \varepsilon_{\text{rec/sel}(\mu\mu)} \cdot \varepsilon_{\text{trig}(\mu\mu)}} \quad (6.3)$$

where the right terms refer to the offline selection, detector acceptance, reconstruction and trigger efficiencies, respectively.

6.1 Data and Monte Carlo samples

The work here described is based on data collected in 2011 ($\sqrt{s} = 7$ TeV) and 2012 ($\sqrt{s} = 8$ TeV) in pp collisions at the LHCb detector, for an integrated luminosity of $\sim 1 \text{ fb}^{-1}$ and $\sim 2 \text{ fb}^{-1}$, respectively. The stripping version used are Stripping20r1p1a and Stripping21r0p1a respectively. For these productions, events were saved in MDST format including the additional variables required for this study.

The Monte Carlo samples have been generated with Sim08h, separately for the two years and the two magnet polarities, and the different decay lines can be summarised as in Table 6.2.

Decay channel	Gen. Events 2011		Gen. Events 2012	
	MU	MD	MU	MD
$D^{*+} \rightarrow D^0(\rightarrow \mu^+\mu^-)\pi^+$	525065	550169	1019997	1084183
$D^{*+} \rightarrow D^0(\rightarrow \pi^+\pi^-)\pi^+$	521240	455758	1065651	1030253
$D^{*+} \rightarrow D^0(\rightarrow \pi^+\pi^-)\pi^+$ as $\mu^+\mu^-$	1437	1526	4156	4125

Table 6.2: Monte Carlo generated events, divided per year and splitted by magnet polarity (magnet up, MU, and magnet down, MD). The last sample is stripping-filtered with the line for the signal channel.

6.2 Selection

The selection for the signal and control channels in data and Monte Carlo samples will be here presented, starting from the trigger strategy, describing the optimisation of the cuts, up to the final selection cuts.

6.2.1 Trigger studies

The signal channel $D^0 \rightarrow \mu^+\mu^-$ can be triggered by muon triggers both at L0 and Hlt1. At Hlt2 level dedicated lines were written (see Subsubsec. 6.2.1.1).

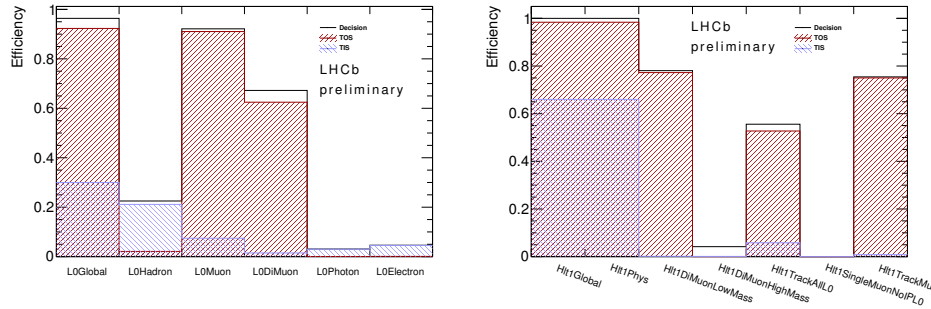


Figure 6.1: Efficiencies of trigger lines for offline-selected $D^0 \rightarrow \mu^+ \mu^-$ signal as obtained from MC. Efficiencies for TOS and TIS decisions are also shown. Hlt1 efficiencies are on top of L0 triggered events.

The trigger path at L0 and Hlt1 has been decided on the basis of Monte Carlo simulations.

Trigger path	Eff. (Dec)	Eff. (TOS)
L0Muon L0DiMuon	0.932411	0.920583
L0Muon L0DiMuon L0GlobalTIS	0.96236	0.961478
L0Muon L0DiMuon L0HadronTIS	0.957857	0.948759
Hlt1DiMuonLowMass Hlt1TrackMuon	0.884929	0.880395
Hlt1DiMuonLowMass Hlt1TrackMuon Hlt1TrackAll	0.905347	0.89475
Hlt1DiMuonLowMass Hlt1TrackMuon Hlt1Phys(TIS)	0.969814	0.968682
Hlt1DiMuonLowMass Hlt1TrackMuon Hlt1TrackAll Hlt1Phys(TIS)	0.973148	0.971964

Table 6.3: Trigger efficiencies for offline selected $D^0 \rightarrow \mu^+ \mu^-$ candidates in Monte Carlo. Hlt1 efficiencies are determined on top of L0 triggered events. Efficiencies are calculated for various lines as Dec (*i.e.* the event triggered the lines) or TOS (*i.e.* the $D^0 \rightarrow \mu^+ \mu^-$ decay triggered the lines); where TIS is indicated in parentheses the line is required to be triggered independently of the signal. The || symbol indicates the OR of the trigger lines.

The signal efficiencies for L0 and Hlt1 lines are shown in Fig. 6.1. At L0 most of the events are triggered by L0Muon and L0DiMuon lines but a non-negligible fraction of events can be recovered using the other triggers. In Table 6.3 the efficiencies for some combinations of triggers are shown, referred to preselected signal events.

At Hlt1 level most of the efficiency is given by Hlt1DiMuonLowMass, Hlt1TrackMuon, and Hlt1TrackAllL0 lines. In principle, part of the events are also triggered by Hlt1DiMuonHighMass line in which most probably one

of the signal muons and one random muon have been combined (as from Fig. 6.1 events are not TIS nor TOS).

In the MC all trigger lines, including the calibration ones, are not prescaled. As a consequence, global efficiencies at L0 and Hlt1 level are not reliable. In any case, a full TOS chain for the signal is required as the small additional statistics from considering TIS events would be washed out by a larger uncertainty for the TIS efficiency estimation: (L0Muon_TOS || L0DiMuon_TOS) && (Hlt1DiMuonLowMass_TOS || Hlt1TrackMuon_TOS || Hlt1 TrackAllL0_TOS).

The final efficiencies will be measured with a data-driven method on $J/\psi \rightarrow \mu^+\mu^-$ control channels.

6.2.1.1 Hlt2

Variable	Cut value
DOCA	< 0.1 mm
$\min(p_T(\mu))$	> 750 MeV/c
$\max(p_T(\mu))$	> 1100 MeV/c
$\min(p(\mu))$	5000 MeV/c
Track fit χ^2	< 5
$\min(\chi^2 IP(\mu))$ w.r.t. PV	< 3
$\max(\chi^2 IP(\mu))$ w.r.t. PV	< 8
χ_{FD}^2 of the D^0	> 20
$\cos(\text{Angle}(\vec{p}_{D^0}, \vec{r}_{PV} - \vec{r}_{DV}))$	> 0.9998
$p_T(D^0)$	> 1800 MeV/c
$\chi^2 IP(D^0)$ w.r.t. PV	< 15
D^0 vertex fit χ^2	< 10
D^0 mass window	± 70 MeV/c ²

Table 6.4: Summary of the cuts used in the HLT2 trigger for the $D^0 \rightarrow \mu^+\mu^-$ selection. Cuts referred to muons are also applied to kaons and pions for the $D^0 \rightarrow \pi^+\pi^-$ and $D^0 \rightarrow K^-\pi^+$ decays.

A dedicated set of lines was designed for Hlt2, selecting *untagged* two-body D^0 decays using exactly the same trigger cuts for both the signal and the control samples. The same lines were used for tagged and untagged D^0 decay selection. A common template for $D^0 \rightarrow x^+y^-$ decays was designed and the applied cuts for the selection are summarised in Table 6.4.

To match the rate retention requirements of Hlt2, a prescale was applied to some of the Hlt2 trigger lines, which was not constant over the time. For this reason the data is split into two periods, up to run 91556, corresponding to an integrated luminosity of 79 pb^{-1} , and after run 91556, corresponding to an integrated luminosity of 3 fb^{-1} after which the prescales on the Hlt2 lines were changed to a stable value. The values of the prescales used for the Hlt2 trigger lines used for this study are listed in Table 6.5.

Run number	Lumi	Hlt2Dst2PiD02Kpi	Hlt2Dst2PiD02pipi
> 91556	$\sim 79 \text{ pb}^{-1}$	0.002	0.006
< 91556	$\sim 3 \text{ fb}^{-1}$	0.01	0.03

Table 6.5: Prescales used for the trigger lines that select the normalisation channels for this analysis.

6.2.2 Stripping

The stripping line selection cuts are reported in Table 6.6. As it can be noticed, these cuts are very similar to the Hlt2 ones. Additional cuts on impact parameter and transverse momentum of the soft pion, on the D^0 candidate invariant mass and on the mass difference between the D^* and D^0 candidates are applied that allow the selection of the tagged sample.

6.2.3 Offline selection

The signal to background ratio of the stripped data samples $D^{*+} \rightarrow D^0(\rightarrow \mu^+ \mu^-) \pi^+$ can be further improved by applying additional cuts. As previously said, two main types of background were identified: the combinatorial one, due to two muons coming mainly from b decays, and the one coming from pions misidentified as muons in the $D^{*+} \rightarrow D^0(\rightarrow \pi^+ \pi^-) \pi^+$ decay. The former is mainly suppressed by applying additional geometrical cuts through a multivariate selection, using a Boosted Decision Tree, the latter by applying tight particle identification cuts. In the following, the choice of variables and of the optimal working point is described.

Variable	Cut value
kinematic cuts	
$\min(p_T(\mu))$	$> 750 \text{ MeV}/c$
$\max(p_T(\mu))$	$> 1100 \text{ MeV}/c$
$\min(p(\mu))$	$> 5000 \text{ MeV}/c$
$\min(\chi^2 IP(\mu))$ w.r.t. PV	> 3
$\max(\chi^2 IP(\mu))$ w.r.t. PV	> 8
χ_{FD}^2 of the D^0	> 20
$\cos(\text{Angle}(\vec{p}_{D^0}, \vec{r}_{PV} - \vec{r}_{DV}))$	> 0.9997
$p_T(D^0)$	$> 1800 \text{ MeV}/c$
D^0 Vertex fit χ^2	< 10
$\chi^2 IP(D^0)$ w.r.t. PV	< 15
additional cuts for the tagged selection	
$p_T(\pi)$	$> 110 \text{ MeV}/c$
$\chi^2 IP(\pi)$ w.r.t. PV	< 10
$D^{*\pm}$ Mass window	$\pm 110 \text{ MeV}/c^2$
invariant mass cuts	
D^0 Mass window	$\pm 70 \text{ MeV}/c^2$
Δm	$(145.421 \pm 10) \text{ MeV}/c^2$

Table 6.6: Summary of the selection cuts used in the stripping for the $D^{*+} \rightarrow D^0(\rightarrow \mu^+\mu^-)\pi^+$ selection. Cuts referred to muons are also applied to kaons and pions for the $D^{*+} \rightarrow D^0(\rightarrow \pi^+\pi^-)\pi^+$, $D^{*+} \rightarrow D^0(\rightarrow K^-\pi^+)\pi^+$ decays. The cuts which are labelled with π are referred to the *slow* pion coming from the D^* decay. The cuts selecting the D^* -tagged lines are in the second section of the table. All tracks are required to be reconstructed as *long*.

6.2.3.1 Decay Tree Fitter and mass range

The Decay Tree Fitter (DTF) procedure [49] reconstructs a complete decay chain involving multiple decay vertices. The method allows the simultaneous determination of decay time, position and momentum parameters together with their uncertainties and correlations for all the involved particles. In this context, the invariant mass difference $\Delta M = m_{\mu\mu\pi_s} - m_{\mu\mu}$ is used along with the mass of the $m_{\mu\mu}$ as a main discriminating variable. The resolution on ΔM is typically 0.5–0.6 MeV/c^2 but it reduces to half by performing a

Observable	Range (MeV/c ²)
m_{D^0}	1775-2100
Δm_{DTF}	139.6 - 151.6
m_{D^0} signal region	1840 - 1885
Δm_{DTF} signal region	144.9 - 146.1
m_{D^0} blind region	1834 - 1900

Table 6.7: Mass windows as imposed by the stripping selection. The signal region and the blind region are also reported.

kinematic fit using the Decay Tree Fitter implementation, and forcing the D^* to originate from the primary vertex. The new value obtained after the fit, hereafter referred to as ΔM_{DTF} , is used throughout the study. The mass ranges used for the analysis, together with the signal regions and the blind region, are imposed by the trigger and stripping selections and are reported in Table 6.7.

6.2.3.2 Preselection

Variable	Cut value
χ^2 fit DTF	< 100
PIDK μ^\pm	< 0
PIDK π^\pm	< 5

Table 6.8: Preselection cuts applied offline on candidates that passed the stripping selections.

Candidates passing the stripping cuts are required to satisfy loose requirements on the quality of the fit of the Decay Tree Fitter tool. In addition to this, the decay $D^0 \rightarrow K\pi$ misidentified as $D^0 \rightarrow \mu^+ \mu^-$ or as $D^0 \rightarrow \pi^+ \pi^-$ can be partially removed by applying a cut on the PIDK variable of the muons/pions. A summary of the preselection cuts is shown on Table 6.8.

6.2.3.3 Multivariate selection

A multivariate method (see Appendix A for its definition and a detailed description) is used for the final selection of signal candidates. The multivariate operator is revised with respect to the previous studies [17] both in the variables used and in the training method. In order to train the multivariate operator, a MC sample of $D^{*+} \rightarrow D^0(\rightarrow \mu^+\mu^-)\pi^+$ decays is used as signal. As background sample, the data events in the right sideband of the D^0 mass distribution are considered. In particular $m_{\mu\mu} - m_{D^0}^{\text{PDG}} > 30$ was required. In fact the right sideband is dominated by combinatorial background against which the MVA operator has to be trained; the left sideband instead would contain mostly partially reconstructed and misidentified backgrounds, which are treated separately in this study. The variables used are:

- $\mu \cos(\theta)$, the angle of the flight direction of the positive muon in the D^0 rest frame with respect to the D^0 momentum in the laboratory frame;
- $\cos(\gamma) = \hat{p}_{D^0} \cdot \hat{r}_{D^0}$, defined starting from the angle between the D^0 momentum and the line joining the PV and the particle decay vertex;
- D^0 $IP\chi^2$ with respect to the PV. IP stands for Impact Parameter (IP), that is the distance of closest approach between a reconstructed track and the primary vertex. $IP\chi^2$ is defined as the variation in the χ^2 per degree of freedom of the vertex fit done with and without the track associated to the considered particle. If the particle originates from the primary vertex the value of this variable is expected to be small, while it will be larger for particles produced in secondary vertices;
- D^0 distance of closest approach (DOCA) between the trajectories of the two muons. The DOCA for the tracks of two particles coming from a common vertex decay should be ideally zero;
- $\min(\mu IP\chi^2)$, the minimum impact parameter χ^2 of the two muons with respect to the PV;
- $\min(\mu p_T)$, minimum transverse momentum of the two muons;
- D^0 vertex χ^2 , the decay vertex of a particle is reconstructed starting from the decay particles tracks and a χ^2 of the fit is calculated;
- D^* DTF χ^2 , the χ^2 of the decay tree fit;

- $D^0 \cos(\theta)$, the angle of the D^0 in the D^* rest frame with respect to the D^* flight direction in the laboratory frame;
- D^0 FD χ^2 , flight distance χ^2 of the D^0 . the flight distance (here FD) is a measurement of the distance of the decay vertex from the primary vertex, thus being correlated to the mean life of the particle. This variable includes information on the errors on the determination of the two vertices position;
- $\min(\mu \text{ Iso})$, minimum isolation variable of the two muons. The isolation variable for a muon can be written as:

$$I_\mu = \frac{p_T(\mu)}{p_T(\mu) + \sum_i (p_T)_i}, \quad (6.4)$$

where i runs over the transverse momentum of all the charged particles inside a cone around the considered muon, whose momentum is excluded from the sum;

- π_s Iso, isolation variable of the slow pion;
- $\pi_s p_T$, transverse momentum of the slow pion;
- DTF $D^0 p_T$, as obtained after the decay tree fit.

Since the data sideband is used to train the BDT, in order to avoid biases the samples are split into nine sub-samples according to the event number (*i.e.* according to the module of the division by nine). The BDT is trained on the first four parts, tested on the second four and applied on data on the last part with cyclic permutations. In this way the applied BDT is always unbiased with respect to the event on which is computed. Figure 6.3 shows the comparison of the BDT ROC curves for different permutations. As expected, all the permutations have the same distribution. For a comparison with Ref. [17], the implemented BDT uses the same options and variables. Nevertheless, this BDT is not identical as the data and MC samples have different reconstruction, and because the training sample is larger than the one previously used. The BDT chosen for this study is compared with the old one in Fig. 6.4. The plot shows a significant performance gain mainly due to the exploitation of isolation variables. The final output of the BDT is distributed between -1 and +1. Its cumulative distribution function is used instead, which is distributed between 0 and 1. This function has the signal evenly distributed between 0 and 1 while the background shows a strong peak

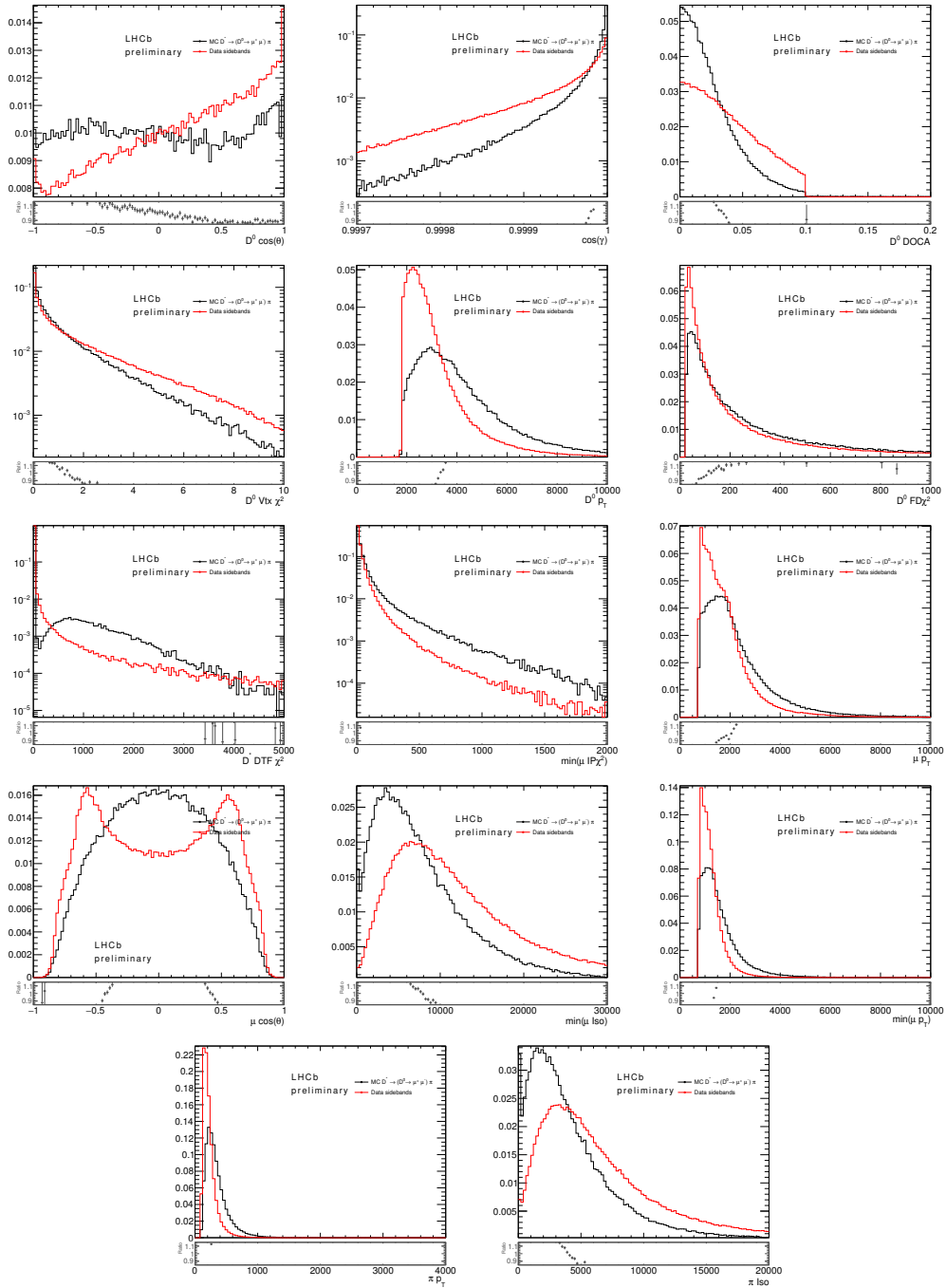


Figure 6.2: Normalised distributions of the variables used as input to the BDT for signal MC and data sidebands

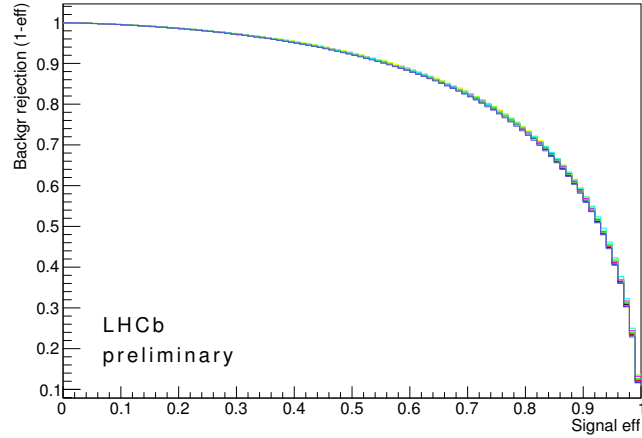


Figure 6.3: Comparison of the BDT ROC curves for the different permutations.

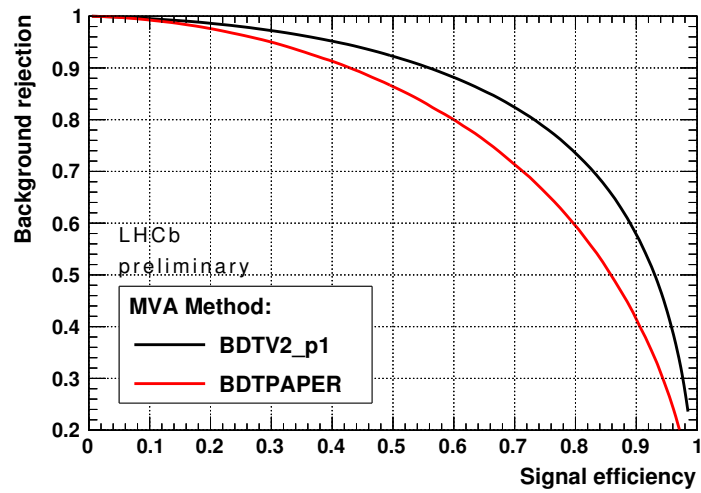


Figure 6.4: Comparison of the ROC curves, relative to the new training (black) and the one of the previous publication (red).

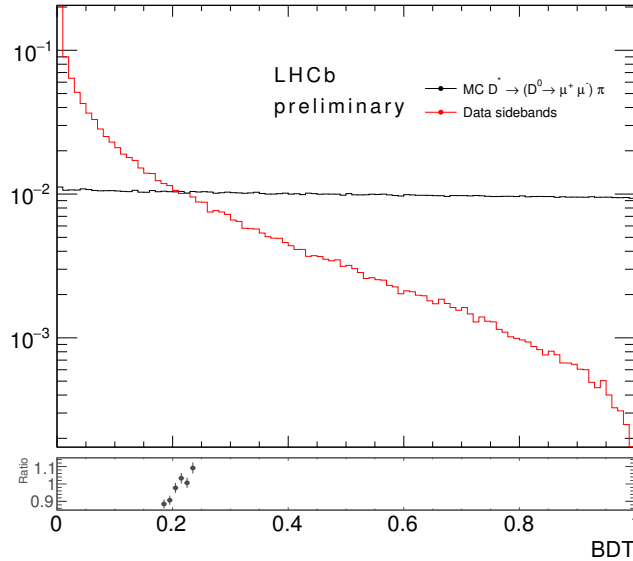


Figure 6.5: Distribution of the BDT variable for signal MC events and background events from the right sideband of the dimuon invariant mass.

at 0 with a fast decrease towards 1. This monotonous variable change does not modify the performances of the operator and allows a simpler calibration of the response in data. From here on the word “BDT” will represent this variable after the flattening operation. Possible biases in the combinatorial background invariant mass distribution were checked with an inclusive MC sample with three muons in the final state (developed for the $\tau \rightarrow \mu\mu\mu$ search). The profile distribution of the BDT as a function of the dimuon invariant mass for events passing the $D^{*+} \rightarrow D^0(\rightarrow \mu^+\mu^-)\pi^+$ selection in this sample is shown in Fig. 6.6. The plot shows that the distribution is consistent with the BDT being independent from the invariant mass, and in particular no bin with significantly higher value can be seen.

6.2.3.4 Offline muon identification cuts

Three main variables are used for muon identification in this study: IsMuon, NShared, requested to be 0, and MuIDPlus. The first two variables have been described in Ch. 4, while MuIDPlus is the new BDT classifier described in Ch. 5.

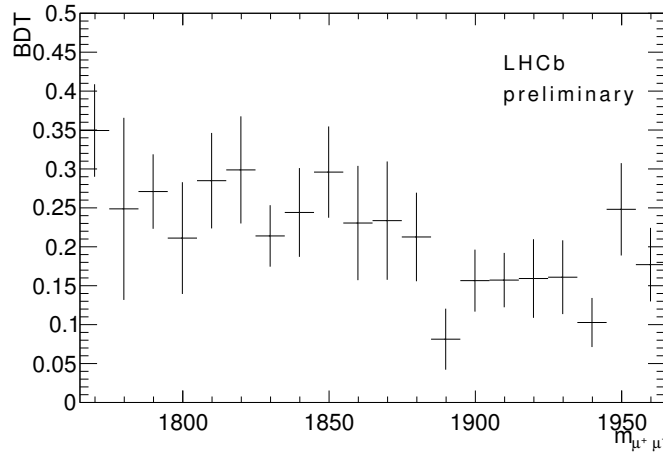


Figure 6.6: Profile histogram of the BDT variable as a function of the dimuon invariant mass for MC background events.

6.2.4 Optimisation

The choice of the best cuts to apply to a variable is usually done making use of an estimator, or Figure of Merit (FoM). For the study of rare decays the usual choice is to maximise the purity, in order to reduce the background as much as possible. Nevertheless, G. Punzi proved [50] that a better criterion is the choice of the selection that gives the best estimate for the cross section (or the best limit if the decay is not observed). In this study, the BDT output together with the cut on MuIDPlus have been optimised by maximising the Punzi FoM, which assume the following expression:

$$FoM = \frac{\varepsilon_{\mu\mu}^{\text{BDT+MuIDPlus}}}{\frac{a}{2} + \sqrt{N_{\text{bkg}}}}, \quad (6.5)$$

where:

- the parameter a is chosen to be equal to 3;
- $\varepsilon_{\mu\mu}$, the signal efficiency for a given BDT and MuIDPlus cut, is determined from MC;
- N_{bkg} , the number of background events, corresponds to the sum of two contributions:

$$N_{\text{bkg}} = N_{\text{comb}} + N_{\text{misID}}, \quad (6.6)$$

where

- N_{comb} is the number of combinatorial background events in the signal mass window. It is determined by extrapolating the fit results from the right-hand sideband to the blind region of the $m_{\mu\mu}$ distribution;
- N_{misID} represents the number of misidentified $D^0 \rightarrow \pi^+\pi^-$ events, as determined in Sec. 6.4. For bins with less than 10 events the error is determined as the biggest difference between the central value and the 68% poissonian CL. For bins with more than 10 events, the error is the square root of the yields.

The FoM as a function of the BDT and MuIDPlus cuts, for 2011 and 2012 data, is reported in Fig. 6.7. The optimal cut values are reported in Table 6.9, together with the signal efficiencies and the number of background events in the D^0 signal window.

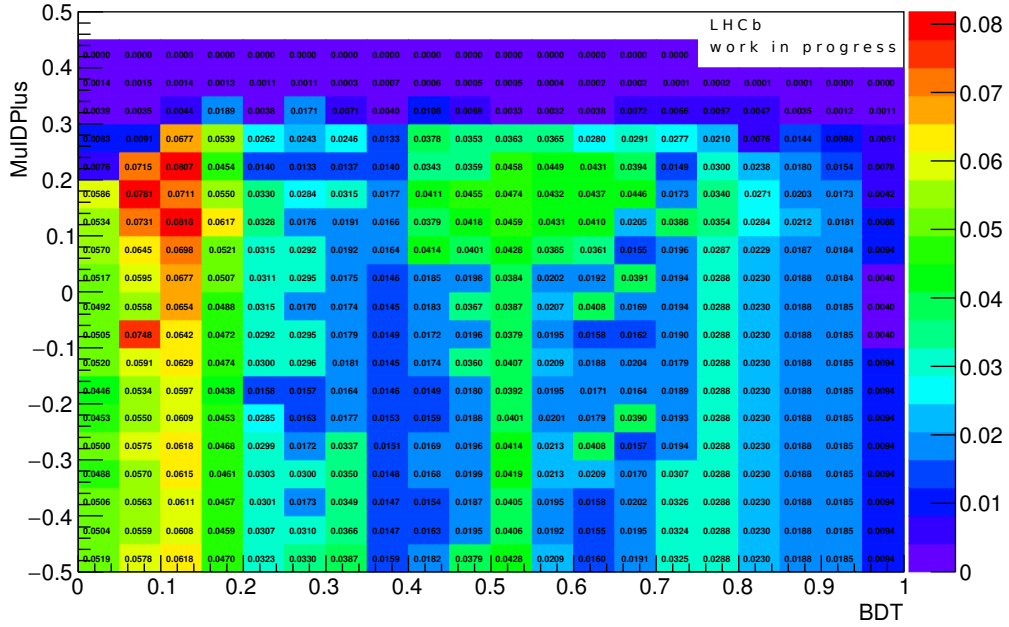
	2011	2012
BDT cut	> 0.1	> 0.5
muIDPlus cut	> 0.1	> 0.15
$\varepsilon_{\mu\mu}^{\text{BDT+MuIDPlus}}$	0.88	0.58
N_{comb}	167.9	79.9
N_{misID}	24.1	19.6

Table 6.9: Optimal BDT and MuIDPlus cut values, signal efficiency and number of background events in the D^0 signal window, for 2011 and 2012 data.

6.3 Normalisation

The determination of the efficiencies is mandatory to obtain the correct number signal events starting from the observed number of events. Moreover, the factorisation of the various contribution to the efficiency is useful to understand influence of the different systematic effects that can affect the measurement. In the expression for the branching ratio, different efficiencies

Punzi FOM - MuIDPlus vs BDT



Punzi FOM - MuIDPlus vs BDT

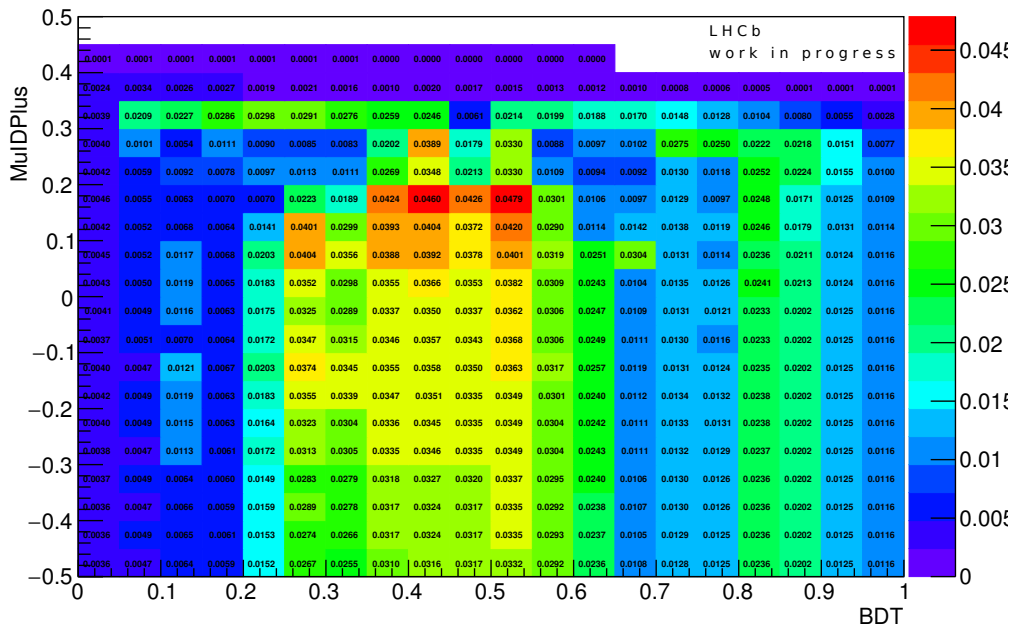


Figure 6.7: Figure of Merit for 2011 (top) and 2012 (bottom) data.

appear that will be described in the following: the acceptance efficiency ε_{acc} , the combined reconstruction, stripping and offline selection efficiencies $\varepsilon_{\text{rec/sel}}$ and the trigger efficiency $\varepsilon_{\text{trig}}$.

6.3.1 Detector acceptance

Decay mode	ε_{acc} 2011 (%)	ε_{acc} 2012 (%)
$D^{*+} \rightarrow D^0(\rightarrow \mu^+\mu^-)\pi^+$	20.07 ± 0.03	20.13 ± 0.03
$D^{*+} \rightarrow D^0(\rightarrow \pi^+\pi^-)\pi^+$	20.20 ± 0.03	20.27 ± 0.03

Table 6.10: Generator level efficiency averaged over magnet polarity for 2011 and 2012.

In order for a D^0 meson to be reconstructed it is necessary that the daughter tracks are within the LHCb acceptance, which corresponds to a polar angle between 10 and 400 mrad. To avoid the full simulation of all events, the acceptance cuts are applied already at the generator level. The efficiencies for these cuts are taken from the table of generator and simulation statistics provided to the collaboration. The values were obtained generating ten thousand signal decays for each mode and each of the magnet polarities. The efficiencies were then calculated from the number of passing and failing decays. The results for the MC signal and normalisations averaged over the magnet configurations are shown in Table 6.10.

6.3.2 Reconstruction, stripping and preselection efficiencies

The reconstruction, stripping and preselection efficiencies are determined from MC and are here combined for simplicity. The computed efficiency values, evaluated from simulated signal events that have already passed the acceptance requirements, are listed on Table 6.11.

6.3.3 Calibration of the trigger efficiencies

The trigger efficiencies for the $D^0 \rightarrow \mu^+\mu^-$ blind channel can be determined from MC samples. The final efficiency including the different trigger requests is reported in Table 6.12:

Decay mode	$\varepsilon_{\text{rec/sel}}$ 2011	$\varepsilon_{\text{rec/sel}}$ 2012
$D^{*+} \rightarrow D^0(\rightarrow \mu^+\mu^-)\pi^+$	0.0289 ± 0.0002	0.0277 ± 0.0001
$D^{*+} \rightarrow D^0(\rightarrow \pi^+\pi^-)\pi^+$	0.0366 ± 0.0002	0.0357 ± 0.0002

Table 6.11: Reconstruction, stripping and preselection efficiencies from MC samples. The errors reported in this table are only due to the statistical uncertainties of the MC samples.

Decay	L0+Hlt1+Hlt2/Selected
$D^{*+} \rightarrow D^0(\rightarrow \mu^+\mu^-)\pi^+$ (2011)	0.837 ± 0.003
$D^{*+} \rightarrow D^0(\rightarrow \mu^+\mu^-)\pi^+$ (2012)	0.719 ± 0.002

Table 6.12: Trigger efficiency for L0+Hlt1+Hlt2 from MC samples for $D^0 \rightarrow \mu^+\mu^-$ decay relative to the selection requirements. The errors collected in this table are only due to the statistical uncertainties of the MC samples.

The L0 trigger efficiencies for the $D^0 \rightarrow \pi^+\pi^-$ channel can instead be measured directly on data by exploiting the TISTOS method [51], as well as the TIS and TOS efficiencies, as:

$$\varepsilon_{\text{TIS}} = \frac{N_{\text{TISTOS}}}{N_{\text{TOS}}}, \quad (6.7)$$

$$\varepsilon_{\text{TOS}} = \frac{N_{\text{TISTOS}}}{N_{\text{TIS}}}, \quad (6.8)$$

$$\varepsilon_{\text{trig}} = \frac{N_{\text{trig}}}{N_{\text{TIS}}} \cdot \frac{N_{\text{TISTOS}}}{N_{\text{TOS}}}. \quad (6.9)$$

The number of TIS, TOS and triggered (trig) events was obtained directly with fits to the data samples. A fit to the ΔM was performed after a tight cut on the D^0 mass. Given the different trigger conditions of 2011 and 2012 data taking, the trigger efficiencies were measured separately for the two years.

The fits for the $D^0 \rightarrow \pi^+\pi^-$ are shown in Fig. 6.8 (2011) and in Fig. 6.9 (2012). The signal is described with a sum of a Crystal Ball shape with double tail and a simple gaussian. The background is described with `RoostD0Bg`. The signal shape parameters of the Crystal Ball are estimated on the MC sample and left free to float in a small range around the estimated values. The signal resolution and background parameters were left free to vary.

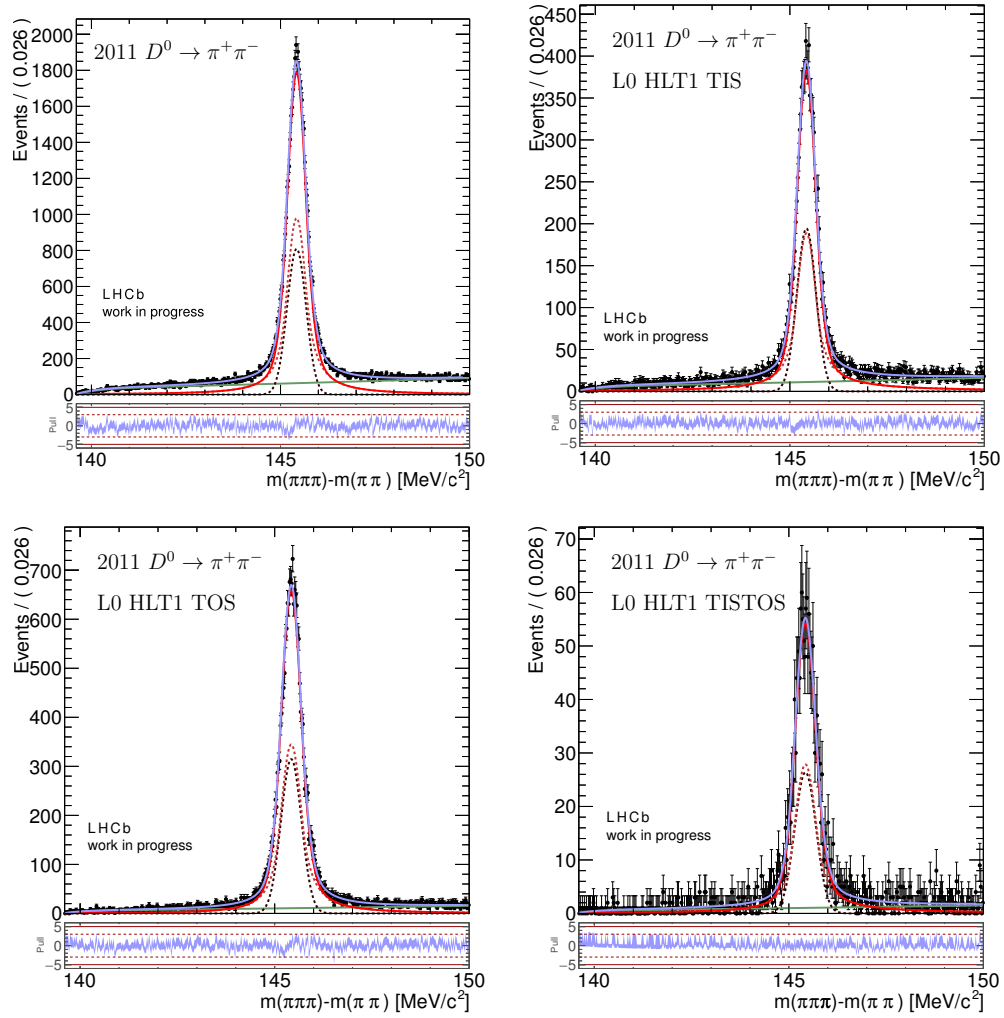


Figure 6.8: Fits of the $D^0 \rightarrow \pi^+\pi^-$ 2011 sample to extract the trigger efficiencies with the TISTOS method.

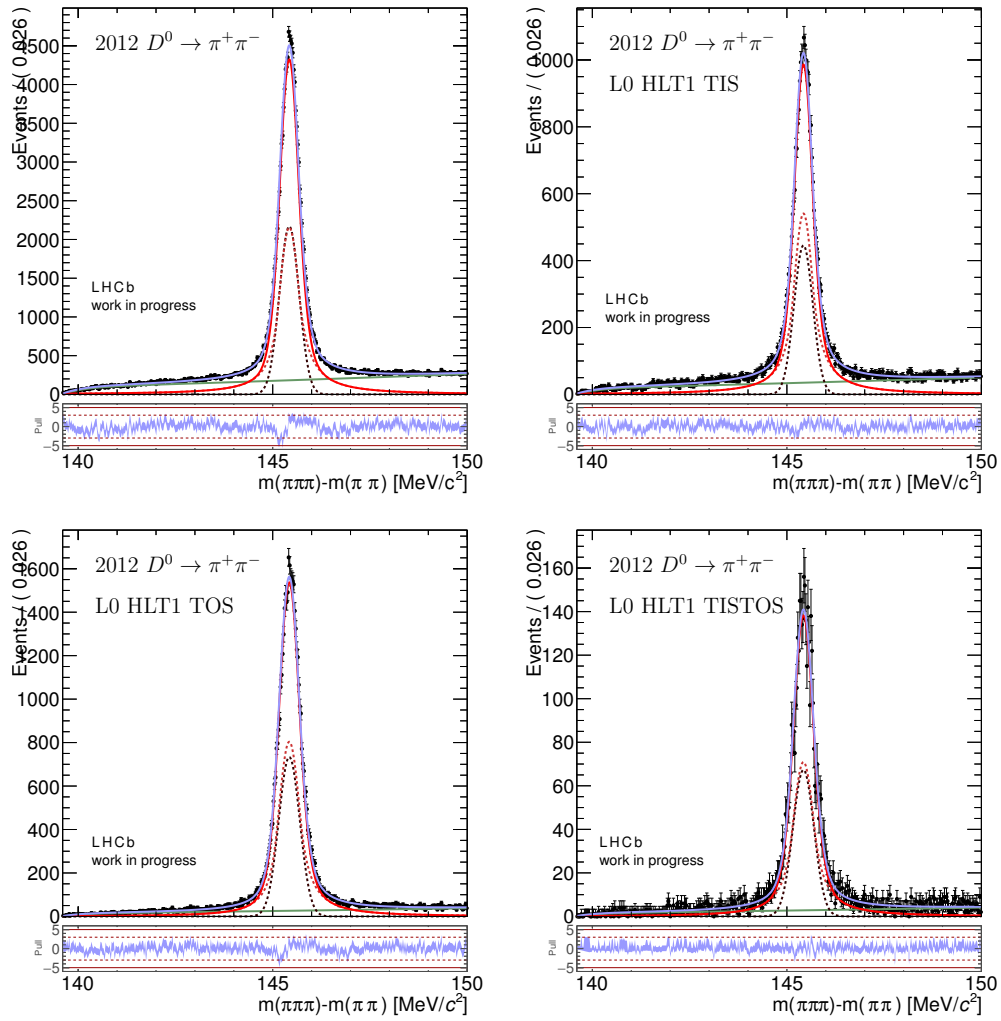


Figure 6.9: Fits of the $D^0 \rightarrow \pi^+\pi^-$ 2012 sample to extract the trigger efficiencies with the TISTOS method.

	$D^0 \rightarrow \pi^+\pi^-$	
	2011	2012
N_{trig}	$(5.30 \pm 0.08) \times 10^4$	$(1.318 \pm 0.005) \times 10^5$
N_{TIS}	$(1.15 \pm 0.03) \times 10^4$	$(4.77 \pm 0.04) \times 10^4$
N_{TOS}	$(1.99 \pm 0.03) \times 10^4$	$(2.96 \pm 0.03) \times 10^4$
N_{TISTOS}	$(1.74 \pm 0.04) \times 10^3$	$(4.37 \pm 0.08) \times 10^3$
$\varepsilon_{\text{trig}}$	0.40 ± 0.02	0.408 ± 0.009
ε_{TOS}	0.151 ± 0.005	0.148 ± 0.003
ε_{TIS}	0.087 ± 0.002	0.092 ± 0.002

Table 6.13: Trigger efficiencies as extracted with the TISTOS method in data.

$D^0 \rightarrow \pi^+\pi^-$			
2011		2012	
Hlt1/L0	Hlt2/Hlt1	Hlt1/L0	Hlt2/Hlt1
0.48 ± 0.02	0.920 ± 0.009	0.51 ± 0.01	0.931 ± 0.006

Table 6.14: Hlt1 and Hlt2 trigger efficiencies from MC samples for $D^0 \rightarrow \pi^+\pi^-$ decay. The errors collected in this table are only due to the statistical uncertainties of the MC samples.

The results of the fits are shown in Table 6.13 divided by year. The uncertainties are purely statistical and obtained from the fits. The efficiencies do not vary sensibly between 2011 and 2012.

The Hlt1 and Hlt2 efficiencies for the $D^0 \rightarrow \pi^+\pi^-$ channel are determined from simulation. It is worth noting that for 2012 MC samples, leaving the Hlt2 requirement indirectly requires LOGlobal despite no specific requirements are made on this. For this reason the Hlt2 requirement is removed from stripping and its efficiency determined with respect to physics TIS triggers (*e.g.* Hadron, Muon, Photon, etc.). The values of the efficiencies are shown in Table 6.14.

6.4 Fit model

Since the signal region is blind, this section only presents the studies relating to the modelisation of the background.

6.4.1 Combinatorial background

The combinatorial background is studied directly on data. The PDF for the m_{D^0} distribution is determined using the right-hand sideband events, which are not polluted by other backgrounds and is parametrised with a linear function $\mathcal{P}ol(\lambda)$, where the λ parameter, represents the slope. For the Δm observable a dedicated threshold function is used, the `RootStdDBG`:

$$f_{\Delta m}(a, b, c) = (1 - e^{-(\Delta m - \Delta m_0)/c}) \cdot \left(\frac{\Delta m}{\Delta m_0} \right)^a + b \left(\frac{\Delta m}{\Delta m_0} - 1 \right). \quad (6.10)$$

which depends on three parameters a , c , determining how fast the function saturates, and b , a linear term in the Δm distribution.

6.4.2 Misidentified $K\pi$ background

This type of backgrounds is determined on data, following the studies done in Ref. [52]. A single exponential $\mathcal{E}xp(\alpha)$ with a negative slope α is used for the m_{D^0} distribution of the sum of the two components, while a gaussian $\mathcal{G}auss(\mu, \sigma)$ is used for Δm . The gaussian width is constrained to the values in Ref. [17] while the slope of the exponential is left free to vary in the fit.

6.4.3 Misidentified $\pi\pi$ background

The most important peaking background is due to $D^{*+} \rightarrow D^0(\rightarrow \pi^+\pi^-)\pi^+$ decays, where two pions are misidentified as muons. Strong particle ID cuts are applied to both muon tracks, however, given the high branching fraction for this decay channel, a significant fraction of them is misidentified. In order to determine their contribution, a high statistics sample of simulated $D^{*+} \rightarrow D^0(\rightarrow \pi^+\pi^-)\pi^+$ has been produced and then filtered with the same offline selection applied to data and reconstructed as $D^{*+} \rightarrow D^0(\rightarrow \mu^+\mu^-)\pi^+$. This approach has the double advantage of giving information not only on the rate but also on the shape of the background. In addition, the misidentification correlation between the two pion tracks is naturally taken into account. The

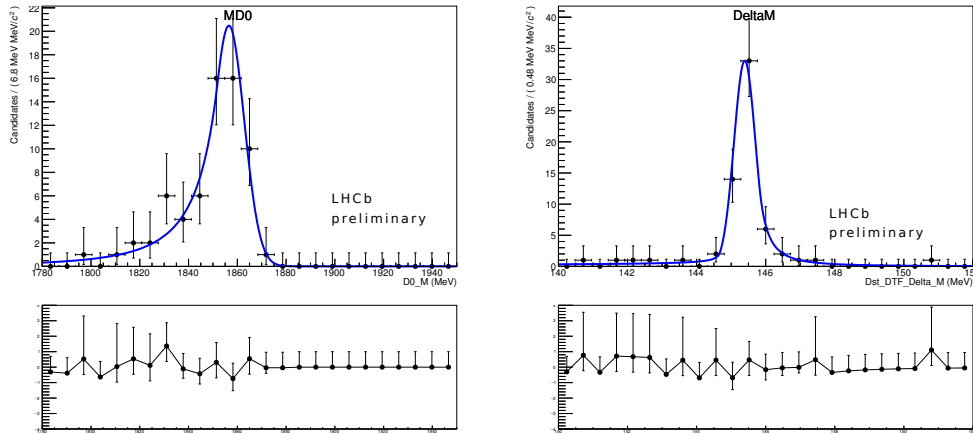


Figure 6.10: Shapes for $D^{*+} \rightarrow D^0(\rightarrow \pi^+\pi^-)\pi^+$ misidentified as $D^{*+} \rightarrow D^0(\rightarrow \mu^+\mu^-)\pi^+$ in 2011 simulation.

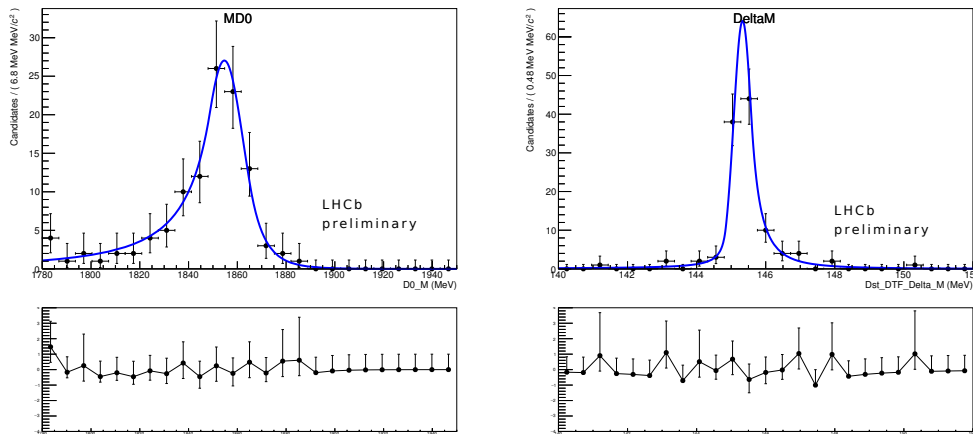


Figure 6.11: Shapes for $D^{*+} \rightarrow D^0(\rightarrow \pi^+\pi^-)\pi^+$ misidentified as $D^{*+} \rightarrow D^0(\rightarrow \mu^+\mu^-)\pi^+$ in 2012 simulation.

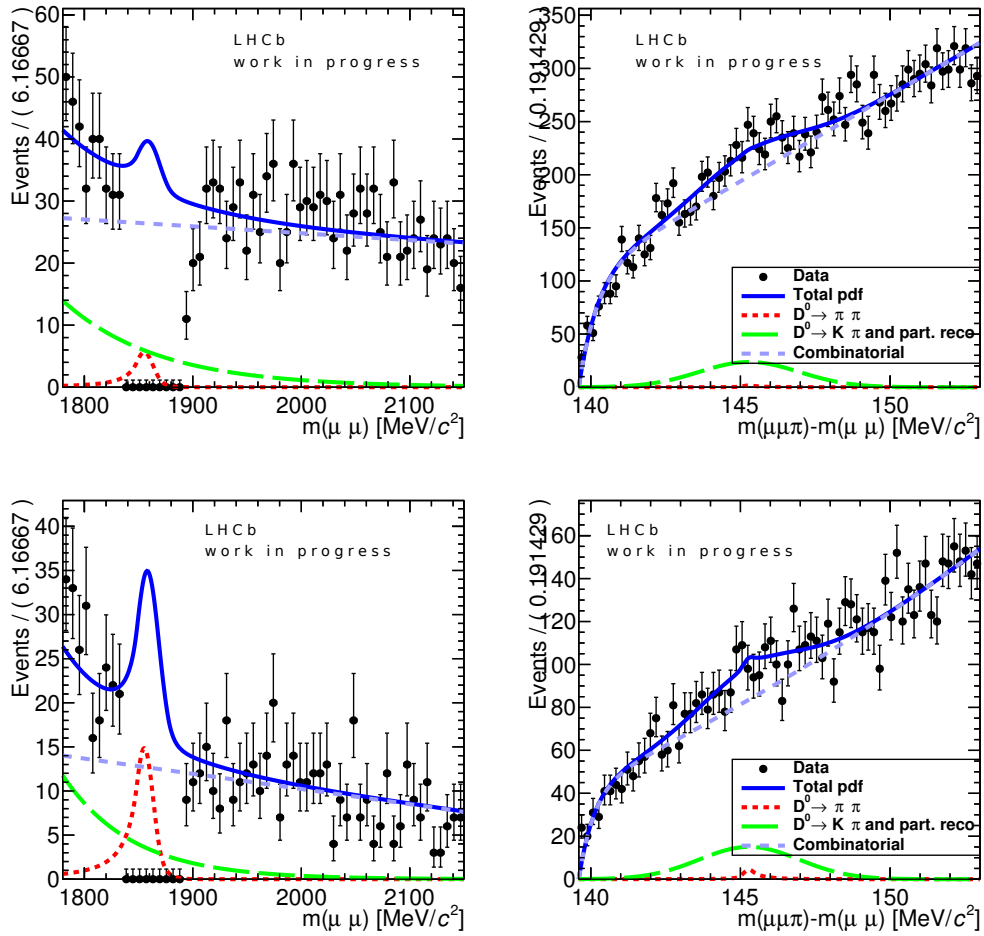


Figure 6.12: Blinded mass fit to selected $D^{*+} \rightarrow D^0(\rightarrow \mu^+ \mu^-) \pi^+$ events. Data from 2011 is on the top, 2012 on the bottom.

final shapes obtained for 2011 and 2012 are shown in Fig. 6.10 and Fig. 6.11, respectively.

The shapes are fitted with a double Crystal Ball shape both in D^0 mass and ΔM_{DTF} .

6.4.4 Blind fit

The fit results after the entire selection chain are shown in Fig. 6.12, where all the components are shown except for the signal one.

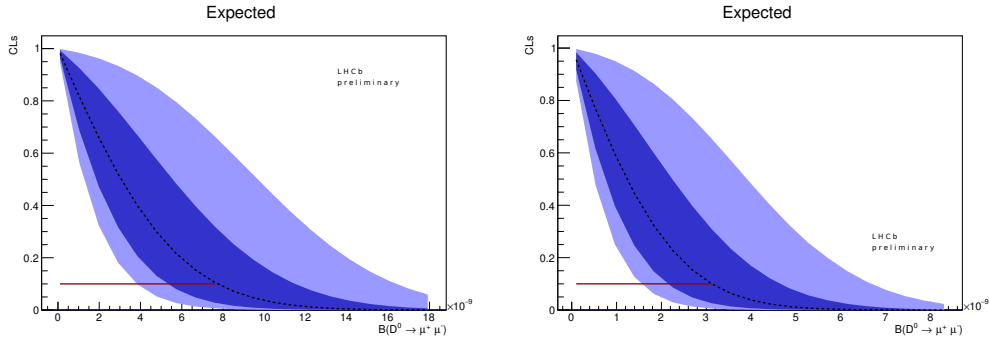


Figure 6.13: Expected CLs as a function of the $D^0 \rightarrow \mu^+\mu^-$ branching fraction as obtained using (a) 2011 data and (b) 2012 data.

6.5 Results

The limit on the $D^0 \rightarrow \mu^+\mu^-$ branching fraction is computed using the CLs [53] method as implemented in ROOSTATS [54]. For this thesis the asymptotic approximation is used, which reproduces very well the frequentist one. The expected background components are estimated as described in Sec. 6.4. The combinatorial background is extracted from the fit to the blind data. The misidentified component is evaluated from estimates of the misID in data.

The expected CLs using the asymptotic method are shown in 6.13 and the computed limits at 90% CL are reported in Table 6.15.

Computed upper limit at 90% CL for $D^0 \rightarrow \mu^+\mu^-$	
2011	$5.7 \cdot 10^{-09}$
2012	$3.1 \cdot 10^{-09}$

Table 6.15: Computed upper limits as obtained for the single year datasets separated.

Comparing these results with the current upper limit for the $D^0 \rightarrow \mu^+\mu^-$ branching fraction [17] $\mathcal{B}(D^0 \rightarrow \mu^+\mu^-) < 6.2(7.6) \cdot 10^{-9}$ at 90% CL (95% CL), obtained with data collected in 2011, an improvement can be noticed that can be credited to an enhancement in the background rejection. These

results are very preliminary since the correct approach would have required to have a specific tuning of the BDT on the studied decay channel.

Conclusions

This thesis was devoted to the development of a novel algorithm for the muon identification in the LHCb experiment and its application.

The newly developed discriminating variable has been tested on a Monte Carlo sample specifically tuned to reproduce the particle fluxes expected after the upgrade; the new information included in the algorithm has shown to drastically improve the performance of background rejection as the muon identification efficiency threshold varies.

The variable has thus been included in a Boosted Decision Tree classifier in order to be tested in the context of the ongoing $K_S^0 \rightarrow \mu^+ \mu^-$ analysis [47], where it proved to have comparable or even better performances with respect to the muon identification algorithms which are currently used.

Thanks to the encouraging results, the algorithm has been included as *additional information* in the Run 2 stripping data and is currently available to all the LHCb community, although it is optimised for the $K_S^0 \rightarrow \mu^+ \mu^-$ decay. It has thus been tested on calibration samples of $J/\psi \rightarrow \mu^+ \mu^-$ (for the signal) and $D^{*+} \rightarrow D^0(\rightarrow K^- \pi^+) \pi^+$ (for the pion background), whose muon momentum distributions are different from those of the $K_S^0 \rightarrow \mu^+ \mu^-$. Nevertheless, the algorithm allowed a better background rejection as a function of the muon identification efficiency when compared to the ProbNN method. It has to be noticed that the new algorithm does not reproduce in this case the performance improvement shown in the $K_S^0 \rightarrow \mu^+ \mu^-$ analysis when it is compared to the CombDLL classifier. This feature will be further investigated, although some losses in performances are expected here because this sample is quite different from the one used for the BDT tuning.

The algorithm has been finally tested on the study of the $D^0 \rightarrow \mu^+\mu^-$ decay, which represents a benchmark channel for the search of New Physics. This preliminary study allowed to set an expected limit for the branching fraction of the $D^0 \rightarrow \mu^+\mu^-$ decay that shows an improvement with respect to the previous limit. Encouraged by this very promising result, the possibility of including the new MuIDPlus algorithm in the 2017 trigger will be evaluated in the next months.

Multivariate selection

Several variables used in candidate selection, show a correlation that can be very strong. Abandonment of simple rectangular cuts, chosen independently for each variable, in favour of the simultaneous observation and analysis of more than one variable allows to take into account the possible correlations between them thus permitting the optimal separation of the signal events from the background.

A.1 Boosted Decision Tree

A decision tree [55] is a tree-structured classifier that acts on single events through repeated left/right (yes/no) decisions on single variables, until they are categorised as signal or background. As shown in Fig. A.1, starting from the root node, a sequence of binary splits using cuts (c_1, c_2, \dots) on the discriminating variables (x_i, x_j, \dots) is applied to the data. In each split the variable (and the corresponding cut) is chosen that gives the best separation between signal and background in that particular node. For this reason the same variable may be used at several nodes and others might not be used at all. The leaf nodes at the end of the tree are labeled as signal, S , and background, B , depending on the majority of events that end up in the considered node.

Defining the purity p as $p = S/(S + B)$, the separation criterion for node splitting is called *Gini Index* and is defined as $I_{\text{Gini}} = p(1 - p)$. The criterion is symmetric with respect to the event classes: it has a maximum

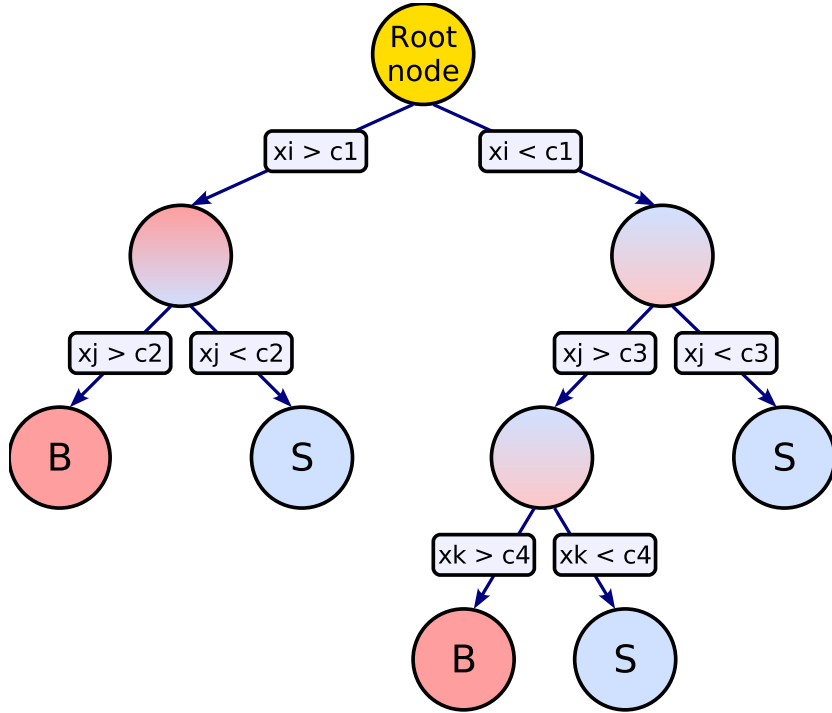


Figure A.1: Schematic view of a decision tree.

where the samples are fully mixed, *i.e.* at $p = 0.5$, and is zero if the sample consists of one event class only (both signal and background). From these definitions follows that the choice of the variable and its cut is based on the maximisation of the difference of I_{Gini} between the parent sample and the two daughter samples, that is

$$I_{\text{Gini}}^{\text{parent}} - \left(I_{\text{Gini}}^{\text{daughter 1}} + I_{\text{Gini}}^{\text{daughter 2}} \right). \quad (\text{A.1})$$

The classifier response is reproducible applying the same tree growing algorithm to the same data sample. Rather, its instability resides in the behaviour shown when two input variables exhibit similar separation power: in this case, a fluctuation in the sample may cause the algorithm to decide to split on one variable neglecting the other, altering the whole tree structure starting from this node, possibly causing a completely different classifier response. The *boosting* procedure allows to overcome this problem by constructing a forest of decision trees starting from the same training sample but assigning different weights to the events. The Boosted Decision Tree (BDT)

classifier is more statistically stable and has better separation performances compared to a single decision tree.

A.2 Training, test and application

The multivariate analysis consists of three steps:

- the training or growing of the decision tree is the process that defines the splitting variables and their cuts for each node. The node splitting stops once it has reached the minimum number of events specified in the decision tree configuration. The leaf nodes are labelled as signal or background on according to the class the majority of events belongs to. This procedure needs a prior knowledge of the two categories and of the variable distributions;
- the test phase consists in the application of the grown decision tree to a sample that is independent still analogous to the one used for the training, in order to make sure of the proper working of the classification procedure;
- the application of the method on the sample.

The test phase requires particular care not to meet with the problem of overtraining, which occurs when a problem has too few degrees of freedom because too many parameters of the algorithm were adjusted to too few data points. A solution to counteract overtraining consists in the use of three statistically independent data sets: one to do the training, one to identify when the training has to be suspended (and for the pruning of insignificant nodes), and the last one for the performance validation.

A.3 Likelihood

Peaking contributions in the signal region of the invariant mass are typical of misidentified background, and they cannot be removed with a simple sideband subtraction. To get rid of these events it is mandatory to cut on identification variables.

For an event with n variables x_i , the likelihood defines the probability for an event to belong to the category k as

$$\mathcal{L}^k = \prod_i^n p_i^k(x_i), \quad (\text{A.2})$$

that is the product of the probability for each variable to belong to an event of the category k . The single probabilities are calculated with probability distribution functions normalised to 1 $\forall k, i$, and are the result of a fit to an histogram in the experimental case. The logarithm of the likelihood (log-likelihood) is usually preferred, for it allows to deal with sums instead of products:

$$\ln \mathcal{L}^k = \sum_i^n \ln p_i^k(x_i). \quad (\text{A.3})$$

The likelihood indicates how well a given hypothesis is supported by a given observation but the likelihood alone is not sufficient for a decision in favour of one or the other hypothesis. As a discriminating variable, the difference between the log-likelihoods for two given hypotheses (h_1, h_2) is often used (delta-log-likelihoods), which has the form

$$\Delta LL_{h_1/h_2} = \ln \mathcal{L}(h_1) - \ln \mathcal{L}(h_2) = \ln \left(\frac{\mathcal{L}(h_1)}{\mathcal{L}(h_2)} \right). \quad (\text{A.4})$$

A.4 Neural Networks

The expression (Artificial) Neural Networks (NN) indicates the simulation of artificial neurons connected one with each other, each neuron being able to give a particular output to a given input. The power of Neural Networks is in the opportunity of requiring a non-linear response from a neuron and hence from the entire network, that becomes able to solve complex problems.

A weight w is associated to the connection of each neuron to others; each neuron gives a single output for each input applying a response function $\phi(x)$, which is usually a sigmoid function, defined by the formula $\frac{1}{1+e^{-x}}$, or a $\tanh(x)$.

In multilayer NN, neurons are divided into layers and the connections are only allowed between different layers. In this case the output of the whole network will be:

$$y_{\text{out}} = \sum_{j=1}^{n_h} y_j^{(2)} w_{j1}^{(2)} = \sum_{j=1}^{n_h} \phi \left(\sum_{i=1}^{n_{\text{in}}} x_i w_{ij}^{(1)} \right) w_{j1}^{(2)} \quad (\text{A.5})$$

where n_{in} and n_h are the number of input and middle neurons, and w_{ij} is the weight applied between the i^{th} and the j^{th} neurons of two layers. ProbNN is an example of algorithm based on Neural Networks.

Bibliography

- [1] D. J. Griffiths, *Introduction to elementary particles; 2nd rev. version.* Physics textbook, New York, NY: Wiley, 2008.
- [2] Fayyazuddin and Riazuddin, *A Modern Introduction to Particle Physics; 2nd ed.* World Scientific Publishing, 2000.
- [3] K. A. Olive *et al.*, “Review of Particle Physics,” *Chin. Phys.*, vol. C38, p. 090001, 2014.
- [4] Y. Ashie *et al.*, “Evidence for an oscillatory signature in atmospheric neutrino oscillations,” *Phys. Rev. Lett.*, vol. 93, p. 101801, Sep 2004.
- [5] M. G. Aartsen *et al.*, “Measurement of atmospheric neutrino oscillations with icecube,” *Phys. Rev. Lett.*, vol. 111, p. 081801, Aug 2013.
- [6] M. Kobayashi and T. Maskawa, “CP-Violation in the Renormalizable Theory of Weak Interaction,” *Prog. Theor. Phys.*, vol. 49, pp. 652–657, 1973.
- [7] G. Aad *et al.*, “Observation of a new particle in the search for the Standard Model Higgs boson with the ATLAS detector at the LHC,” *Physics Letters B*, vol. 716, no. 1, pp. 1 – 29, 2012.
- [8] S. Chatrchyan *et al.*, “Observation of a new boson at a mass of 125 GeV with the CMS experiment at the LHC,” *Physics Letters B*, vol. 716, no. 1, pp. 30 – 61, 2012.
- [9] G. Aad *et al.*, “Combined Measurement of the Higgs Boson Mass in pp Collisions at $\sqrt{s} = 7$ and 8 TeV with the ATLAS and CMS Experiments,” *Phys. Rev. Lett.*, vol. 114, p. 191803, 2015.

- [10] T. Teubner, “The Standard Model,” School for Experimental High Energy Physics Students, (Oxford: STFC), pp. 112 – 206, W.J.Murray, & M.E.Evans (Eds.), 2009.
- [11] L. Maiani, “The GIM Mechanism: origin, predictions and recent uses,” Mar 2013. Comments: Opening Talk, Rencontres de Moriond, EW Interactions and Unified Theories, La Thuile, Valle d’Aosta, Italia, 2-9 March, 2013.
- [12] L. Wolfenstein, “Parametrization of the Kobayashi-Maskawa Matrix,” *Phys. Rev. Lett.*, vol. 51, pp. 1945–1947, Nov 1983.
- [13] C. S. Wu, E. Ambler, R. W. Hayward, D. D. Hoppes, and R. P. Hudson, “Experimental test of parity conservation in beta decay,” *Phys. Rev.*, vol. 105, pp. 1413–1415, Feb 1957.
- [14] J. H. Christenson, J. W. Cronin, V. L. Fitch, and R. Turlay, “Evidence for the 2π Decay of the K_2^0 Meson,” *Phys. Rev. Lett.*, vol. 13, pp. 138–140, Jul 1964.
- [15] G. Burdman, E. Golowich, J. L. Hewett, and S. Pakvasa, “Rare charm decays in the standard model and beyond,” *Phys. Rev.*, vol. D66, p. 014009, 2002.
- [16] N. K. Nisar *et al.*, “Search for the rare decay $D^0 \rightarrow \gamma\gamma$ at Belle,” *Phys. Rev.*, vol. D93, no. 5, p. 051102, 2016.
- [17] R. Aaij *et al.*, “Search for the rare decay $D^0 \rightarrow \mu^+\mu^-$,” *Phys. Lett.*, vol. B725, pp. 15–24, 2013.
- [18] G. Burdman and I. Shipsey, “ $D^0 - \bar{D}^0$ mixing and rare charm decays,” *Ann. Rev. Nucl. Part. Sci.*, vol. 53, pp. 431–499, 2003.
- [19] A. Paul, A. De La Puente, and I. I. Bigi, “Manifestations of warped extra dimension in rare charm decays and asymmetries,” *Phys. Rev.*, vol. D90, no. 1, p. 014035, 2014.
- [20] A. Breskin and R. Voss, *The CERN Large Hadron Collider: Accelerator and Experiments*. Geneva: CERN, 2009.
- [21] C. Lefèvre, “The CERN accelerator complex. Complexe des accélérateurs du CERN.” Dec 2008.

- [22] The LHCb Collaboration, “The LHCb Detector at the LHC,” *Journal of Instrumentation*, vol. 3, no. 08, p. S08005, 2008.
- [23] P. R. Barbosa-Marinho *et al.*, *LHCb VELO (VERtex LOCator): Technical Design Report*. Technical Design Report LHCb, Geneva: CERN, 2001.
- [24] Aaij, R. and others, “Performance of the LHCb Vertex Locator,” *JINST*, vol. 9, p. 09007, 2014.
- [25] R. Antunes-Nobrega *et al.*, *LHCb reoptimized detector design and performance: Technical Design Report*. Technical Design Report LHCb, Geneva: CERN, 2003.
- [26] E. Bos *et al.*, “The Trajectory Model for Track Fitting and Alignment,” Tech. Rep. LHCb-2007-008. CERN-LHCb-2007-008, CERN, Geneva, Mar 2007.
- [27] B. De Paula, F. Marinho, and S. Amato, “Analysis of the $B_s \rightarrow \mu^+ \mu^-$ Decay with the Reoptimized LHCb Detector,” Tech. Rep. LHCb-2003-165, CERN, Geneva, Mar 2004.
- [28] P. R. Barbosa-Marinho *et al.*, *LHCb muon system: Technical Design Report*. Technical Design Report LHCb, Geneva: CERN, 2001.
- [29] *LHCb muon system: addendum to the Technical Design Report*. Technical Design Report LHCb, Geneva: CERN, 2003.
- [30] *LHCb muon system: second addendum to the Technical Design Report*. Technical Design Report LHCb, Geneva: CERN, 2005. Submitted on 9 Apr 2005.
- [31] “Handling of the generation of primary events in gauss, the lhcb simulation framework,” *Journal of Physics: Conference Series*, vol. 331, no. 3, p. 032047, 2011.
- [32] T. Sjöstrand, S. Mrenna, and P. Skands, “A brief introduction to PYTHIA 8.1,” *Computer Physics Communications*, vol. 178, no. 11, pp. 852 – 867, 2008.
- [33] D. J. Lange, “The evtgen particle decay simulation package,” *Nuclear Instruments and Methods in Physics Research Section A: Accelerators, Spectrometers, Detectors and Associated Equipment*, vol. 462, no. 1-2,

- pp. 152 – 155, 2001. BEAUTY2000, Proceedings of the 7th Int. Conf. on B-Physics at Hadron Machines.
- [34] S. Agostinelli *et al.*, “Geant4-a simulation toolkit,” *Nuclear Instruments and Methods in Physics Research Section A: Accelerators, Spectrometers, Detectors and Associated Equipment*, vol. 506, no. 3, pp. 250 – 303, 2003.
- [35] “The LHCb digitization program.”
- [36] “The LHCb High Level Trigger program.”
- [37] “World wide LHC computing grid.”
- [38] “Letter of Intent for the LHCb Upgrade,” Tech. Rep. CERN-LHCC-2011-001. LHCC-I-018, CERN, Geneva, Mar 2011.
- [39] I. Bediaga *et al.*, “Framework TDR for the LHCb Upgrade: Technical Design Report,” Tech. Rep. CERN-LHCC-2012-007. LHCb-TDR-12, Apr 2012.
- [40] A. Bharucha *et al.*, “Implications of LHCb measurements and future prospects,” *The European Physical Journal C*, vol. 73, no. 4, pp. 1–92, 2013.
- [41] R. Aaij *et al.*, “First Measurement of the CP -Violating Phase in $B_s^0 \rightarrow \phi\phi$ Decays,” *Phys. Rev. Lett.*, vol. 110, p. 241802, Jun 2013.
- [42] R. Aaij *et al.*, “First Evidence for the Decay $B_s^0 \rightarrow \mu^+\mu^-$,” *Phys. Rev. Lett.*, vol. 110, p. 021801, Jan 2013.
- [43] “Observation of the rare $B_s^0 \rightarrow \mu^+\mu^-$ decay from the combined analysis of CMS and LHCb data,” *Nature*, vol. 522, 2015.
- [44] LHCb Collaboration, “LHCb PID Upgrade Technical Design Report,” Tech. Rep. CERN-LHCC-2013-022. LHCb-TDR-014, Nov 2013.
- [45] M. Anelli *et al.*, “Performance of the LHCb muon system with cosmic rays,” *JINST*, vol. 5, p. P10003, 2010.
- [46] F. Archilli *et al.*, “Performance of the Muon Identification at LHCb,” *J. Instrum.*, vol. 8, p. P10020. 17 p, Jun 2013.

- [47] “Updated limit for the decay $K_S^0 \rightarrow \mu^+\mu^-$,” Tech. Rep. LHCb-CONF-2016-012. CERN-LHCb-CONF-2016-012, CERN, Geneva, Oct 2016.
- [48] C. Patrignani *et al.*, “Review of Particle Physics,” *Chin. Phys.*, vol. C40, no. 10, p. 100001, 2016.
- [49] W. D. Hulsbergen, “Decay chain fitting with a Kalman filter,” *Nuclear Instruments and Methods in Physics Research A*, vol. 552, pp. 566–575, Nov. 2005.
- [50] G. Punzi, “Sensitivity of searches for new signals and its optimization,” *eConf*, vol. C030908, p. MODT002, 2003.
- [51] Tolk, S. and Albrecht, J. and Dettori, F. and Pellegrino, A., “Data driven trigger efficiency determination at LHCb,” Tech. Rep. LHCb-PUB-2014-039. CERN-LHCb-PUB-2014-039, CERN, Geneva, May 2014.
- [52] Bonivento, Walter and Dettori, Francesco, “Search for the $D^0 \rightarrow \mu^+\mu^-$ decay with 922 pb^{-1} at LHCb,” Feb 2011. Linked to LHCb-CONF-2012-005.
- [53] J. Neyman, “Outline of a theory of statistical estimation based on the classical theory of probability,” *Philosophical Transactions of the Royal Society of London A: Mathematical, Physical and Engineering Sciences*, vol. 236, no. 767, pp. 333–380, 1937.
- [54] L. Moneta, K. Cranmer, G. Schott, and W. Verkerke, “The RooStats project,” in *Proceedings of the 13th International Workshop on Advanced Computing and Analysis Techniques in Physics Research. February 22-27, 2010, Jaipur, India.*, p. 57, 2010.
- [55] A. Hoecker *et al.*, “TMVA - Toolkit for Multivariate Data Analysis,” *ArXiv Physics e-prints*, Mar. 2007.